Surface Precipitation in Gold and Tungsten Containing Iron-based Alloys and Steels

MSc Thesis

P. Martin Rojo

Draft January 2020

MSc Aerospace Engineering
Technical University of Delft

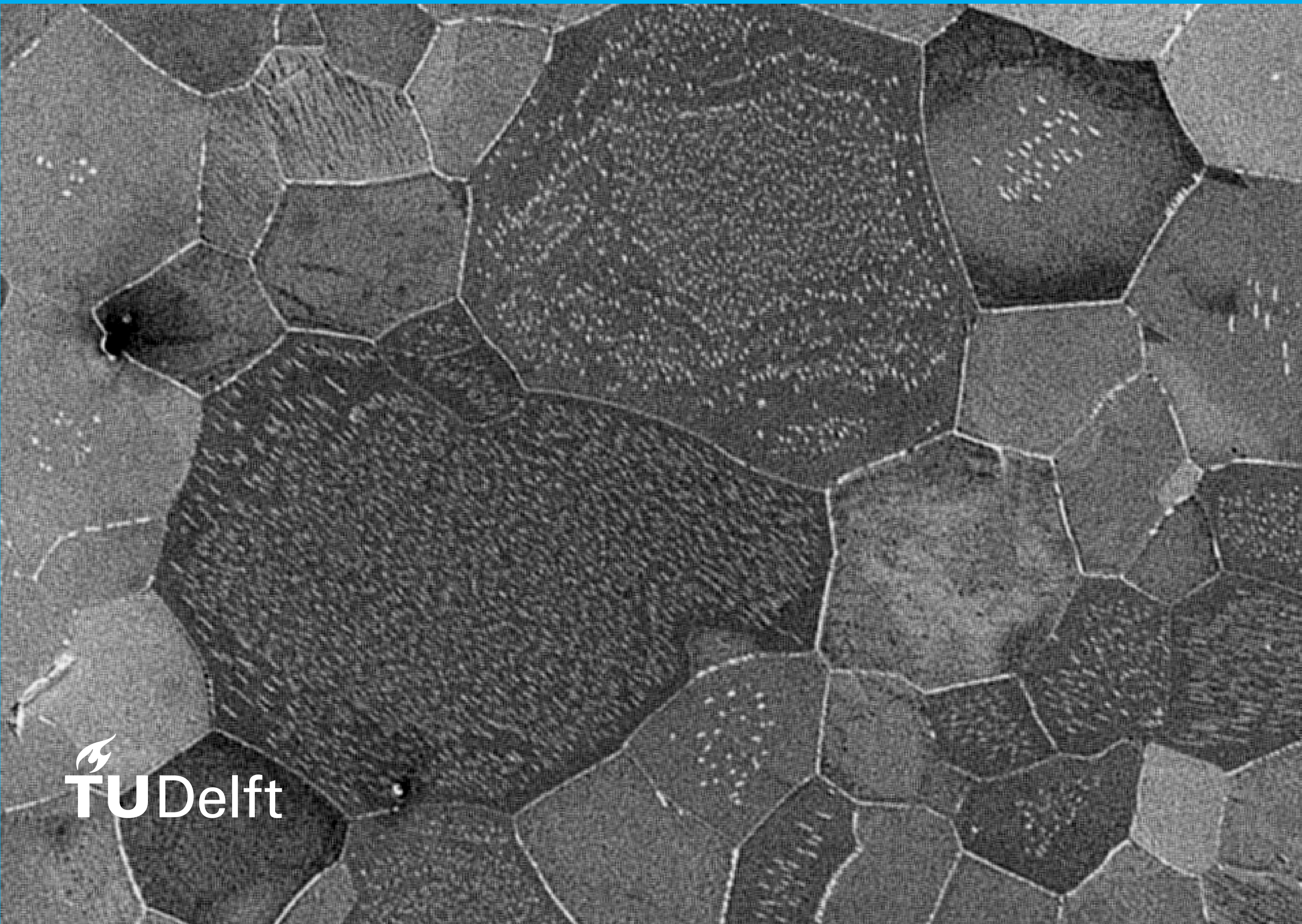

Surface Precipitation in Gold and Tungsten Containing Iron-based Alloys and Steels

MSc Thesis

by

P. Martin Rojo

to obtain the degree of Master of Science
at the Delft University of Technology,
to be defended publicly on Monday January 20, 2020 at 09:00 AM.

Student number:	4734084	
Project duration:	March 1, 2019 – January 20, 2020	
Thesis committee:	Prof. dr. ir. S. v.d. Zwaag,	TU Delft, supervisor
	Dr. N.H. v. Dijk ,	TU Delft
	MSc. J. Sinke,	TU Delft

Preface

This Thesis report is the result of my the Master's Thesis research at the group of Novel Aerospace Materials in the Delft University of Technology. The aim of the report is to study the new phenomenon of surface precipitation on Fe-Au and Fe-Au-W alloys, and an experimental creep designed steel with a composition close to commercial creep steels. Surface precipitation has been observed as an easier alternative to understand creep-cavity precipitation, which is fundamental to develop the theory of self healing metals.

The insights of this project have been achieved by means of experimentation with delicate furnaces in the Delft University of Technology facilities. The experiments consisted of heat treatments in extremely low oxidation conditions. The outcome of this thesis has managed to assess the influence of the addition of an extra self-healing agent, where an interaction between tungsten and gold has been confirmed. Moreover, mechanical testing has been performed to assess the influence of deformation. A contribution to the surface precipitation theory has been gained, which will eventually help with the development of self healing alloys.

I would not have been able to achieve these results without the contribution of many people. First of all, I would like to thank my graduation committee for being able to be present for my graduation.

I would also like to thank my daily supervisor, Dr.ir. N.H. van Dijk, who knew how to deal with my desperation and kept me on my toes. His guidance and feedback have helped me to grow in the scientific world. As my supervisor, I have to thank Prof.dr.ir. S. van der Zwaag for giving me the opportunity of participating in this project. After these ten months, I have had the pleasure to get to know him and I am happy to say that I found in him an essential pillar for my thesis. Not only is his expertise was admirable, but also he always made the effort to understand me and keep my motivation until the very last moment.

Another vital person during this project is Yifan Fu. I could have never imagined to have such patient and nice person to work with. She has offered me endless help by tutoring and advising me during these hard ten months, where we have learned to overcome many obstacles. I also had the pleasure to share some experiments with Hao Yu and his steels, and with who I had really good times with the dilatometer.

As an experimental project, this thesis would have never come true without the help of all the technicians. The alloys I have been working with have been an experimental challenge, as they are extremely sensitive to oxidation. Therefore, I have to thank Hans Brouwer and Wim Sloof for their patience with the experiments and their expertise on the field which helped us to solve the oxidation problems. Also, Elise Reinton who gave me an easy access to the Brinell machine, my ally during the last month. For all the experiments related to the dilatometer, I am really grateful to Nico Geerlofs, who had the patience to guide me and teach me the tricks for such a delicate and complex machine.

Finally, I would like to deeply thank my family and friends who have managed to make me feel at ease both in Spain and the Netherlands.

Paula Martin Rojo

Abstract

Self-healing materials have recently drawn the attention of industry as a new solution to the degradation of materials. Recent progress on the field of autonomous self-healing metals has been in the line of self-healing creep-resistant steels. This is challenging due to the nanometer scale of the creep cavities and the fact that only 3D partially filled cavities can be examined to understand the phenomenon. As a consequence, valuable information is hard and expensive to acquire. This thesis proposes to study the surface precipitation phenomenon as an easier alternative to understand creep-cavity precipitation. Surface precipitation have only been studied in binary steels, therefore, the thesis focuses on the influence of the addition of a second self-healing element by studying the time evolution of gold tungsten containing iron based steels. The results provide new insights into the theory of self-healing steels, where tungsten has been found to decelerate the gold precipitation kinetics.

Contents

1

Introduction

The concept of self-healing materials has recently been developed inspired by nature. Some natural systems, such as skin and bone, are able to regenerate and restore their properties once they have been damaged. If this concept is applied to man-made materials, self-healing materials are those that are able to autonomously repair the damage occurred during service [1].

The advantages of self-healing materials are related to an increase in safety and reliability. For this reason, industry has found self-healing materials to be an attractive solution to deal with damage. So far, industries have developed engineering materials under the "damage prevention" philosophy in which they strive for delaying the formation of damage. However, self-healing materials offer the possibility of partially or fully repairing the damage, resulting in extended operational lifetimes, and thereby reducing the maintenance.

Most of the research on self-healing materials has been carried out on polymers , where the processing has been relatively easy to deal with. On the other hand, metals present the complication of high manufacturing temperatures and high mechanical properties required in commercial alloys [2].

Even though the challenge of developing self-healing metals has showed a slow progress, there is a wide interest since metals are one of them mostly used materials in industry. Metals are excellent at offering good mechanical properties, and there is a vast knowledge on how to tune their properties [3]. The properties of metals are highly dependent on the microstructure. The microstructure can be controlled by heat-treating the alloy with the right composition. Heat-treatment techniques have been improving over the years, striving for advanced alloys able to reach higher operating temperatures and loads where the degradation of metals become critical [4].

From all the self-healing metal approaches, autonomous healing materials are the most promising toward a future application in industry. Autonomous healing in metals does not require any external trigger and healing happens when the damage appears under the normal service conditions of the material. The mechanism studied here is based on alloys with a supersaturated solute that wants to segregate and precipitate, but where the nucleation energy barrier is too high to precipitate in the matrix. Therefore, when a cavity nucleates within the material, a free surface is created that has a lower energy barrier for nucleation and the solute segregates here and precipitates. As a consequence, it requires solid-state diffusion of solute atoms from the matrix to the damage site. The challenge with autonomous healing is that the temperature should be high enough to guarantee adequate mobility of the solute atoms in the matrix, while maintaining good mechanical properties degraded by temperature. As a consequence, there is a limited temperature range where self-healing can happen efficiently. The limits of this range are defined by Van Dijk and Van der Zwaag [5], with a minimum temperature of $T_{min} = 0.4T_m$ and a maximum temperature of $T_{max} = 0.65T_m$, where T_m is the melting temperature in kelvin. This temperature range is in line of creep-loaded metals, especially in the case of creep-resistant steels.

The focus of this project is on self-healing creep-resistant steels. Creep occurs in metals that operate at high temperatures ($T > 0.4T_m$), where they suffer irreversible plastic deformation under quasi-constant load smaller than the yield stress. The mechanism consist on three steps: (i) nucleation of creep cavities in the interior of the material, (ii) coalescence of cavities, and (iii) catastrophic failure due to the formation of a large crack [3]. Creep is one of the main degradation modes of engineering materials, together with fatigue, wear, and corrosion. Even though creep can result in catastrophic failure, many industries require metals to operate at these high temperatures and loads. Without the development of such advanced metallic materials, industries such as thermal and nuclear power plants, chemical and petroleum plants would not be possible, since their gas turbines have to operate under creep conditions[6].

Progress of self-healing creep-steels was firstly made on austenitic steels by Laha et al. [7] and Shynia et al. [8] with the precipitation of boron and boron nitrides in the creep cavities, respectively. It was found that the selective precipitation in creep cavities can stop their coalescence that would lead to a catastrophic failure. Posterior improvement with addition of Cu [9] was proved to not be an efficient self-healing element since the nucleation barrier in the matrix was not high enough. Most recent investigations have been performed in the field of binary ferritic Fe-X alloys. Zhang et al. [10–12] observed that Au is an outstanding self-healing element due to its large size difference with Fe atom. This resulted in a high nucleation barrier for precipitation in the matrix that is due to the large lattice strain. Fe-Au results achieved an 80% healing efficiency. However, the price and availability of Au makes it inappropriate for industrial alloys. Versteylen et al. [13] compared the self-healing efficiency of Au in Fe-X binary systems with Cu, Mo and W, and concluded that Mo and W were promising options. Zhang et al. [14] investigated Fe-Mo systems and Fang et al. [15] studied Fe-W alloys, and they confirmed that both Fe-based system could self-heal with Fe_2Mo and Fe_2W Laves phase precipitates, respectively.

The main challenge of studying the cavity-filling mechanism is the size, the location and the timescales of the process. Creep cavities occur inside the material and their size ranges between $\sim 1nm$ and $\sim 1\mu m$. Moreover, only partially filled cavities are informative and 3D studies are recommended to fully understand the mechanism. Consequently, very high-resolution instruments are necessary to monitor the process.

Sun et al. [16] found a solution to this problem by linking the free surface precipitation in the surface of the material to the precipitation inside creep cavities. This surface precipitation has recently been considered as a new phenomenon in metals, since it consist of surface precipitation in the absence of an external supply of new atoms and under vacuum conditions. Leading research groups [17, 18] define surface precipitation as a solid-state transformation that only requires a heat treatment for the precipitates to appear selectively on the surface of metal alloys. Bulk precipitation in metal alloys has been extensively studied and the thermodynamic-kinetic relations and parameters are well understood [3]. However, surfaces behave differently compared to the bulk and bulk related precipitation theories can not always be extended to surfaces. New phenomena such as surface segregation and surface chemistry play a role in the thermodynamics and kinetics of the process and are not yet well understood yet.

So far, little research on surface precipitation has been done, mostly on aluminium [17, 18] and iron alloys [16]. The results have confirmed surface precipitation as a new phenomenon, finding precipitates only at the surface and not in the bulk. These prove that the thermodynamic reasoning on which self-healing is based, with nucleation and growth of precipitates on the free surface easier than in the bulk. However, no kinetic model has been formulated yet, and only a dependence on temperature, alloy composition and precipitation has been established.

The aim of this report is to understand and predict the cavity filling for self-healing materials by studying surface precipitation. The report will be structured in four main chapters. Firstly, chapter 2 will present an overview of the knowledge in the field of surface precipitation together with the concepts this thesis has been based on. Chapter 3 will demonstrate the surface precipitation phenomenon in binary and ternary alloys. The main goal is to provide more experimental data that could contribute to the understanding of the phenomenon. Chapter 4 will go further into an experimental creep steel, designed to be self healing under creep loading, in order to observe the precipitation on potentially commercial creep steels. Finally, chapter 5 will bring all the observations together to give conclusive results.

2

Surface precipitation

As already presented in the introduction, the focus of the thesis is on surface precipitation related to cavity filling on self-healing steels. Recently, surface precipitation has been defined as a new phenomenon [17, 18] that simulates the creep-cavity vacuum conditions where only atoms that come from the bulk will form the precipitate. It is well-known that three requirements are necessary to precipitate selectively at the surface[14, 19]: (i) high mobility and segregation tendency towards the surface, (ii) driving force to precipitate, related to the the chemical driving force and strain energies, and (iii) selective nucleation and growth at the free surface due to high energy barrier to precipitate in the bulk.

Surface precipitation is a recent field of research in which theory has yet to be developed. The focus of this chapter is to summarise the most relevant concepts of surface precipitation related to cavity filling on self-healing creep-steels in which this thesis has been based on. The studied surface precipitation will consider that the atoms that form the precipitates come from the bulk of the material under vacuum conditions. This means that no atoms will be provided from any external source and no interaction with external environment will be considered.

Surface precipitation is a product of two phenomenons, surface segregation and precipitation. This chapter will gather the most relevant concepts from surface science and precipitation thermodynamics and kinetics.

2.1. Surface Segregation

Surface segregation can be defined as the preferential enrichment of the surface with one component of a multicomponent system [20]. As a consequence, surfaces have a different chemical composition to the bulk and can be considered as a different phase of constant thickness. During surface segregation there is an energy cost of replacing a solvent atom from the surface with a solute atom from the bulk. Roussel, Treglia and Legrand [21] propose the Tight-Binding Ising Model (TBIM) to calculate the surface segregation phenomenon for binary alloys, and it has been proved that it is a simple model that has accurately predicted surface segregation energies in dense surfaces. The TBIM states that there are three main driving forces that can cause a solute atom to segregate to the surface: surface, size, and alloying effect. All of them depend on the surface crystal orientation and structure, therefore, they take into account the atomic and lattice relaxation. The surface effect is related to the surface energy of the elements. Those with lower surface energy will segregate. The size effect is directly related to the strain relaxation of the lattice. The larger the difference in size, the higher the driving force will be to segregate the big atom to the surface. Finally, the alloy effect is related to the solubility of the solute element, which is determined by the phase diagram. The tendency of the solute to dissolve or form a separate phase decides if the solvent or solute segregates, respectively.

Roussel et al. [21] conclude that this simple formulation of the segregation energy in three independent factors is helpful when there is a strong competition between the elements to segregate. However, it should be noted that system variables such as temperature [11, 22], element concentration and imposed strain could modify the segregation tendencies.

Figure 2.1 shows a map with Roussel's results. It is interesting to pay especial attention to the segregation tendencies of the most important self-healing systems when looking at figure 2.1. Versteylen et al. [13] have studied the self-healing efficiency of the four most efficient self-healing alloys: Fe-Au, Fe-Cu, Fe-Mo and Fe-W. The study concludes that Fe-Au presents exceptional self-healing properties, Fe-Mo and Fe-W also have good self-healing capacity, whereas Fe-Cu presents the lowest efficiency. If these results are compared to the segregation tendencies, it can be observed that Au has strong solute segregation due to size and surface effect. Mo and W do not present strong solute segregation, since there is a competition between the solvent segregation tendency due to surface effect and the solute segregation due to size effect. Cu has as a strong solute segregation tendency as Au. Therefore, it can be seen that the surface segregation tendency is in line with the efficiency of the self-healing agent except for Cu. However, the reason for this exception has been attributed to the low energy barrier to precipitate in the matrix for Cu precipitates in Fe-Cu alloys and not to segregation [11].

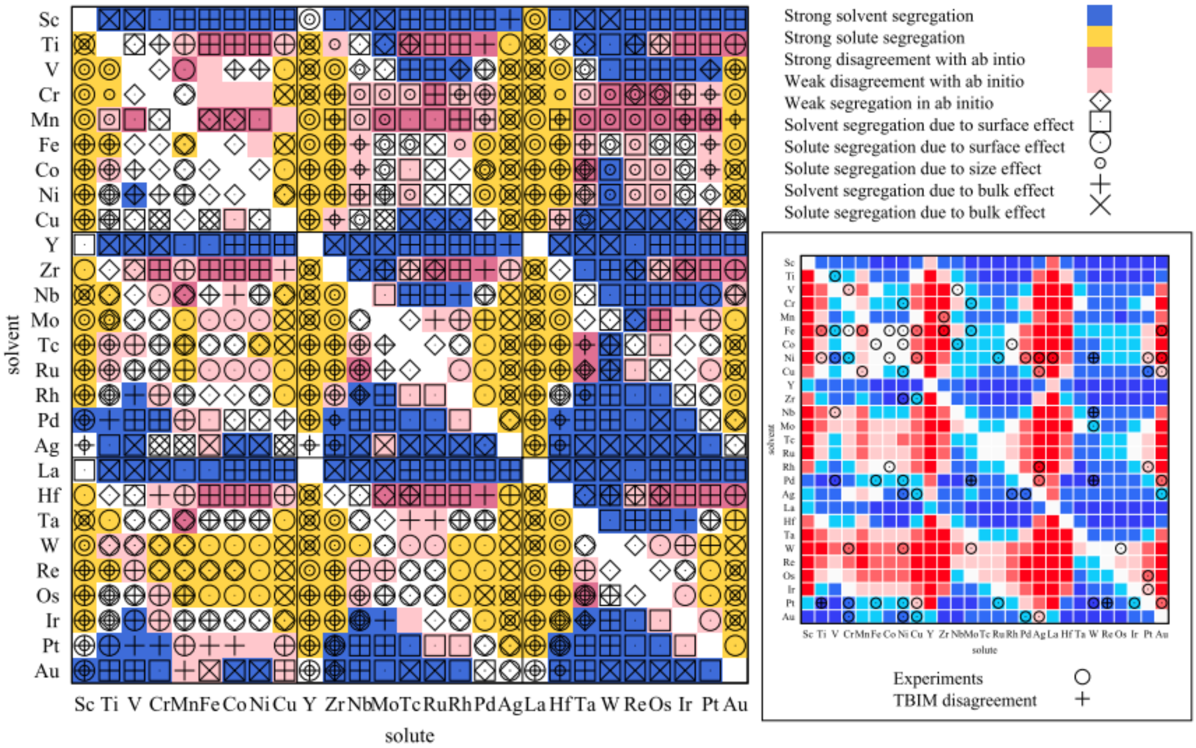

Figure 2.1: Surface segregation TBIM map results compared to ab-initio theory (colours). In blue and yellow the two approaches agree in the prediction. The violet and pink indicate a disagreement in the theories where the TBIM does not show tendency while the ab-initio expects a strong solvent or solute segregation. The TBIM theory is also compared to experimental data (symbols) and the ⊕ symbols indicate some mismatch between the TBIM and these data[21].

Uebing [20] adds that cosegregation of several elements can occur in case of ternary or more complex alloys. Strong chemical interaction, such as changes in binding energy, can cause simultaneous segregation of two elements. Temperature is a decisive parameters that dictates the desegregation of one element and the segregation of another [22]. This means that some elements only segregate to the surface for a limited range of temperatures. Therefore, if the temperature is in this range, the solute will segregate to the surface, otherwise it will desegregate and dissolve into the bulk. As a consequence, surface precipitation is influenced since precipitates could be dissolved. Also Eltester et al.[23] make reference to cosegregation by claiming that it can be encouraged by the presence of attractive force between the two solutes. Additionally, these attractive force can also end up forming surface precipitates depending on the phase diagram, but mostly for high solute content and a low temperature.

Surface segregation could be a decisive factor in surface segregation as it could increase the supersaturation of an element in the surface and increase the precipitation driving force.

2.2. Precipitation Thermodynamics

Precipitation is a type of solid-state phase transformations where a phase different from the matrix forms in the bulk or defects of the crystal lattice. As a phase transformation, it is a thermodynamic process which requires long range diffusion and thermal activation.

In order to better understand precipitation, it should be noted that a solid solution can exists as one phase or a mixture of different phases. The amount of phases that are present in a solution is defined by the thermodynamic equilibrium of the system and Gibbs free energy (G) is commonly used to define this equilibrium. A system is in thermodynamic equilibrium when the Gibbs energy is minimum, in other words, the driving force in a phase transformation in metals is the change in the Gibbs energy ΔG [24].

Surface precipitation deals with heterogeneous multi-component alloys, where at least two phases are present (α and β), composed of at least two types of atoms (A and B). In these systems, the calculation of the Gibbs free energy of the system is done by Gibbs curves of the phases that compose the system. The bulk Gibbs free energy for each phase are calculated by taking into account the mixing enthalpy and entropy [24]. However, the surface Gibbs free energy for the same phase need a separate calculation because two additional phenomena take place in the surface: (i) the surface has a different composition to the bulk due to segregation, and (ii) the surface has a higher free energy due to the loose bonds [17].

This difference between the Gibbs free energy in the surface and the bulk results in precipitation phases in the surface at temperatures where is not possible in the bulk. Furthermore, precipitation can also be impeded in the bulk if the chosen solute atoms are too big, and there is a nucleation energy barrier due to the high strain of the change in volume of the big precipitate in the matrix [25].

Uebing [20, 22, 26] observed that an epitaxial growth (2D) is the first step towards the nucleation of surface precipitates (3D), which is identified as a metastable precipitation sequence. This epitaxial growth was seen to be more stable than 3D precipitates in the bulk since the epitaxial arrangement leads to additional bonding between the substrate and segregated atoms. In these cases, the equilibrium precipitation does not occur directly, but through intermediate precipitates called metastable, whose composition differs from the equilibrium. The precipitation of the metastable sequence is influenced by three energies: bulk enthalpy, interface energy and strain energy. The sequence follows a monotonic loss in bulk enthalpy and increase of interfacial energy. The strain energy evolves parabolically: it starts to increase as the coherent precipitate grows, due to the efforts to accommodate the coherency; it reaches a maximum when the precipitate loses coherency, and when the precipitate becomes incoherent the strain energy is minimum[27].

2.3. Precipitation Kinetics

Nucleation and growth of precipitates are processes governed by long range diffusion. Diffusion is a thermally activated process by which atoms and molecules are able to move within the material, and as such, it obeys Boltzmann statistics formulated by Arrhenius kinetics. The diffusion is quantified by the diffusivity (D), which depends on the migration activation energy Q_D, the probability of having a free adjacent vacancy and making a successful jump D_0, and temperature T.

An important parameter to take into account when dealing with diffusion problems is the diffusion length of the atoms in the material, given by ($x_{dif} = 2\sqrt{Dt}$), where t is the time. The diffusion length, classifies the diffusion problem into inexhaustible and exhaustible, where the case of surface precipitation on bulk samples is inexhaustible. In addition, there are preferential diffusion paths where atoms diffuse faster than in the lattice due to a lower activation energy. In the case of surface precipitation, surface and grain boundary diffusion are the main preferential paths [24].

Nucleation can be defined as the formation of a critical-sized volume (r^*) of atoms with the composition and structure of a new phase, called nuclei [3, 24]. The critical radius r^* is defined in equation 2.1 for the case of homogeneous nucleation, where there is no particular initiation site for nucleation. It is the minimum radius that the cluster has to achieve in order to generate a stable nuclei. This critical radius is obtained as a results of differentiating the variation of Gibbs free energy for homogeneous nucleation (see equation 2.2) where (V) is the volume of the precipitate, and ΔG_V is the volume free energy reduction due to the formation of a new phase that is stable in the phase diagram. The second contribution is the interface free energy γ. It is related to the interface that it is created between the matrix phase and the new phase α/β of area A. The last contribution, also multiplied by the volume of the precipitate, is related to the change in volume of the new phase, which generates a misfit strain energy ΔG_s in the matrix.

$$r^*_{hom} = \frac{2\gamma}{(\Delta G_V - \Delta G_s)} \tag{2.1}$$

$$\Delta G_{hom} = -V\Delta G_V + \Sigma_i A_i \gamma_i + V\Delta G_s \tag{2.2}$$

Figure 2.2 shows the variation of the Gibbs free energy with the radius of the particles, since the surface and volume are dependant on the radius. It can be observed that up to r^* the disintegration of the cluster is more favourable. Moreover, it can be seen that the driving force for precipitation that comes from the phase equilibrium (ΔG_V) is reduced by the interface and strain energy ($A\gamma + \Delta G_s$).

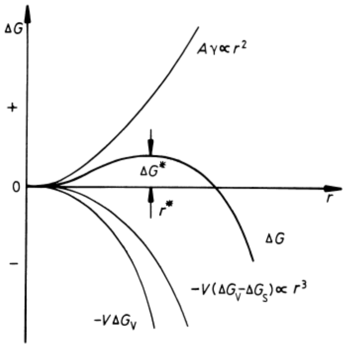

Figure 2.2: Variation of the ΔG_{hom} with the radius of the nuclei [24].

By definition, surface precipitation consists of heterogeneous nucleation due to the site-selective requirement. The variation of Gibbs free energy associated to heterogeneous nucleation is presented in equation 2.3. The equation can be divided in three different contributions. The first three contributions are the same as in the homogeneous nucleation. In the case of surface precipitation the misfit strain energy could be ignored as the precipitate will nucleate on top of the surface and not in the middle of the matrix.

The last contribution, ΔG_d, is characteristic of heterogeneous nucleation. It accounts for the destruction of the defect's free energy. The defect in the material, such as dislocations, grain boundaries and free surfaces are high free energy locations. The nucleation of a precipitate in these locations means destroying part of the defect that had a high free energy, which means that the reduction of free energy associated to heterogeneous nucleation would be higher than for homogeneous. Moreover, these defects are also space to precipitate which can reduce the misfit strain energy ΔG_s. As a consequence, heterogeneous precipitation is going to be preferable and most likely to occur in practice.

$$\Delta G_{het} = -V(\Delta G_V - \Delta G_s) + \Sigma_i A_i \gamma_i - \Delta G_d = -V(\Delta G_V - \Delta G_s) + A_{\alpha\beta}\gamma_{\alpha\beta} - A_{\alpha\alpha}\gamma_{\alpha\alpha} \tag{2.3}$$

Surfaces are a preferred location for heterogeneous precipitation. The most likely sites to nucleate in the surface are in the kinks, since they are the sites with most unsatisfied number of bonds. Also ledges and terraces are high potential sites. The number of kinks in a surface can change depending on the surface orientation, and therefore this is going to influence the nucleation rate. Those surfaces with the orientation with the maximum number of kinks will have the fastest nucleation rate [28].

In addition to the destruction of these high energy interfaces, the nucleation and growth of the precipitates could be encouraged if there is a orientation relationship between the matrix and the nuclei. If they form a low-energy coherent interface, then the energy reduction is bigger. In this case, the shape of the precipitates will obey Wulff construction [28].

The nucleation rate depends on two factors: diffusion of the atoms in the material, where the migration activation energy and the atomic vibration are key parameters, and the energetic barrier for nucleation. Surface precipitation requires that the barrier for nucleation in the bulk is high enough to impede the precipitation in the bulk. This energy barrier is defined by the sum of: (i) the volume free energy reduction due to the formation of a new phase, previously referred as the driving force for precipitation, (ii) the balance on the surface free energy from the destroyed and new interfaces, (iii) the misfit strain energy of the new precipitate (~ 0 for precipitation in the surface), and (iv) the destruction of the defect's free energy. As aforementioned, temperature will govern the nucleation process through the undercooling degree. The precipitation driving force is the most sensitive parameter to the undercooling, as it defines a critical undercooling below which no nucleation occurs [24]. However, a high undercooling can also result in barrier-free nucleation according to a recent study from Van Dijk et al. [29]. It was observed that when the nucleation activation energy is comparable to the thermal agitation, the nucleation barrier vanishes, which is the case for large undercoolings and solid-state transformations in which the net interfacial energy is really small. No energy barrier results in bulk precipitation, which is undesirable for self-healing. As a consequence, there is a temperature range in which surface precipitation can occur.

The growth of the precipitate defines their shape and size. The size will depend on the diffusivity. Zener's theory proposes a model for precipitation in the bulk in which the radius grows proportionally to $(Dt)^{1/2}$, where D and t are diffusivity and time, respectively. Carlow and Zinke-Allemang [30] proposed a a growth rate based on the Ostwald ripening theory that accounts for the surface and in their model the radius increases proportionally to $(Dt)^{1/4}$.

The shape of the precipitates depends on the relative migration rate of the interfaces, which is related to surface energies and concentration gradients. Semicoherent interfaces have lower energy than incoherent ones; therefore, the system will prefer to maximize the semicoherent surface and minimize the incoherent surface and consequently, incoherent interfaces have higher mobility. Therefore, depending on the coherence of the interfaces of the precipitate, the shape can vary from equiaxed to plate-like.

As aforementioned, precipitates will have a tendency to nucleate in defects due to the free space to accommodate the precipitate and the destruction of the defect energy. Moreover, the growth of particles in these defects it is also going to be faster than in the bulk. The growth in the bulk is limited by the volume diffusion. However, defects such as grain boundaries, dislocation or surfaces, are preferential paths for substitutional diffusion, which means that the diffusion in faster. Therefore, The growth of these precipitates, called allotriomorphs, can be separated in three steps: (i) volume diffusion of the solute to the preferential path, (ii) diffusion along the preferential path, and (iii) diffusion along the α/β interface, which is normally a high energy site, and thus, the diffusion is also faster. This will be the case in surface precipitation.

2.4. Spherical Indentation

As state in the previous section, mass transport to the surface is crucial for surface precipitation. The atomic transport is greatly accelerated by the presence of dislocations. There are several ways to create and vary the local dislocation density in the material. In this thesis work, spherical local indentations at different loads have been performed to create locally different dislocation densities in an unstrained sample and prior to the heat treatment.

Spherical indentations have been considered an interesting tool to obtain the plastic properties for metals as they simplify the experimental procedure by reducing the amount of indents. Unlike conical indentations, spherical ones do not depend on the apex angle and there is a one-to-one correspondence between the conical impression and the depth-radius ratio [31].

However, the strain field is hard to study and contradictory results have been observed in the literature regarding the strain-hardening and strain field distribution around the spherical indentations. Many attempts have been made, mostly in copper, to determine the surface hardening around a spherical indentation.

For the purpose of this thesis, the work done by Chaudhri [32, 33] has been taken into account. The equivalent plastic strain distribution around a spherical indentation is calculated, as shown in figure 2.3. In spherical indentations, the strain is defined by the dimensionless parameter a/R, where a is the radius of the indent and R is the radius of the sphere. It has been observed that there is a transition in the strain distribution depending on the a/R. For indentations where $a/R < 0.1$ the maximal strain is around $\sim 0.5 - 0.8a$, whereas for $a/R > 0.15$ the maximal strain is in the centre of the indent [33]. Figure 2.3 shows the distribution for $a/R > 0.15$ indents since the maximal strain is in the centre, and the strain distribution is not spherical but elongated along the load axis.

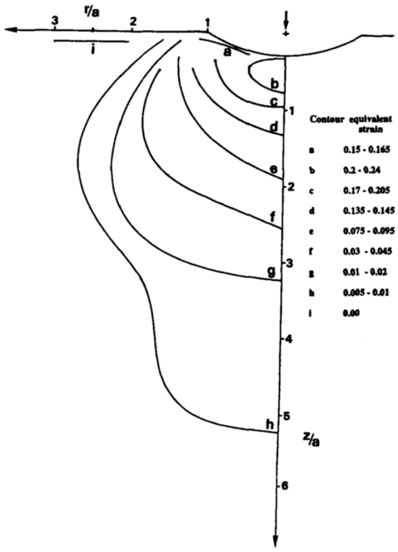

Figure 2.3: Strain field around a spherical indentation [32].

2.5. State of the art

Surface precipitation on aluminium alloys has been studied mainly by Chen at al. [17] and Vu Dinh [18], where a uniform distribution of precipitates and a uniform precipitation among all the grains was observed. Moreover, it was found that the precipitate surface coverage was ~ 25 times higher than the fraction estimated for the bulk. Chen et al. [17] studied the influence of temperature and cooling rate in Al-Si binary and Al-Si-Ge alloys. Vu Dinh et al. [18] studied mainly the influence of temperature in more Al-Zn-Mg complex alloys, where they observed precipitation of two precipitates of different composition.

Regarding temperature, both groups agree that increasing the degree of undercooling increases the number density and reduces the average size. Chen et al. observed that bimodal precipitation appeared for large undercooling and that the composition of the precipitates also changed with temperature for ternary alloys. Regarding the effect of undercooling, Chen et al. showed that increasing the cooling rate has the same effect as increasing the undercooling, and that the increase of the cooling rate decreased the activation temperature of a bimodal precipitation.

Surface precipitation on steels has been studied mainly by Sun et al. [16] and Zhang [34] on binary iron-gold alloys who observed the influence of the degree of undercooling. Regarding nucleation, it was found that precipitates were distributed in a pattern, preferring to nucleate along the facets formed during the heat treatment. As for growth, the shape of the precipitates was irregular due to the anisotropic growth, where they also grew inwards. Sun et al. observed that the radius grew proportionally according to Zener's theory ($r \propto (Dt)^{1/2}$). Both the nucleation and growth of the precipitates changed from grain to grain. This means that they depend on the orientation and topology of the grain, which affects the relative migration rate of interfaces.

Zhang [34] studied the influence of prior deformation by indentation prior to the heat treatment of Fe-Au and Fe-Au-B-N. It was observed that only the alloy containing B and N showed a tendency for Au-rich precipitates to nucleate in the indentation, which suggests that B and N interact with dislocations and increase the Au driving force. In the same study, Zhang studied the influence of deformation by applying pre-strain to the alloys. It was found that the pre-strain increases the dislocation density. In Fe-Cu and Fe-Au alloys, precipitates nucleated in the dislocations, and also for Fe-Mo it accelerated the nucleation and growth of precipitates.

The remaining relevant research for surface precipitation comes from the results from creep experiments. The only useful information that can be applied to surface precipitation is observed in the partially-filled cavities. As already claimed by Versteylen [13], Fe-Mo an Fe-W are also promising self-healing alloys. The precipitation in Fe-Mo [14] and Fe-W alloys [15] during the creep test showed Laves phase (Fe_2Mo, Fe_2W) precipitates that nucleated selectively on the grain boundaries, creep cavities. In the case of Fe-Mo alloys, it was also observed that there was additional nucleation on deformation bands, especially on the triple junctions.

It was confirmed that Mo segregated to the grain boundaries, and that the orientation of the Fe_2Mo precipitates was related to the Fe substrate. Zhang et al. [11] also observed a relation between the Au-rich precipitate and the Fe matrix, where the precipitation seem to prefer the coherent interfaces.

Fang et al. [15] observed that the number density of W-rich precipitates per cavity and per cavity area remained constant for a given creep load, and the number density was higher for a higher load. The results were ~ 0.5 and ~ 0.65 precipitates/cavity, and $\sim 2 * 10^{10}$ and $\sim 6 * 10^{10}$ precipitates/cavity area [m^{-2}] for 140 MPa and 160 MPa respectively. This was correlated to the dislocation density, which remained constant for creep stage II. A higher load generated a higher dislocation density and higher number density of precipitates per cavity. Therefore, Fang et al. concluded that there is a relation between the degree of deformation and the precipitates number density.

Fang et al. [15] described the growth rate of the precipitates by as $< V >= kt^n$, where <V> is the precipitate average volume, k and n are constants, and t is time. The experimental results showed that the exponent n=0.8, which fitted with previous computational results. This exponent is depends on two factors: (i) the ratio between the spacing between the cavities and the cavity radius, and (ii) the ratio between the bulk and grain boundary diffusivities. The volume is proportional to the r^3, where r is the radius; therefore, the relation found by Fang is equivalent to $< r >\propto \ t^{0.8/3} \propto ^{0.26}$.

Finally, Fang concluded that the growth of the precipitates is limited by grain boundary diffusion. This grain boundary was evident because there where depleted zones of W around the grain boundaries limited by the bulk diffusion of W. The experiments confirmed that the calculated bulk diffusion length coincides with the W depleted zone.

3

Surface Precipitation on Binary and Ternary Alloys

The aim of this chapter is to evaluate surface precipitation on binary and ternary alloys as an alternative option to study the self-healing mechanism at creep-induced damage in steels. This chapter starts with the motivation of this set of experiments. Secondly, a detailed description of the set-up of the experiments will be presented. It will be followed by a discussion of the results from the binary and ternary alloys. Together in this section, the role of the unwanted oxidation layer will be examined. Additionally, the results from the final experiments on the binary and ternary alloys will be presented.

3.1. Motivation on Experiments Binary and Ternary Alloys

Most of the research on self-healing of creep-damaged alloys has been carried out by Delft University of Technology, who have observed effective autonomous healing properties in Fe-Au alloys [12]. In view of the scarcity of gold, which limits its application in industry, the latest research trends have proposed promising alternatives as healing agents such as Mo and W. Mo and W are healing agents that form Fe_2Mo and Fe_2W Laves phase precipitates [13]. Both elements are efficient self healing agents that have shown preferential precipitation in creep cavities [14, 15]. By comparing Fe-W to Fe-Mo alloys, there are two slight differences. Tungsten improves the solid-solution strengthening better than molybdenum. However, the diffusivity of tungsten is slower than molybdenum's in the BBC matrix of iron, which can slow down the kinetics of the precipitation [14]. Taking these into account, tungsten has been selected as the ternary element to study due to its relevance in creep-steels.

Based on these previous studies, two alloys were selected as study objects. Fe-Au has been chosen as the binary steel as the as gold-rich precipitates kinetics fit with the time scale of this thesis work. Within only 30 minutes of ageing, relevant surface precipitation can be obtained [16]. Moreover, some research has been already carried out on Fe-Au surface precipitation by Sun et al. [16], at different ageing temperatures and short times. Thus, it is the self healing alloy that has been researched the most and therefore, the best option to be the alloy to compare the ternary results with. For this reason, this thesis will be focused in the continuation of the research by evaluating the time evolution of Au-rich surface precipitation and to become a reference system to compare the new experiments on ternary alloys.

Fe-Au-W will be the ternary alloy. The experiments on Fe-Au-W have been designed with the idea to study the interaction of two self-healing agent. This is based on previous observation on the addition of B and N in Fe-Au-B-N steels, which has modified the behaviour of Au-rich precipitates by retarding its precipitation [10, 11].

Finally, strain fields have been introduced in the samples by means of indentation in order to assess the relation between the strain field and precipitation. Based on previous research at the Delft University of Technology by Zhang [34], Knoop indentation in a Fe-Au alloy and aging 64 hours at 550ºC showed no selective precipitation of Au-rich precipitates. The size of these precipitates is nano-scale and they are found all over the matrix in the indented region. However, with the addition of B and N bigger Au-rich precipitates were found to precipitate in the indentation valley. This behaviour of gold precipitates shown in figure 3.1a. Moreover, within the same research group, Szymanski performed Vickers (conical) indentation in Fe-6W alloys that were subsequently aged for 140h at 600ºC. The results, presented in figure 3.1b, show that there is precipitation of rectangular shaped W-rich precipitates, but they do not precipitate selectively on the highest deformed areas [35]. It can be concluded that precipitation is expected for Fe-Au alloys and it is doubtful for W-alloys because the alloy will contain a lower atom percentage of tungsten (less driving force) and the ageing cycle will consist on shorter times. The innovation of these experiments relies on the spherical shape of the indents. Spherical indentation is different from conical indentation because it is independent of the apex angles and one indentation is enough to obtain the plastic properties of a specimen at different depths [31]. Consequently, in only one experiment a strain gradient can be observed in the surface of the indentation and a variety of crystallographic orientations are exposed, whereas in Vickers or Knoop indents only one crystallographic plane is exposed in the surface.

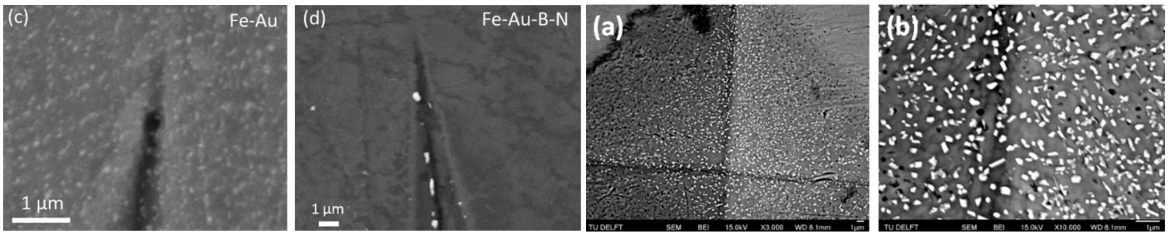

(a) Comparison of Knoop indentation on Fe-Au and Fe-Au-B-N alloys [34].

(b) Precipitation on diamond indentation on Fe6W alloy [35].

Figure 3.1: Surface precipitation on a (a)Knoop indentation on Fe-Au and Fe-Au-B-N alloys, and (b) on a diamond indentation on Fe-6W alloy. These results are part of the research carried out by Zhang [34] and Szymanski [35], respectively.

In conclusion of all this previous research, some hypotheses have been formulated and expected to be confirmed with the experiments. During the analysis of the results in sections 3.3 and 3.4.2, the following hypotheses will be considered:

1. The evolution of the precipitates with time is expected to follow a power law relationship between the precipitates radius (r) and the ageing time (t) as follows:$r = c * t^n$. The exponent is expected to be close to n=0.26, as observed by Fang with the growth of the precipitates in creep-induced cavities [15].
2. The observations on the kinetics of the binary Fe-Au system has proven that short times are enough to observe surface precipitation [16]. The ageing times proposed in this thesis are relatively large for Au-rich precipitation, and therefore, coalescence of Au-rich particles is expected.
3. Based on the patterns of Au-rich precipitation observed by Sun [16], a deeper analysis of these patterns is thought to give more insight on the possible origin of these patterns. The main reasons that have been considered until present are surface facetting and crystallographic orientation of the grains.
4. Based on the fact that the diffusivity of W is much lower than Au, the formation of the Laves phase is expected only for longer times.
5. Regarding the the ternary Fe-Au-W alloy, an interaction between Au and W can be expected of the type:
   - Acceleration: the introduction of W accelerates the precipitation of Au-rich precipitates.
   - Zero: there is no interaction between Au and W and the precipitation of Au-rich particles remain the same with and without the presence of W.
   - Deceleration: the introduction of W decelerates the precipitation of Au-rich precipitates.
   - Other: Some other unforeseen interaction takes place.

3.2. Experimental Set-up

The materials that have been studied are high purity Fe-based binary and ternary alloys manufactured by Goodfellow whose composition is listed in table 3.1. The raw materials were produced as a rolled sheet that were cut by spark erosion into small plates with dimension of ~ $17.5x8x0.5mm^3$.

The samples have been polished and cleaned by an ultrasonic bath with ethanol prior to the heat treatment. Four different set-ups have been tested until the definitive set-up has been reached.

Table 3.1: Chemical composition of binary and ternary Fe-based alloys (wt%) and lower transformation temperature (A_1).

Alloy (wt%)	**Au**	**C**	**N**	**B**	**Fe**	A_1
Fe-3Au	2.87	0.0008	0.0085	<0.01	Balanced	868°C
	Au	**W**			**Fe**	A_1
Fe-3Au-4W	3.073	3.826			Balanced	800-930°C

The first two set-ups that were used resulted in oxidized samples and therefore, these are regarded as preliminary experiments. Set-ups 1 and 2 took place in an alumina and silica electric-resistance furnaces. The samples were placed in a corundum crucible and a quartz boat in the alumina and silica furnaces, respectively. The alumina furnace has a heating rate of 100 °C/h and a cooling rate of 10 °C/min, whereas the silica furnace, due to its smaller size, could be heated up at a faster rate of 10 °C/min and cooled at the same speed. Prior to the heat treatment, both of the furnaces have been fluxed with a mix of 10% hydrogen and argon, previously filtered, in order to obtain a protective atmosphere and prevent oxidation of the samples. The flux of the gas mixture prior to the heat treatment is 0.5 L/min. Due to the oxidation problem, a titanium getter located inside the chamber next to the samples was used, but it was unsuccessful.

Set-ups 3 and 4 were performed in the final furnace set-up as the samples were not oxidized. This final set-up consists of the same silica electric-resistance furnace as set-up 2, where the gas mixture is also fluxed for two hours before the heat treatment. However, this time flux of argon goes through one filter and an extra furnace heated to 800ºC where there is titanium powder as a getter to remove all the oxygen present in the argon. Moreover, there is a bypass for the hydrogen to avoid heating it to 800ºC for safety reasons [36]. Additionally, one extra step is performed prior to the heat treatment: the chamber is pre-heated at 200ºC for 1 hour, so that the oxygen attached to the silica walls gets fluxed away [37].

The difference between set-ups 3 and 4 is that in 3, the annealing and the ageing of the samples occurs in the definitive furnace. However, set-up 4 splits the heat-treatment in two. Firstly, the annealing is performed in a separate vertical furnace where the sample is contained in a silica tube with filled with argon and then is quenched in water. This is done to lower the risk of oxidation at high temperatures (868ºC). Then, the samples are polished and cleaned and aged in the definitive furnace. Table 3.2 presents a summary of the different set-ups.

Table 3.2: Heat treatment and respective experimental set-up for all the experiments on binary and ternary alloys.

Set-up		**Treatment**	**Furnace tube**	**N° filters**	**Gas**	**Getter**
1	a	Pre-annealing and ageing in the same furnace	Alumina	1	$10\% H_2 + Ar$	-
	b			2		Ti
2		Pre-annealing and ageing in the same furnace	Silica	2	$20\% H_2 + Ar$	-
3		Pre-annealing and ageing in the same furnace	Silica	1 + extra furnace	$10\% H_2 + Ar$	Ti
4		Pre-annealing **in a separate** furnace	Silica	1 + extra furnace	$10\% H_2 + Ar$	Ti

The heat treatment performed to obtain surface precipitation consisted of two parts. First, the samples have been annealed in the single α iron phase in order to obtain homogenise and solutionize the supersaturated solutes (Au and W) in the iron matrix. In the second part, the samples have been aged isothermally. The ageing temperature has been chosen to be 700ºC, which results in a good combination of driving force and incubation time that will enable to observe the evolution of precipitation in an appropriate time scale for this thesis. The summary of the different thermal treatment that have been applied are summarised in table 3.3.

Table 3.3: Summary of the heat treatments for FeAu and FeAuW alloys.

Nº	Annealing	Ageing	Alloy	Set-up
1	900°C-24 hours	700°C-0.5 hour	FeAu and FeAuW	1.a
2		700°C-10 hour	FeAu	1.a
3	868°C-8 hours	700°C-0.5 hour	FeAu and FeAuW	2
4		700°C-8 hour	FeAu and FeAuW	1.b
5		700°C-1 hour	FeAuW	4
6		700°C-2 hour	FeAu, FeAuW and FeW	3
7		700°C-2 hour	FeAu, FeAuW and FeW	4
8		700°C-16 hour	FeAu and FeAuW	4
9		700°C-32 hour	FeAu and FeAuW	4

The heat treatments have been designed based on the previous work of Zhang, Fang and Fu. Regarding the annealing step, based the work of Zhang Fe-Au alloy can be annealed at 868°C for 5 hours [34]. Fang calculated that Fe-Au-W annealing temperature is located between 800-930°C since Thermocalc calculations indicate that this is the single α-iron region for Fe-4W (wt%) [19]. Fang performed a surface precipitation experiment with Fe-Au and the procedure consisting of an annealing at 900°C for 24 hours. The first experiments were chosen to replicate Fang's set-up, and for this reason, the annealing temperature and time were maintained at 900°C for 24 hours. Later on, Fu studied more in depth the homogenization temperatures of Fe-Au-W trying to obtain a fully homogenized sample in order to be able to perform subsequent creep test on these samples. The result obtained was that 860°C for 8 hours resulted in a fully solutionized alloy . This combination of Fe-Au-W annealing time and temperature coincides with the requirements for the Fe-Au alloy. For this reason, the heat treatments for surface precipitation were re-designed to have an annealing temperature of 868°C for 8 hours and both samples were tested together.

For the ageing step, the aim of this report is to assess the the evolution of surface precipitation with time, and therefore, the ageing time has been varied. The particle diffusional growth it is known to follow a power law with time as $r = c * t^X$ [30, 38], where r is the radius of the precipitate, c a constant and t the time. Therefore, the time has been chosen to follow a 2^X sequence. Figure 3.2 presents a graphical summary of all the heat treatments with their corresponding set-up.

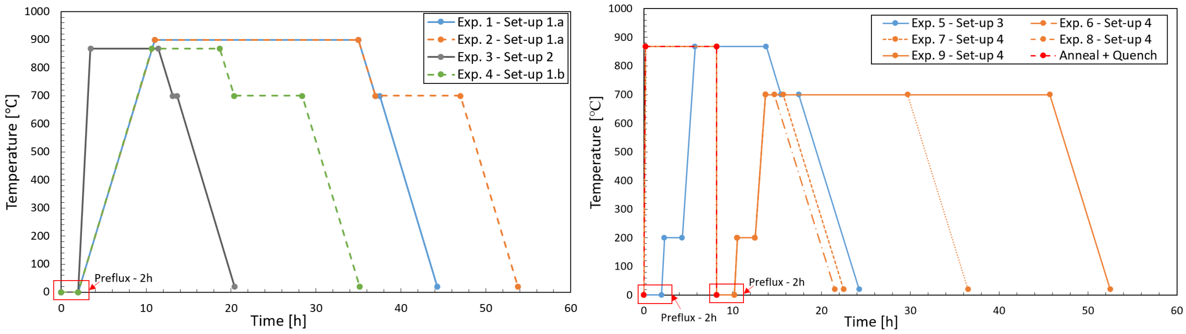

(a) Preliminary heat treatments.

(b) Final heat treatments.

Figure 3.2: Heat treatment for surface precipitation on Fe-Au, and Fe-Au-W alloys.

Secondary Electron Microscopy (SEM, JEOL JSM 6500F) coupled to Energy Dispersive Spectroscopy (EDS) was used to analyse the samples after the heat treatment. Both the surface of the precipitates and the cross sections have been assessed. The samples were only cleaned by an ultrasonic bath with ethanol before analysing the surface precipitation. However, in order to examine the cross section, the samples were polished and cleaned with an ultrasonic bath with ethanol. Finally, the processing of the images has been done with the software ImageJ, with which it has been possible to assess the number density, average diameter and areal coverage of the precipitates.

3.2.1. Supplementary Experimental Analysis on binary and Ternary Alloys

Together with the evolution of time, the influence of local deformation has been assessed. The deformation has been done by indentation with the ZHV30 ZWICKI-LINE Hardness tester with the Brinell indentor. The indentor used was a ball of 2.5 mm diameter, the speed of the load application was $80 \mu m/min$, the removal speed was $5 mm/min$ and the load holding time was of 10 seconds. The indentations have been done in the binary and ternary samples that have used set-up 4. There are two ways to control the indentation in a hardness test: by setting the maximal load or the maximum depth. Since these samples are very thin (≈ 0.5 mm thick), maximum depth was chosen in order to avoid going through the sample. Figure 3.3 shows the scheme of the indentations where it can be observed that three indentations were performed in each sample at three different depths: 45, 90 and 180 μm. The three depths were chosen according to the grain size of the samples (∼ 100 μm after annealing): one much smaller, one in the order of the grain size and the last one larger. The samples have been indented after the annealing and mechanical polishing and before the ageing.

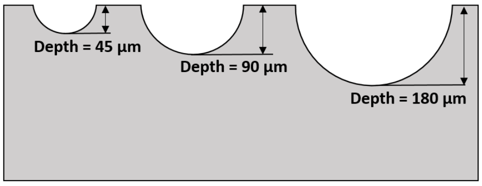

Figure 3.3: Scheme of the indentations performed in the samples with the Brinell Hardness tester.

Moreover, in order to understand the interaction between the two alloying elements in the ternary alloy, further experiments have been done.Electron Back-scatter Diffraction (EBSD) was performed in the ternary alloy in order to investigate the relationship between the precipitates and the crystal orientation of the iron matrix.The EBSD was performed after the heat treatment on the alloy that was aged for one hour in the set-up 4. The step taken for the EBSD was 3 μm for a short time (∼ 1 hour).

Additionally, TEM analysis on FeAuW was performed on creep failed samples. A FEI cubed Cs corrected Titan was used for analysis. The elemental analysis was done with an EDX detector X-MaxN 100TLE. For lattice images a Gatan camera was used. In scanning mode (STEM) ADF (Annular Dark Field) images are collected. For elemental mapping the EDX spectrum is collected for each beam position in a STEM image. For this, the plates were polished to about 20 nanometer thickness.

3.3. Preliminary Results and Discussion

The experimental results from the preliminary set-ups have resulted in a oxide layer on top, and around the precipitates. This indicates that surface precipitation on the Fe-Au and Fe-Au-W alloys is a delicate phenomenon that requires to have control of the furnace atmosphere in order to avoid oxidation of the samples. According to the Ellingham and Richardson diagrams, the most delicate system is the reduction of tungsten $W \rightarrow WO_2$ with a partial oxygen pressure of $PO_2 \sim 10^{-22} atm$ [39]. All of the different set-ups used in the experiments (1.a,1.b and 2) were designed to solve the oxidation in the chamber and reach the low oxygen pressure, which is complicated since even the high-purity argon supply contain traces of 5 ppm of oxygen [40].

Nevertheless, the oxidized samples have been analyzed. According to the study of Ostwald ripening of copper in tantalum substrates on different furnace conditions it was observed that the cluster growth kinetics was slower in those samples that had been oxidized in a forming gas atmosphere (H_2) compared to those with no oxidation [41]. Therefore, the results from the preliminary experiments can be informative about the phenomenon, bearing in mind that the growth kinetics is slower than in the real non-oxidized case.

3.3.1. Surface Precipitation of the Binary Fe-Au Alloy

A summary of the preliminary experiments that have been performed for Fe-Au alloys in presented in table 3.4[1], correspond to the ones presented in table 3.3. Effectively, the Fe-Au samples were annealed at two different temperatures and aged at three different times. The annealing step is not expected to affect the surface precipitation because for both of them the alloy is completely homogenized and the cooling rates were the same.

Table 3.4: Summary of the preliminary experiments for Fe-Au alloy.

Number	Annealing	Ageing	Set-up
1	900°C-24 hours	700°C-0.5 hour	Set-up 1.a
2	900°C-24 hours	700°C-10 hour	Set-up 1.a
3	868°C-8 hours	700°C-0.5 hour	Set-up 2
4	868°C-8 hours	700°C-8 hour	Set-up 1.b

3.3.1.1. Quantitative Results of the Fe-Au Surface Precipitation

Energy-dispersive spectroscopy (EDS) spot analysis was performed to observe the composition of the precipitates. The results can be observed in figure 3.4 for the different ageing times. These preliminary test were all oxidized and oxygen was always present in the analysis in the range of 3 to 14 wt.% and 10 to 53 at.%. Figure 3.4a is an example of the oxidation in the samples, where it can be observed that the oxidation is present even on the Au-rich precipitates. EDS spatial resolution is too low to obtain exact measurements for such small precipitates, which can be the reason for the presence of oxygen on the Au-rich particles. In section 3.3.4, the oxidation of the samples will be discussed in depth. Taking the oxidation problem into account, various measurements were done ignoring the presence of oxygen in order to observe of the gold and iron ratio of the precipitates. Figure 3.4b show that the composition of the gold precipitates has around 55 $at.\%$ Au, which coincides with the binary iron-gold phase diagram [42, 43] where at 700 ºC the Au-rich precipitates should have a composition close to ~ 80 wt.% and ~ 60 at.% Au and ~ 40 at.% Fe.

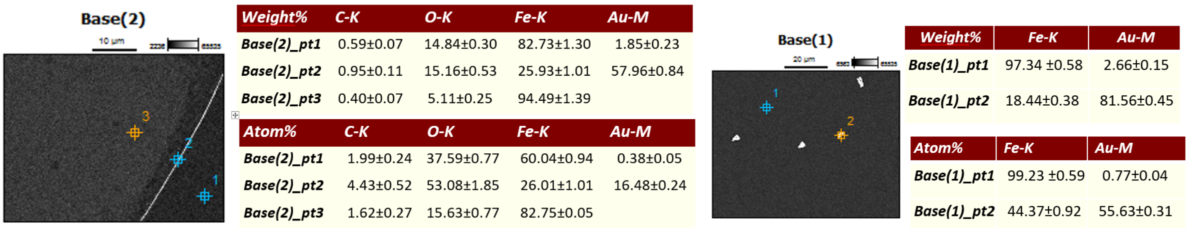

Weight%	C-K	O-K	Fe-K	Au-M
Base(2)_pt1	0.59±0.07	14.84±0.30	82.73±1.30	1.85±0.23
Base(2)_pt2	0.95±0.11	15.16±0.53	25.93±1.01	57.96±0.84
Base(2)_pt3	0.40±0.07	5.11±0.25	94.49±1.39	

Atom%	C-K	O-K	Fe-K	Au-M
Base(2)_pt1	1.99±0.24	37.59±0.77	60.04±0.94	0.38±0.05
Base(2)_pt2	4.43±0.52	53.08±1.85	26.01±1.01	16.48±0.24
Base(2)_pt3	1.62±0.27	15.63±0.77	82.75±0.05	

(a) EDS analysis Fe-3Au. Ageing: 700°C-0.5h.

Weight%	Fe-K	Au-M
Base(1)_pt1	97.34 ±0.58	2.66±0.15
Base(1)_pt2	18.44±0.38	81.56±0.45

Atom%	Fe-K	Au-M
Base(1)_pt1	99.23 ±0.59	0.77±0.04
Base(1)_pt2	44.37±0.92	55.63±0.31

(b) EDS analysis Fe-3Au. Ageing: 700°C-0.5h.

Figure 3.4: EDS analysis on the preliminary experiments for the Fe-Au alloy.

---

[1] Experiment number 2 was performed by H. Fang withing the research group and this thesis has continued the line of his experiments. For this reason, those results have been taken into account.

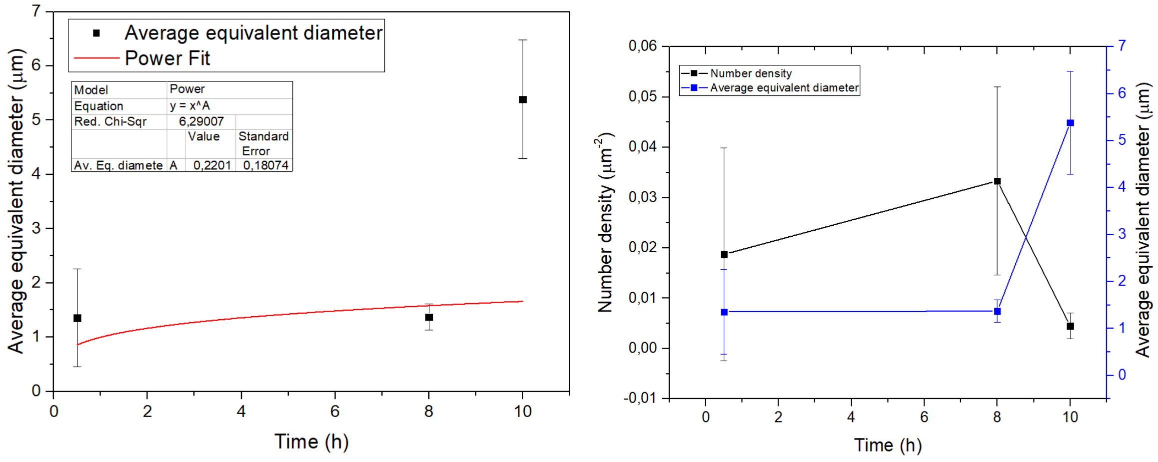

(a) Average diameter.

(b) Number density and average equivalent diameter.

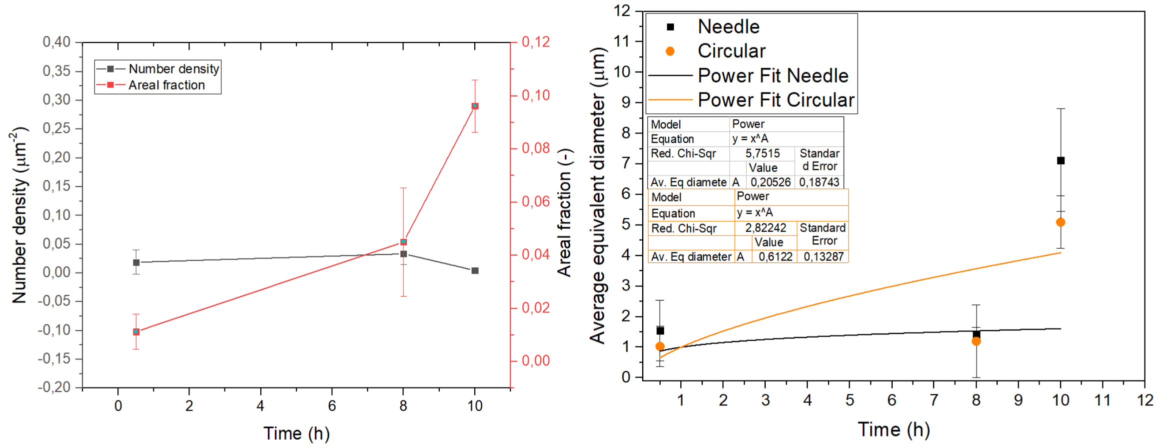

(c) Number density and areal fraction.

(d) Average diameter according to aspect ratio.

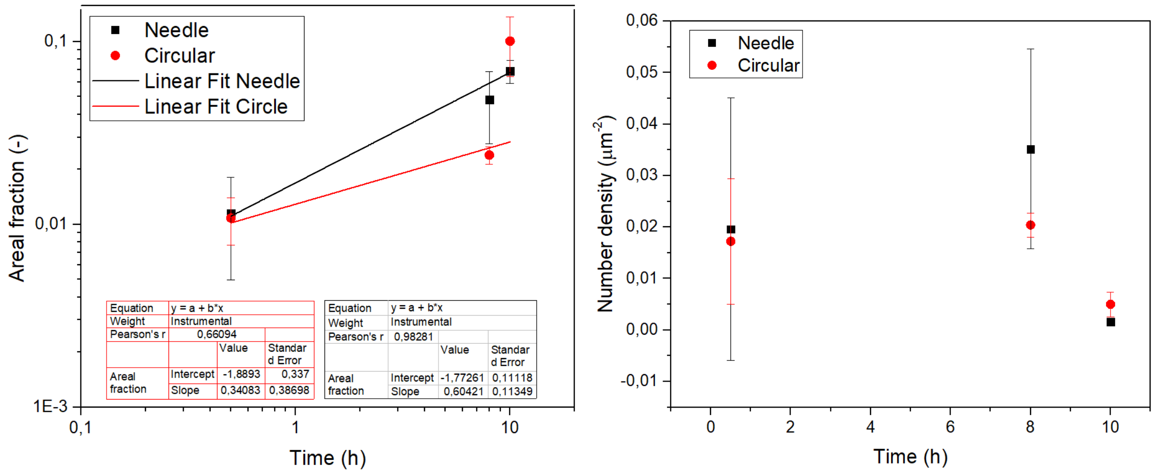

(e) Number density and areal fraction.

(f) Average diameter according to aspect ratio.

Figure 3.5: SEM backscattered images of Fe-3Au after 868°C-8 hours annealing and 700°C-0.5 hours ageing.

Figure 3.5 presents the quantitative analysis of the SEM images. Three parameters have been calculated from the analysis of ImageJ: the equivalent diameter, the areal fraction coverage and the number density.

ImageJ is a software that is able of quantifying the number of particles found by contrast and their areal coverage, which have been used to define the three parameters:

- Average equivalent diameter = $\sqrt{\frac{4\text{Area precipitate}}{\pi}}$
- Areal fraction = $\frac{\text{Area precipitate}}{\text{Area total}}$
- Number density = $\frac{\text{Number of precipitates}}{\text{Area total}}$

The equivalent diameter of the precipitates was calculated assuming that the the particles have an ideal round shape. This way, it is easy to compare the growth of all the precipitates with different shapes. Figure 3.5a presents the evolution with time of the average of the equivalent diameter in all of the grains. A power fit has been performed and it can be observed a exponent of 0.22 ± 0.18 was found. This exponent is in the line of the results from Fang [15] and Carlow [30]. Fang [15] found that for isolated cavities, the precipitate growth had an exponent of 0.267. Carlow's theory [30] proposed for the growth rate based on Ostwald ripening. Carlow et al. proposed $r^n(t) - r^n(0) = Kt$, where the n factor depends on the dimensionality of the problem and limitation of the growth rate. They concluded that the case of surface precipitation is a 3D problem and the rate is limited by surface diffusion, resulting in $n = 4$. Therefore, it can be concluded that the preliminary results are close but slower to the results from Fang and the ones predicted by Carlow's theory.

Figure 3.5b shows the evolution of time of the number density and areal fraction. It can be seen that after 8 hours there is some coarsening because the number density decreases and the areal coverage increases. This is corroborated also by figure 3.5c, where the the average diameter also increases for 10 hours. All of these results should just be taken as a rough indication, because the samples were oxidized, and therefore, the kinetics have been modified [41]. Therefore, no clear conclusions can be obtained.

As observed in the qualitative results in section 3.3.1.2 the shape of the precipitates varies from grain to grain. Generally, the are two main shapes that can be found: round-disk-like and needle-like precipitates. Qualitatively it seems that there can be differences in the behaviour of the precipitates according to their shape. For this reason, the same analysis was performed diving the shapes in two groups by their aspect ratio. The precipitates were fit in a fitted ellipse, and the aspect ratio was calculating by dividing the minor axis by the major one. The two shapes that have been defined are:

- Disk-like/round: the aspect ratio $\frac{c}{a} > 0.5$
- Needle-like: the aspect ratio $\frac{c}{a} \leq 0.5$

Figures 3.5e, 3.5f and 3.5 show the differences in average diameter, areal fraction and number density between these two shapes, respectively. It seems that the results for the needle-like precipitates are more scattered. Round precipitates however, have seem to grow more homogeneously. Both types of precipitates follow the same trend, where the kinetics of the round precipitates seem to be slower. However, maybe this is due to the fact that needle-like precipitates grow along a high-diffusion path in contrast to the round particles. As aforementioned, no clear conclusions are obtained from the kinetic results of oxidized experiments, but these results provide qualitative input for the final experiments.

3.3.1.2. Qualitative Results for the Fe-Au Surface Precipitation

Figure 3.6 presents the evolution of Au-rich surface precipitation in the Fe-Au alloy with different annealing temperatures and times, and most importantly, at different ageing times. It can be see that all of them have some features in common:

- The shape, the size and the number density of the precipitates differ from grain to grain. This means that the influence of the grain crystallographic orientation is a key parameter for the nucleation and growth of the precipitates.
- There is a strong preference for grain-boundary precipitation. Grain boundaries are partially (or fully) covered with precipitates. Even when there are no precipitates inside the grain, the grain boundaries are covered with precipitates. It is logical that precipitates find grain boundaries a favorable nucleation location, as they have more space and less strain energy.
- There are grains that show a precipitate free zone (PFZ) between the grain boundary and the precipitation in the middle of the grain. The width of the PFZ vary from grain to grain, although it seems that they are similar for the grains with same shape of precipitates.

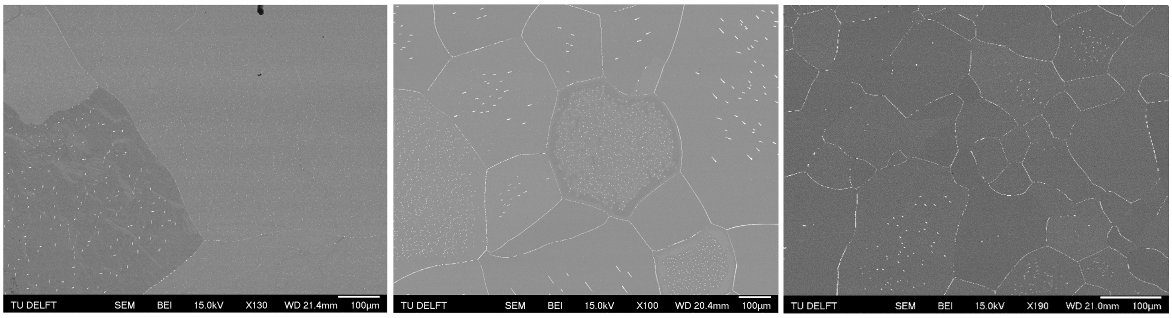

(a) Fe-3Au Set-up 1: 900°C-24h+700°C-0.5h.

(b) Fe-3Au Set-up 1: 900°C-24h+700°C-0.5h.

(c) Fe-3Au Set-up 2: 868°C-8h+700°C-0.5h.

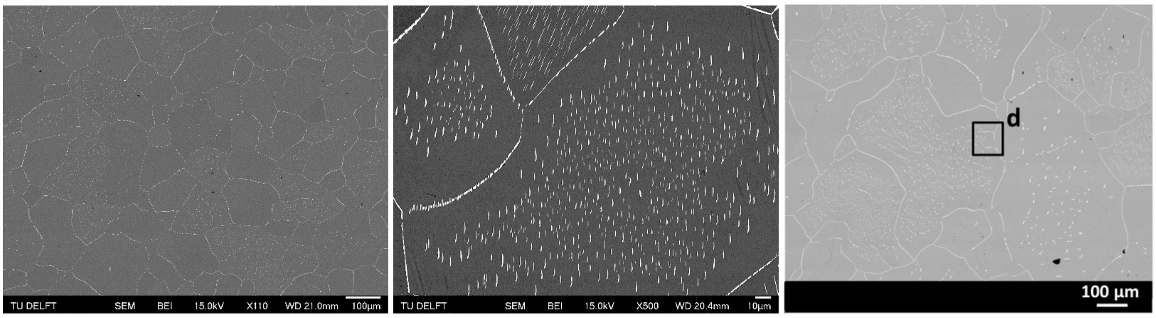

(d) Fe-3Au Set-up 3: 868°C-8h+700°C-0.5h.

(e) Fe-3Au Set-up 5: 868°C-8h+700°C-8h.

(f) Fe-3Au Fang: 900°C-24h+700°C-10h.

Figure 3.6: SEM backscattered electron images of preliminary experiments of Fe-3Au. Comparison of the different annealing and ageing times.Figure 3.6f shows a picture obtained from Fang's results were the square identified by a *d* is not present in this report.

As can be observed in the SEM images in 3.7, Fe-Au alloys seem to present two types of precipitates regarding to their shape: round and needle-like precipitates. These two shapes seem to behave different from each other and have been studied at higher magnification.

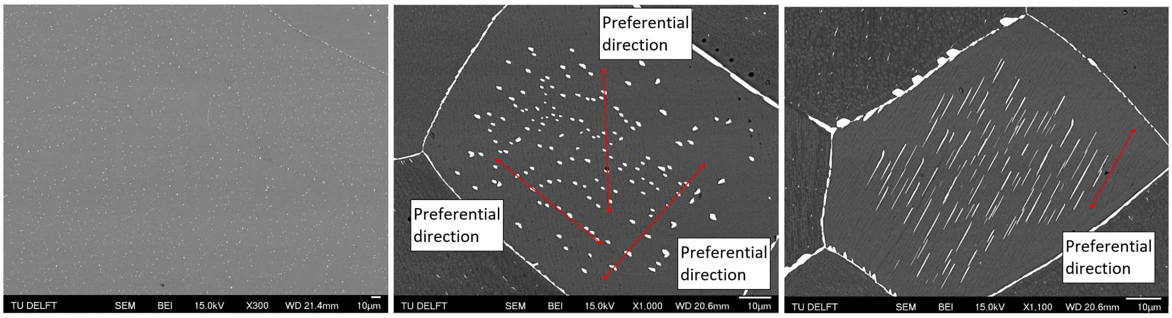

(a) Uniform distribution of round precipitates on Fe-3Au. Ageing: 700°C-0.5h.

(b) Round precipitates in a pattern on Fe-3Au. Ageing: 700°C-8h.

(c) Needle-like precipitates on Fe-3Au. Ageing: 700°C-0.5h.

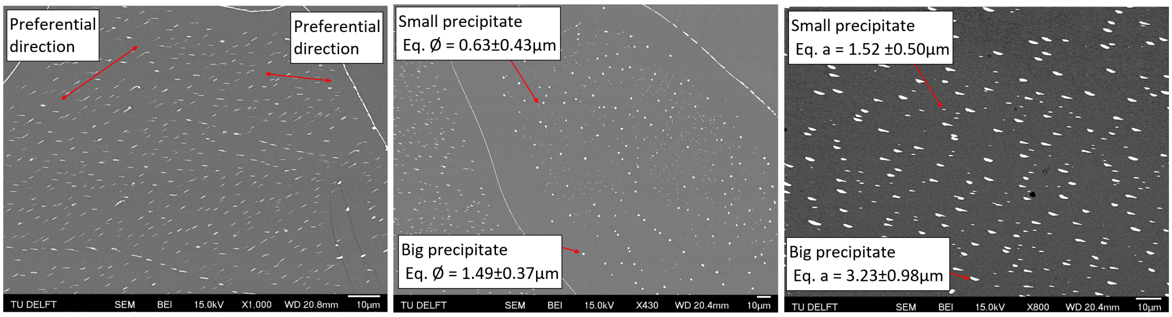

(d) Needle-like precipitates with two preferential growing directions.Ageing: 700°C-0.5h.

(e) Two nucleation times on Fe-Au. Ageing: 700°C-0.5h.

(f) Two nucleation times on Fe-Au. Ageing: 700°C-8h.

Figure 3.7: SEM backscattered electron images of preliminary experiments of Fe-3Au. Comparison of the precipitates shapes, grain boundaries thickness, subgrains and preferential directions.

Round particles are found to precipitate uniformly with high number density, as can be observed in figure 3.7a, or with a low number density but where the precipitation seem to follow a clear pattern, as showed in figure 3.7b. In this last figure, the pattern is called preferential precipitation direction and three different preferential directions have been observed. In the case of the needle-like precipitates, it has always been observed that they follow a preferential direction, which is parallel to their longitudinal direction. Generally, within one grain all needles follow the same direction as presented in figure 3.7c. In very few cases, the precipitates follow two precipitation directions within the same grain, as shown in figure 3.7d. In these cases, the angle between both directions is $\sim 42 \pm 8^\circ$, the major axis is still parallel to the precipitation direction and generally both directions are equally populated. From this observations it can be concluded that the shapes of the precipitates seem to be related to the crystallographic grain orientation.

Furthermore, it has been observed for both precipitate shapes that in some cases there are two sizes of precipitates within the same grain. As shown in figures 3.7e and 3.7f, it is clear that two precipitate sizes are present on top of the grains. It seems that there have been two nucleation stages.

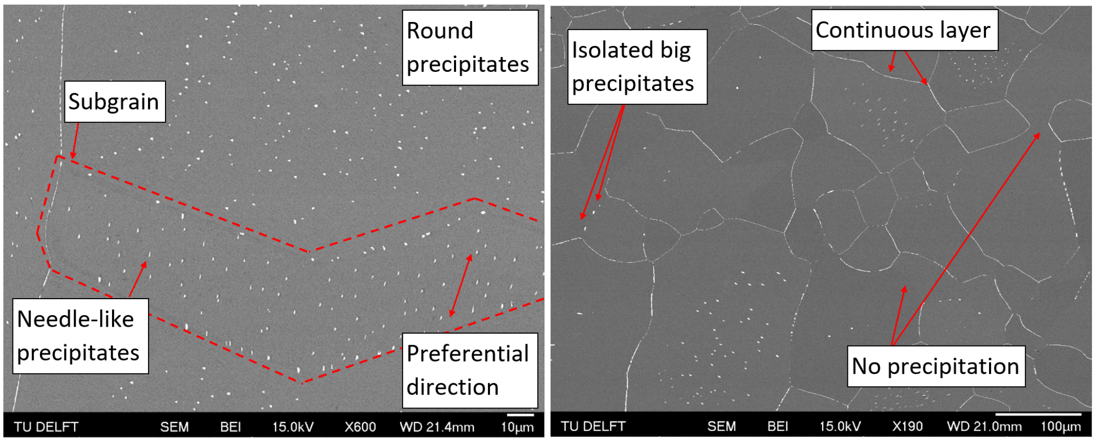

(a) Precipitation on subgrain of Fe-3Au. Ageing:700°C-0.5h.

(b) Precipitation on grain boundaries. Ageing:700°C-0.5h.

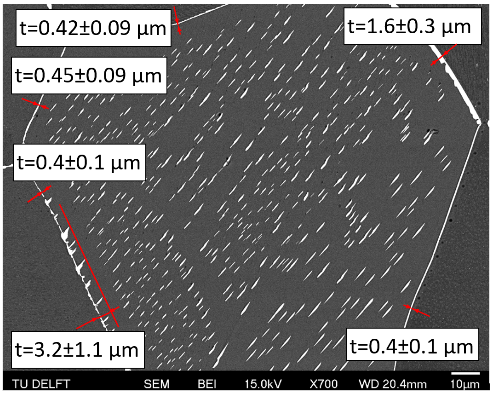

(c) Precipitation on grain boundaries. Ageing:700°C-8h.

Figure 3.8: SEM backscattered electron images of precipitation on subgrain and grain boundaries of the preliminary Fe-3Au experiments. 3.8a shows how the precipitation pattern changes in a subgrain. 3.8c shows the different thicknesses of the grain boundary precipitation within the same grain, where t accounts for the thickness.

Apart from the shape, some other features have been observed repeatedly over the different samples. Occasionally, subgrains have been identified where the precipitation pattern changes subtly. As can be observed in figure 3.8a, the precipitation changes from a uniform round precipitates withing the grain to a needle-like precipitates with a preferential growing direction. From this observations it can be concluded that the the light change in the precipitation pattern in the subgrains is due to the difference in the crystallographic orientation. However, this slight mis-orientation is not enough to create a grain boundary with sufficient energy to attract the precipitation of gold. For this reason, subgrains generally are not surrounded by precipitation on the subgrain boundaries.

Grain boundaries have been found to collect gold precipitates, as it is a preferred nucleation site due to their higher interface energy and lower strain energy required to nucleate. As can be observed in figures 3.8b and 3.8c, this precipitation is very irregular and different precipitate morphologies and thicknesses can be found. This irregular behaviour can be explained by the grain orientation at the grain boundaries. In general, four types of grain boundaries can be seen:

- A continuous layer of gold precipitate, which can vary in thickness depending on the boundary (see figures 3.8b and 3.8c).
- Isolated big irregular precipitates on the grain boundaries, this can happen in all kind of grains: with no precipitates, round or needle precipitates (see figure 3.8b).
- Precipitates that seem to grow in the same pattern as the precipitates inside the grain. In these cases, which mostly appear on the grains with needle-like precipitates, the precipitates only grows towards the preferred grain orientation with a uniform pattern for the precipitation (see figure 3.8c).
- No precipitation.

3.3.2. Surface Precipitation of the Ternary Fe-Au-W Alloy

A summary of the preliminary experiments that have been performed for Fe-Au-W alloys in presented in table 3.5. The same heat treatments as for the binary have been done for the ternary alloy in order to be able to assess the influence of the addition of tungsten. The Fe-Au-W samples were annealed at two different temperatures and aged at two different times. The annealing step has considered to not influence surface precipitation because the alloy is completely homogenized and the cooling rates were the same for both of them.

Table 3.5: Summary of the preliminary experiments for Fe-Au-W alloy.

Number	**Annealing**	**Ageing**	**Set-up**
1	900°C-24 hours	700°C-0.5 hour	Set-up 1.a
2	868°C-8 hours	700°C-0.5 hour	Set-up 2
3	868°C-8 hours	700°C-8 hour	Set-up 1.b

3.3.2.1. Quantitative Results of the Fe-Au-W Surface Precipitation

Energy-dispersive spectroscopy (EDS) spot analysis was performed to observe the composition of the precipitates. The results can be observed in figure 3.9. As aforementioned, the preliminary experiments were oxidized and for this reason oxygen can be found. Figure 3.10a shows that the matrix surface is oxidized, containing 9.4 wt.% (27.5 at.%). However, the precipitate do not show any oxygen content, which is expected as it is Au-rich and gold does not get oxidized [39].

In all of the analyzed data, the oxygen content varied between 3 – 11 wt.% (15 – 31 at.%). Moreover, no W-rich precipitates were found, however, figure 3.9b presents a line scan of a particle and it shows that the Au-rich precipitate is followed by a slight increase in the tungsten content. This behaviour has been observed in various precipitates. From this results it can be concluded that 8 hours are not enough to obtain tungsten Laves phase, having in mind that it could be possible that the oxidation problem has already proved to slow down surface kinetics. Moreover, the content in gold found in almost all of the precipitates, both at 0.5 and 8 hours are around ~ 80 wt.% (~ 55 at.%), which is the same content as the calculated and obtained in the binary alloy. This is a useful parameter as the ternary diagram for Fe-Au-W does not exist. Therefore, the presence of tungsten does not seem to modify the equilibrium percentage of the gold particles. Again, it must be bear in mind that the EDS spatial resolution is too low to obtain exact measurements for such small precipitates. Finally, as expected, the oxidation starts on the exposed matrix and gold precipitates do not get oxidized.

In figure 3.10, the quantitative analysis of the evolution of precipitation with time is presented. There has been only two different ageing times in figures 3.10a-3.10c. The results have been compared to the binary ones. Both alloys have similar results for all of the parameters: average equivalent diameter, areal fraction and number density. This was expected since both of them have only Au-rich precipitates. Even though it seems that the precipitates grow faster in the ternary alloy, the nucleation rate is slower and the ternary results have larger scatter than the binary results. For this reason, no clear conclusion regarding the precipitation kinetics can be made from the ternary alloy.

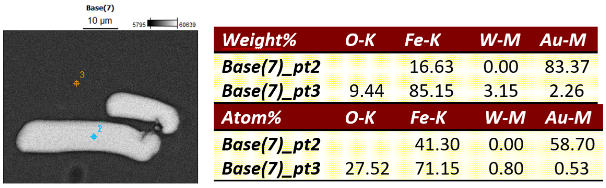

Weight%	O-K	Fe-K	W-M	Au-M
Base(7)_pt2		16.63	0.00	83.37
Base(7)_pt3	9.44	85.15	3.15	2.26
Atom%	**O-K**	**Fe-K**	**W-M**	**Au-M**
Base(7)_pt2		41.30	0.00	58.70
Base(7)_pt3	27.52	71.15	0.80	0.53

(a) EDS analysis Fe-Au-W. Ageing: 700°C-0.5h.

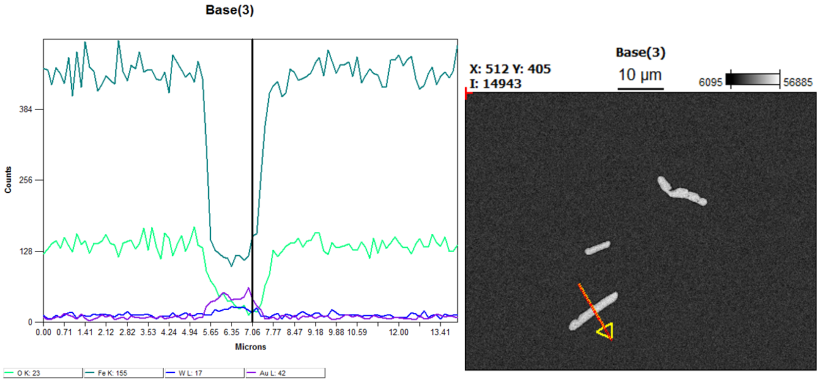

(b) Line scan EDS analysis Fe-Au-W. Ageing: 700°C-0.5h.

Figure 3.9: EDS analysis on the preliminary experiments of Fe-Au-W. In figure 3.9b the line scan is presented. The dark green represents the counts for iron, the light green for oxygen, the purple for gold and the blue for tungsten.

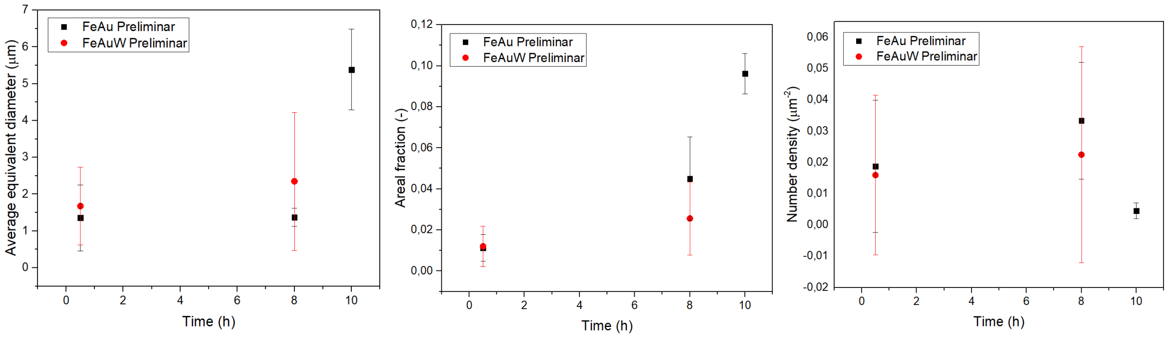

(a) Average diameter.

(b) Areal fraction.

(c) Number density.

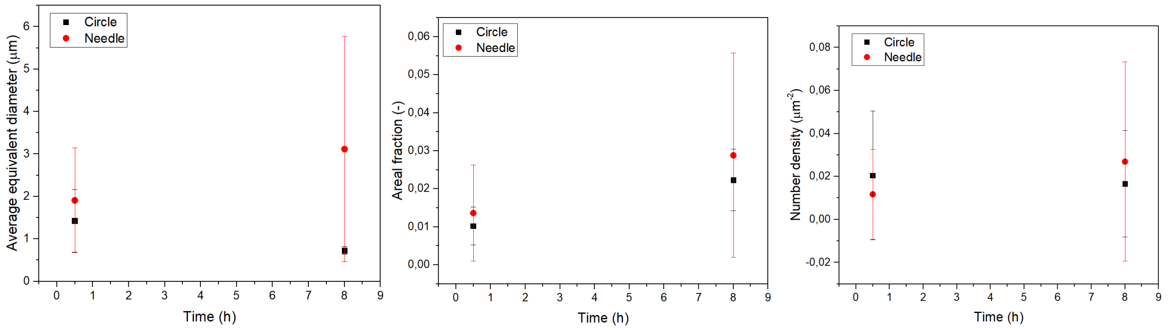

(d) Average diameter according to aspect ratio.

(e) Areal fraction according to aspect ratio.

(f) Number density according to aspect ratio.

Figure 3.10: Quantitative analysis of the evolution with time of the precipitation on Fe-Au-W surface during the preliminary experiments. In view of the few data points that could be obtained from Fe-Au-W, the results have been compared to the Fe-Au preliminary results in figures a-c. Figures d-f show the difference in the aspect ratio.

The ternary alloy behaved as the binary alloy, where the same features were observed: two types of precipitates, round and needle-shaped. Figures 3.10d- 3.10f show a comparison of their evolution with time. Just like in the binary alloy, needle-shaped precipitates show a larger scatter and their growth is faster. However, the nucleation rate seem to be slower. From this result the same conclusion for the binary case can be reached: the growth of the needle-like precipitates could be faster due to the high-diffusivity pathways.

3.3.2.2. Qualitative Results of the Fe-Au-W Surface Precipitation

Figure 3.11 presents the evolution of Fe-Au-W surface precipitation at different annealing temperatures and at different ageing times. The precipitation on the grain boundary increases for larger times and it is clear that there has been coarsening at 8 hours.

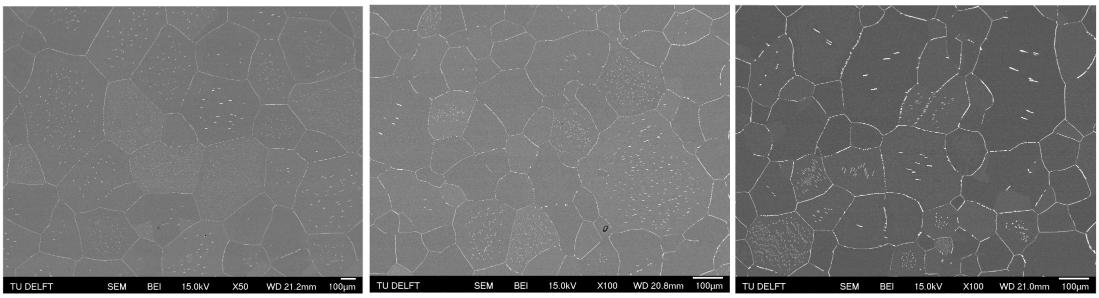

(a) Set-up 1.a - 900°C-24h+700°C-0.5h. (b) Set-up 2: 868°C-8h+700°C-0.5h. (c) Set-up 1.b: 868°C-8h+700°C-8h.

Figure 3.11: SEM backscattered electron images of preliminary experiments of Fe-3Au-4W. Comparison of the different annealing and ageing times.

The qualitative features are in the line as the observations in the binary alloy, as only Au-rich precipitates have been found:

- The shape, the size and the number density of the precipitates differ from grain to grain.
- There is a strong preference for grain boundary precipitation.
- Variable precipitate free zones in the vast majority number of grains.

Round precipitates were found with a uniform distribution or nucleated along preferential directions (see figures 3.12a and 3.12b, respectively). Needle-like precipitates were found all oriented in one direction or two at $\sim 42 \pm 4°$, and occasionally at 90°, which seem to be T-shaped precipitates (see figures 3.12d, 3.12e and 3.12f, respectively). Furthermore, double nucleation times was also observed where the small precipitates were half the size of the big ones, just like in the binary case, where it was also around 40%, see figure 3.12c. Also a change in the precipitation pattern in sub-grains and precipitate free zones (PFZ) were observed. It is clear that the crystal orientation has an influence on the surface precipitation and the relative orientation of the neighbouring grains at the grain boundaries, due to the variation of the PFZ within the grain.

3.3.3. Bulk Precipitation

The cross section of the three samples has been analysed in order to prove that the samples are suitable for self-healing. As aforementioned, one of the requirements for self-healing alloys is that the precipitation in the bulk of the material has to be impeded, and it should only occur selectively on the surface. Previously, the figures have shown that there is precipitation on the surface, for both Fe-Au and Fe-Au-W alloys. It can be observed in figures 3.13 that after 0.5 hours ageing, no precipitation is found in the bulk for Fe-Au and Fe-Au-W alloys, respectively. However, the results after 8 hours at 700°C are very different, as many precipitates have been found next to the surface, as can be observed in the Fe-Au alloy in figure 3.14.

In the case of Fe-Au and Fe-Au-W alloys for 0.5 hours, figure 3.13a shows that there is precipitation on internal cracks, which is the purpose of the self-healing mechanism. In figures 3.13b for Fe-Au and 3.13d and 3.13e for Fe-Au-W , a strong preference for precipitation at the grain boundary is observed. A difference between both of them is that the ternary alloy shows less precipitation at the grain boundaries, see figure 3.13f. In figure 3.13c no segregation or precipitation is promoted close to the surface, which was confirmed by EDS analysis. The EDS results do not show any difference in the atom concentration of gold in the matrix. Consequently, the annealing step of 868°C for 8 hour was successful, after which all the gold and tungsten are in supersaturated solution and it has only precipitated where expected: only on the surface and almost none on the grain boundaries in the bulk material. Compared to the Fe-Au alloy in the same conditions, W seems to have impeded the precipitation of Au in the grain boundaries, or at least, retarded it.

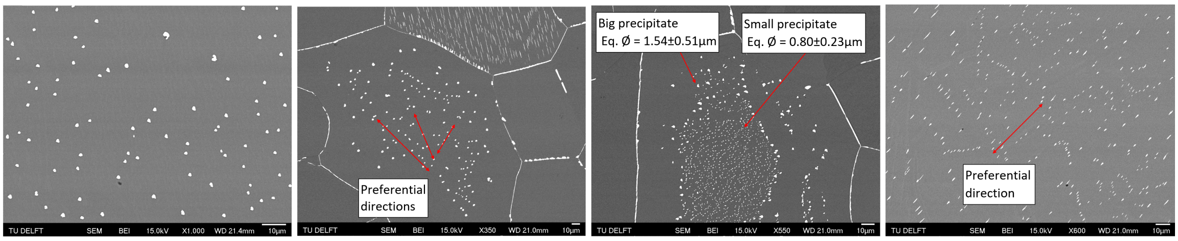

(a) Uniform distribution of round precipitates on Fe-3Au.

(b) Round precipitates in a pattern on Fe-3Au.

(c) Double nucleation found with round shaped precipitates.

(d) Needle-like precipitates with one preferential growing directions.

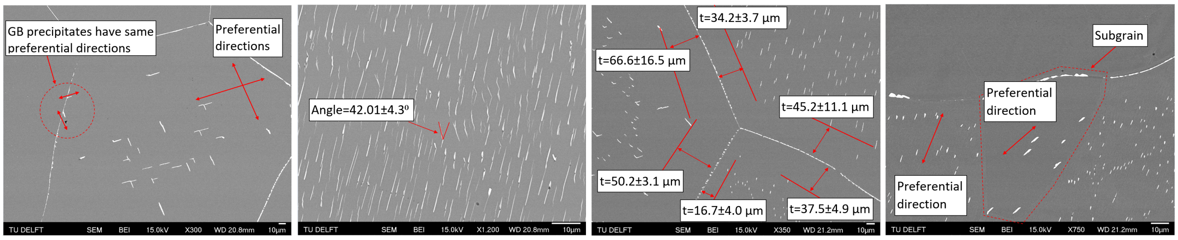

(e) Two orthogonal preferential directions of needles.

(f) Common angle between preferential direction of the needles.

(g) Variation of the precipitate free zones (PFZ) within same grain.

(h) Precipitation on a subgrain: change in pattern.

Figure 3.12: SEM backscattered electron images of preliminary experiments of Fe-Au-W. Comparison of the precipitates shapes and preferential directions.

The diffusional length of gold at 700°C for 0.5 hours is $x_{diff,Au}(700^\circ C, 0.5h) \sim 1.2\mu m$, therefore, it would have been expected that the first $\sim 1.2\mu m$ would have been depleted of gold due to the surface precipitation. This means that the self-healing mechanism can last longer since the matrix keeps supersaturated. From this results, it can be concluded that the annealing step was successful, where all the gold is in supersaturated solution and only it has precipitated where expected: only on the surface and minimally on the grain boundaries of the bulk material.

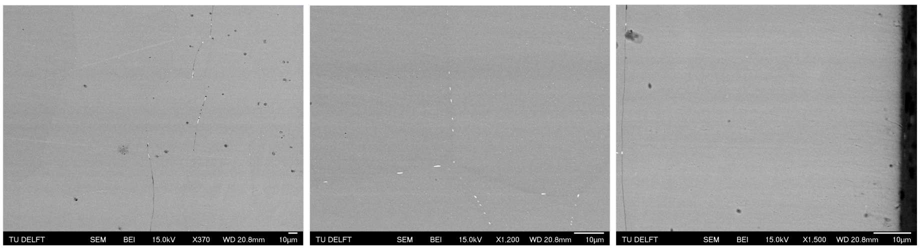

(a) Precipitation on internal cracks.

(b) Precipitation on grain boundaries.

(c) Precipitation next to the surface.

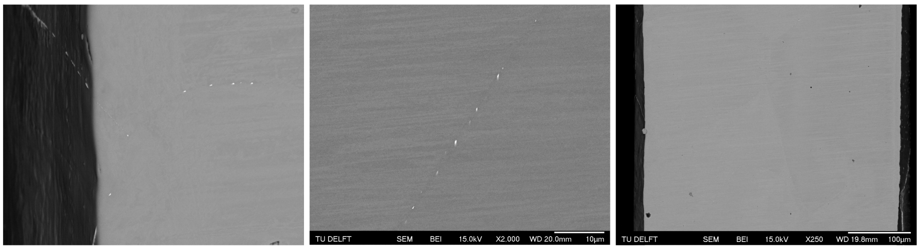

(d) Precipitation on internal cracks.

(e) Precipitation next to the surface.

(f) Precipitation on grain boundaries.

Figure 3.13: Cross-section of Fe-Au and Fe-Au-W for an ageing time of 0.5 hours.

The results for Fe-Au alloy for an ageing time of 8 hours showed precipitation in the bulk close to the lateral and polished surface, as can be seen in figure 3.14a. Even the lateral surface, which corresponds to the top one in figure 3.14a, has big gold-rich precipitates and segregation of the order of $\sim 10\mu m$. It can be observed that, depending on the grain, the precipitates are ordered in a pattern or direction. Again, it is confirmed that the precipitation highly depends on the crystallographic orientation. However, the non-polished surface, in contact with the sample holder during the heat treatment, had no precipitates (see figure 3.14c). This precipitation band along the edge was not expected as it means that the matrix close to the surface can get depleted of the healing solute.

Figure 3.14b shows a higher magnification of bulk precipitation near the polished edge. All the bulk precipitates are gathered in a band of $60 \pm 2 \mu m$. In this band, only present along the polished edge and the lateral edge of the samples, there are zones free of precipitates with a width of $1.20 \pm 0.04 \mu m$, which coincides with the diffusion length for gold at 700°C for 0.5 hours ($\sim 1.2 \mu m$) and not with 0.8 hours ($\sim 5 \mu m$). This diffusion length has been calculated as $X_{diff,Au} = 2\sqrt{D_{Au} t}$, where D_{Au} at 700° has been obtained from Versteylen calculations. An EDS analysis has been performed in order to clarify this precipitation and it is presented in figure 3.14d. The line scan shows that in the first $\sim 5 \mu m$ perpendicular to the surface there is a depletion of gold in the matrix. This coincides with the hypothesis, since it would mean that gold has diffused to the surface and formed precipitates. Then the concentration of gold overpasses the at.% defined for the supersaturated matrix ($1 at.\%$) for the width of the precipitation band. Then the concentration of gold returns to the nominal value ($1.2 at.\%$).

If the results from Fe-Au aged at 0.5 and 8 hours, are compared, it can be seen that the precipitation on the grain boundary occurs already at around 0.5 hours, since the zone free of precipitates has the same width as the diffusion length of gold for 0.5 hours. The precipitation in the bulk seems to occur only at longer ageing times.

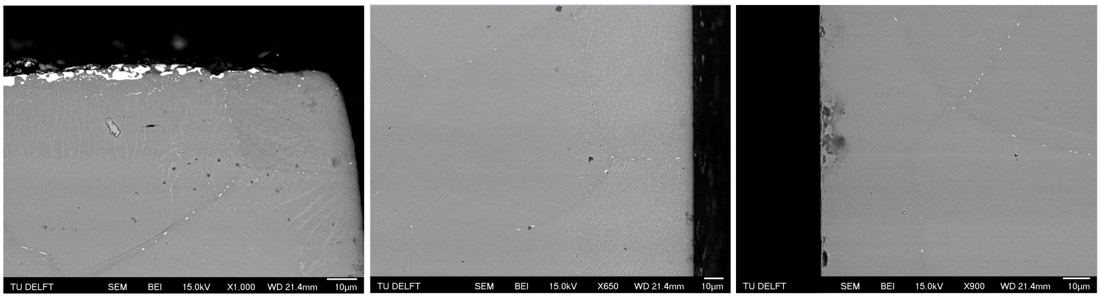

(a) Precipitation on the corner. (b) Precipitation next to the surface. (c) Precipitation on the opposite surface.

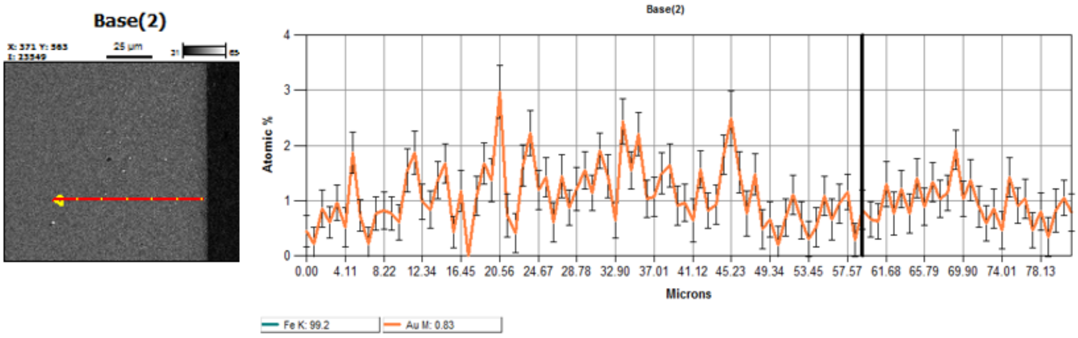

(d) EDS Line-Scan of the composition (at%) next to the surface.

Figure 3.14: Cross section of the Fe-Au alloy that has been heat treated with set-up 5: 868°C for 8 hours and 700°C for 8 hour.

3.3.4. Oxidation

Set-ups 1-2 resulted in oxidized samples, for both alloys. This section will comment the observations on the oxide layer.

Figure 3.15 shows the EDS analysis performed, where the oxide layer had a composition of $\sim 43 at.\%$. Iron oxide (III) (Fe_2O_3) would correspond to a $\sim 60 at.\%$. Taking into account the resolution of EDS measurements where part of the X-rays come from the underlaying matrix, it could be concluded that it corresponds to Fe_2O_3.

The oxide layer is porous as can be observed in figure 3.16a, and the this oxide layer is observed at the base of many precipitates (see figure 3.16b. The oxidation layer from figure 3.16c has been measured to be $45 \pm 8 nm$. In figure 3.16d it can be seen that the oxidation layer is uniform, but it only covers part of the grains. As can be seen in figure 3.16e, EDS analysis has confirmed that effectively there are non-oxidized regions, which sometimes surround the precipitates. In other cases, the oxide layer is only on top of the precipitates.

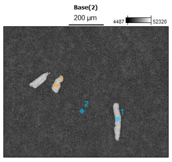

(a) BEI image of oxidized Fe3Au surface.

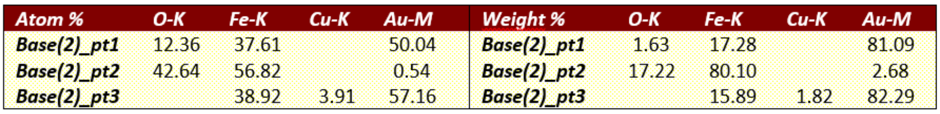

Atom %	O-K	Fe-K	Cu-K	Au-M	Weight %	O-K	Fe-K	Cu-K	Au-M
Base(2)_pt1	12.36	37.61		50.04	**Base(2)_pt1**	1.63	17.28		81.09
Base(2)_pt2	42.64	56.82		0.54	**Base(2)_pt2**	17.22	80.10		2.68
Base(2)_pt3		38.92	3.91	57.16	**Base(2)_pt3**		15.89	1.82	82.29

(b) EDS composition analysis of the oxidized surface.

Figure 3.15: SEM secondary electron images of the surface oxidation of the Fe-Au alloy. The heat treatment corresponds to set-up 1: 900°C-24 hours annealing and 700°C-0.5 hours ageing.

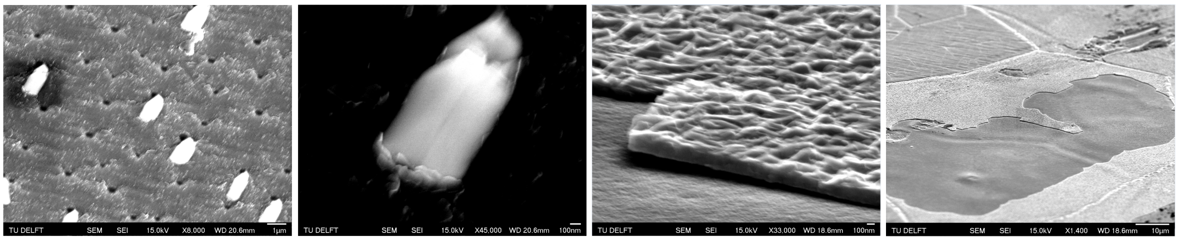

(a) SEI image of the oxide layer on top of precipitates.

(b) SEI image. Particle from 3.16a partially covered with an oxide layer.

(c) SEI image. Oxide layer in Fe-Au-W surface.

(d) SEI image. Non-continuous oxide layer in Fe-Au-W surface.

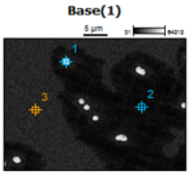

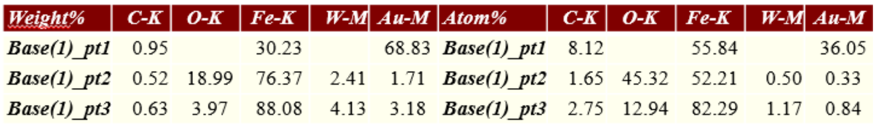

Weight%	C-K	O-K	Fe-K	W-M	Au-M	Atom%	C-K	O-K	Fe-K	W-M	Au-M
Base(1)_pt1	0.95		30.23		68.83	*Base(1)_pt1*	8.12		55.84		36.05
Base(1)_pt2	0.52	18.99	76.37	2.41	1.71	*Base(1)_pt2*	1.65	45.32	52.21	0.50	0.33
Base(1)_pt3	0.63	3.97	88.08	4.13	3.18	*Base(1)_pt3*	2.75	12.94	82.29	1.17	0.84

(e) EDS chemical composition analysis of a particle, the matrix and the oxide layer, respectively.

Figure 3.16: SEM secondary electron images of the surface oxidation of the Fe-Au (a-b) and Fe-Au-W (c-e) alloys. The heat treatment corresponds to set-up 2: 868°C-8 hours annealing and 700°C-8 hours ageing.

According to the findings, two possible situations are possible for the formation of the oxide layer.

- The oxide layer forms prior to the precipitation and it happens during the annealing. The precipitates nucleate and grow at the interface between the matrix and the oxide layer. Figure 3.17a represents this scenario. The oxidation Fe-Au-W alloy seems to agree with this mode if figure 3.16d is observed. This is the most likely mechanism.

  It could also happen that when the particles grow, the particles break the oxidation layer.

- The oxide layer starts growing in the matrix after the surface precipitation has occurred. Then, this oxide layer grows on top of the precipitates. Figure 3.17b represents this scenario. The oxidation in the Fe3Au alloy seems to agree with this mode if figure 3.16a is observed.

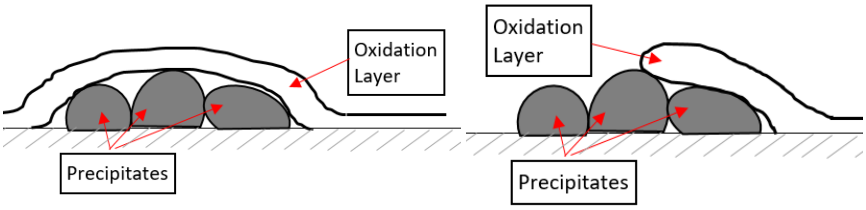

(a) Oxidation mode 1.

(b) Oxidation mode 2.

Figure 3.17: Proposed modes of oxidation.

3.4. Final Results and Discussion

The oxidation problems in the furnace were solved and the final experiments were performed. As aforementioned, two types of set-ups (3 and 4) resulted in no oxidation. The set-up 3 consisted on annealing and ageing the samples in the same furnace. The cool down in the silica furnace was observed to be slower than expected, since the final cool down from 700ºC to room temperature was expected to take 70 minutes (10ºC/min) and it took around 5 hours. No thermocouples were attached to the samples and the analysis of the SEM images indicates that the cool down was slower than expected. This has had an influence on surface precipitation as it will be explained in section 3.4.1.1. On the contrary, set-up 4 performed the pre-annealing in an auxiliary vertical furnace with the sample in a silica tube in high purity Argon atmosphere. The sample was quenched subsequently, then polished, indented and taken to the furnace for the ageing step. To make it clear, a summary of the final experiments that have been performed for the Fe-Au and Fe-Au-W alloys in presented in table 3.6.

This section will first present the results of set-up 3, as this set-up applies the same heat treatment as set-ups 1-2. Secondly, the results for set-up 4 will be analysed and compared with the previous analysis. Moreover, the supplementary analysis that was performed in the set-up 4 samples will be presented. EBSD was performed in order to obtain a relationship between the crystallographic orientation at the sample surface and the precipitation. Additional TEM analysis on Fe-Au-W failed creep samples have been performed in order to find any similarities and indentation experiments have been analysed to observe the relation between the prior plastic strain and the precipitation. Finally, the section ends with the obtained conclusions.

Table 3.6: Summary of the final experiments for Fe-Au and Fe-Au-W alloys.

Number	Annealing	Cooling	Ageing	Set-up
1	868°C-8 hours	$>17min$	700°C-2 hour	Set-up 3
2	868°C-8 hours	Quench	700°C-2 hour	Set-up 4
3			700°C-16 hour	
4			700°C-32 hour	

3.4.1. Results of Set-up 3: Comparison Between Fe-Au, Fe-Au-W and Fe-6W Alloys

The first experiment performed on the final furnace consisted on three samples tested with set-up 3: Fe-Au, Fe-Au-W and Fe-6W. Fe-6W was included in the analysis as it is the most sensitive alloy from the three to oxidation in order to prove the control on the atmosphere of the furnace. Fe-6W has a higher tungsten content, therefore, the Laves phase has a higher driving force to precipitate and shorter times are required. Laves phase is expected to precipitate, which is the phase that requires the lowest oxygen partial pressure to avoid oxidation [39].

3.4.1.1. Quantitative Results for Fe-Au, Fe-Au-W and Fe-6W Alloys with Set-up 3

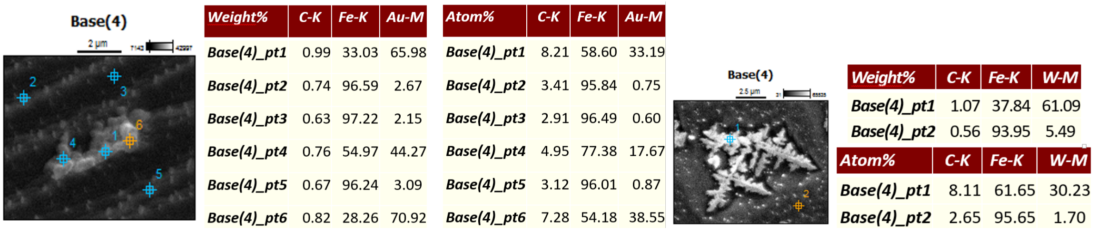

Weight%	C-K	Fe-K	Au-M
Base(4)_pt1	0.99	33.03	65.98
Base(4)_pt2	0.74	96.59	2.67
Base(4)_pt3	0.63	97.22	2.15
Base(4)_pt4	0.76	54.97	44.27
Base(4)_pt5	0.67	96.24	3.09
Base(4)_pt6	0.82	28.26	70.92

Atom%	C-K	Fe-K	Au-M
Base(4)_pt1	8.21	58.60	33.19
Base(4)_pt2	3.41	95.84	0.75
Base(4)_pt3	2.91	96.49	0.60
Base(4)_pt4	4.95	77.38	17.67
Base(4)_pt5	3.12	96.01	0.87
Base(4)_pt6	7.28	54.18	38.55

(a) Fe-Au.

Weight%	C-K	Fe-K	W-M
Base(4)_pt1	1.07	37.84	61.09
Base(4)_pt2	0.56	93.95	5.49

Atom%	C-K	Fe-K	W-M
Base(4)_pt1	8.11	61.65	30.23
Base(4)_pt2	2.65	95.65	1.70

(b) Fe-W.

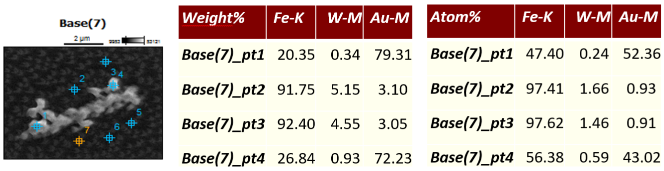

Weight%	Fe-K	W-M	Au-M
Base(7)_pt1	20.35	0.34	79.31
Base(7)_pt2	91.75	5.15	3.10
Base(7)_pt3	92.40	4.55	3.05
Base(7)_pt4	26.84	0.93	72.23

Atom%	Fe-K	W-M	Au-M
Base(7)_pt1	47.40	0.24	52.36
Base(7)_pt2	97.41	1.66	0.93
Base(7)_pt3	97.62	1.46	0.91
Base(7)_pt4	56.38	0.59	43.02

(c) Set-up 4: 700°C-16h.

Figure 3.18: EDS analysis of set-up 3 experiments for the Fe-Au, Fe-Au-W and Fe-6W.

Energy-dispersive spectroscopy (EDS) spot analysis was performed to observe the composition of the precipitates, as can be seen in figure 3.18. Figure 3.18a presents the composition of the Au-rich precipitates in the Fe-Au alloy, where the content was found to be ~ 70 wt.%Au, which is the expected value from the phase diagram, taking into account the resolution of EDS. Figure 3.18b shows the composition of the W-rich precipitates found in the Fe-6W alloy. The content of W was found to be ~ 60 wt.% (~ 30 at.%) which coincides perfectly with the Laves phase composition Fe_2W. Finally, the ternary alloy was also examined but only Au-rich were found, with a composition of ~ 70 wt.%Au, as can be seen in figure 3.18c.

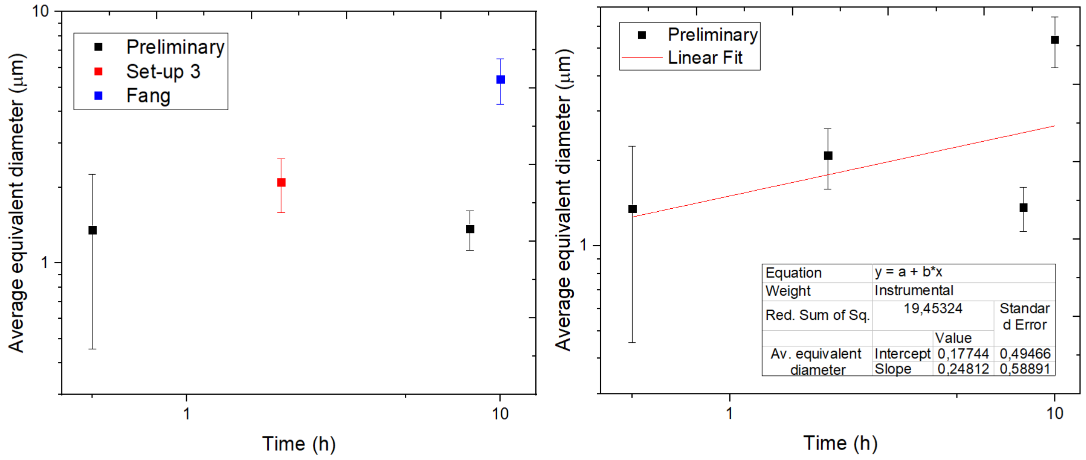

(a) Average equivalent diameter of Fe-Au.

(b) Linear fitting of the average equivalent diameter of Fe-Au.

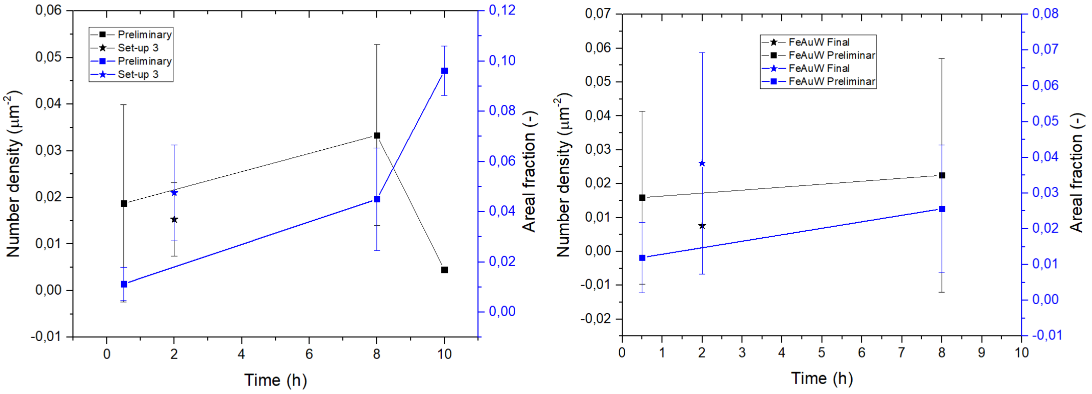

(c) Number density and areal fraction of Fe-Au.

(d) Number density and areal fraction of Fe-Au-W.

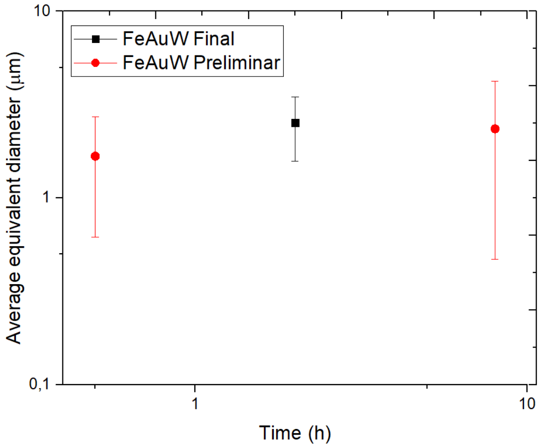

(e) Average equivalent diameter of Fe-Au-W.

Figure 3.19: Analysis of the evolution with time of set-up 3 experiments on the Fe-Au and Fe-Au-W alloys and comparison with preliminary results.

From this results can be concluded that the new furnace successfully managed to keep the oxygen partial pressure below the standards to avoid oxidation where the precipitation occurred as expected since their composition was as predicted by phase diagrams.

The quantitative analysis of the precipitation will be compared to the preliminary results, since the same heat treatment has been applied. This means that it will be possible to observe the influence that the oxidation had in the preliminary results.

Fe-Au and Fe-Au-W results have been analysed quantitatively and compared with the preliminary results, as can be observed in figure 3.19. The average diameter evolution with time for the Fe-Au precipitates was compared in a double logarithmic graph (see 3.19a. Compared to the preliminary results, it seems that the growth in a non-oxidising atmosphere is faster. However, it seems that the preliminary points at 0.5, 10 and the new point fit the same line, which is expected in the double logarithmic scale since the relation between diameter and time is in the form of $r = a * t^b$, and that the preliminary point at 8 hours would be out of place. The eight hours experiment in an oxidizing atmosphere seems to have have been halted or slowed down the growth of the precipitates. Whereas for the 0.5 hours it has not been enough time to influence, and the 10 hours experiment was not oxidized. A linear fitting (see 3.19b) of all the data points including the new one has resulted in a slope of 0.24, which is closer to Carlow's 0.25 theoretical results. The evolution of number density and areal fraction of the Au-rich precipitates in the Fe-Au alloy can be observed in figure 3.19c. It can be observed that both the number density and the areal fraction rate fits in in the trend in the preliminary results. The scatter in the number density is smaller in the final experiment compared to the preliminary.

For the Fe-Au-W alloy, the comparison is harder as there were only two preliminary data points. It must be taken into account that in the final experiments also only Au-rich precipitates were found. In agreement with Fe-Au alloy results, the number density is lower than the preliminary results, and the areal fraction is much higher and the as its scatter (see figure 3.19d). This means that the nucleation is slower, whereas growth is faster in a non-oxidising atmosphere. However, due to the scatter, the results could still follow the same trend as Fe-Au alloy. For this reason, the average equivalent diameter is plotted in figure 3.19e, where it is more clear whether if the oxidation had influenced the results. As aforementioned, a linear fitting is expected in a double logarithmic scale. However, for the ternary there is no previous experimental literature of it can be assumed that the slope is the defined by Carlow again without Au-W interaction to affect the growth. In agreement with the Fe-Au results, the growth for 8 hours was slowed down by the oxidation layer.

From these results, it can be concluded that the oxidation layer had an influence on the surface precipitation for long exposure experiment (8 hours) by slowing down the growth kinetics and it could be possible that for short exposure (0.5 hours) the influence is negligible. For this reason, the short exposure, the final results and the non-oxidized results from Fang can fit according to Carlow's theory and Fangs results for creep conditions.

3.4.1.2. Qualitative Results for Fe-Au, Fe-Au-W and Fe-6W alloys with Set-up 3

A general image of the precipitation of set-up 3 is shown in figure 3.20. In the ternary alloys only Au-rich precipitates were found. For this reason, the precipitation for Fe-Au and Fe-Au-W alloys looks identical, as can be observed in figures 3.20a and 3.20b.

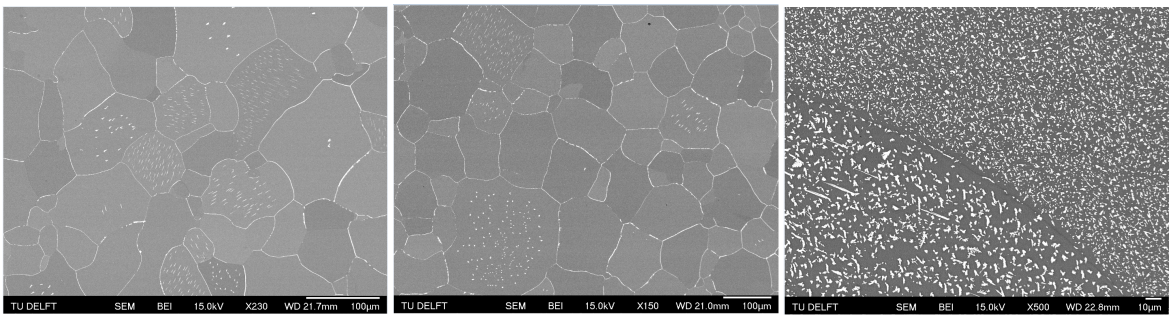

(a) Fe-Au.

(b) Fe-Au-W.

(c) Fe-W.

Figure 3.20: SEM backscattered electron images of set-up 3 experiments on Fe-Au, Fe-Au-W and Fe-6W.

Both figures 3.20a and 3.20b present all of the features found in the preliminary results. The precipitation is inhomogeneous among the grains, since the density and the shape of the precipitates change from grain to grain. Generally, all of the grain boundaries are covered, even if there is no precipitation within the grain. This confirms the strong preference of the precipitation of Au-rich particles for the grain boundary. However, its thickness and shape changes also depending on the nature of the boundary, in the same way as precipitate-free zones. These two last features could depend on the neighbouring grains and their relative crystal orientation. The crystal orientation seems to be a critical parameter that dictates the surface precipitation, as it influences the number density (controls nucleation), the shape (controls the growth) and the grain-boundaries surroundings.

A different precipitation pattern was found on Fe-6W alloy, as shown in figure 3.20c. The matrix is fully covered by precipitates, which in general have irregular shapes, but in most of the cases dendritic traces can be seen. The areal coverage is really high and the distribution seems to be uniform and not follow any pattern. Opposite to Au-rich precipitates, the W-rich precipitates avoid precipitation on the grain boundary, which stands out for a lack of precipitates.

The absence of an oxidation layer has enabled the observation of the topography of the precipitates. Figure 3.21 presents in detail examples of the precipitation on the grain boundary in the Fe-Au alloy, both round and needle-like precipitates in the Fe-Au-W alloy and a dendritic precipitate in the Fe-W alloy in figures 3.21a,3.21b, 3.21c and 3.21d, respectively. The Au-rich precipitates show a globular morphology, as if it is composed of smaller Au-rich clusters. Consequently, the surface/volume ratio is high, which increases the surface energy of the precipitate. This morphology, which is not the equilibrium for Au-rich precipitates, can be explained by the time-scale of the experiment where 2 hours could not be enough for the coalescence of these clusters that would finally end up in a single precipitate with minimal surface/volume ratio.

For the case of the W-rich precipitates, the dendritic morphology is a uncommon morphology for solid-state transformations. Previous literature agrees that this type of morphologies occur in the following situations [44, 45]:

- Isotropic interfacial energy between the precipitate and matrix, This occurs when no crystallographic orientation between the precipitate and the matrix, or there is a total coherency between them. This results in a fast atom attachment to the growing interface.
- Low diffusivity in the precipitate, which happens for really ordered phases.
- A slight misfit between the two phases that results in a slower diffusivity than in a case where there are adjustments dislocations.

Moreover, the direction of the dendrites follow specific directions related to the crystallographic orientations. However, generally this morphology is characteristic of the early growth stages of the precipitates, since a larger size comes with a loss of coherency with the matrix and it ends up transforming in more rounded/polyhedral shaped precipitates. The dendrites found were in the order of $\sim 1\mu m$. Hence, it is expected that for longer times this dendritic morphology is not observed.

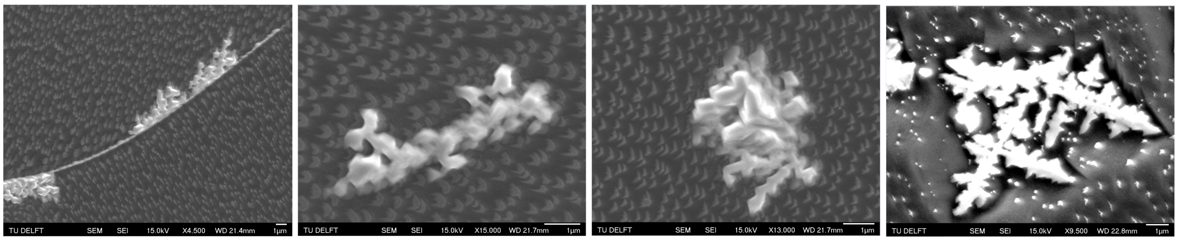

(a) Fe-Au. (b) Fe-Au-W. (c) Fe-Au-W. (d) Fe-W.

Figure 3.21: SEM backscattered electron images of set-up 3 experiments for the Fe-Au, Fe-Au-W and Fe-6W alloys.

3.4.2. Results of Set-up 4: Final Experiments on the Fe-Au and Fe-Au-W Alloys

Finally, in order to reduce the possibility of oxidation, the annealing of the samples was performed in an second furnace and the samples were quenched. Then, they were mechanically polished just before the ageing treatment in the new furnace.

The results for the Fe-Au alloy were as expected, and the precipitation was on the line of the previous results.

However, the results on the Fe-Au-W alloy for 16 and 32 hours showed W-rich precipitates for the first time. Moreover, there was an additional experiment performed on the ternary alloy for 1 hour ageing that has been included in the quantitative analysis.

In this section, the quantitative and qualitative results of the Fe-Au alloy will be presented in the first place, followed by the analysis of the Fe-Au-W alloy. Additionally, supplementary results of EBSD and TEM on the Fe-Au-W alloy will be discussed and finally, the conclusions of this work will be presented.

3.4.2.1. Quantitative Results for the Fe-Au Alloy Surface Precipitation

The results on the composition of the Au-rich phase found for the three ageing times coincide with precious results and the expectations from the phase diagram at 700ºC. Figure 3.22 is an representative example of the EDS analysis in a Au-rich particle, for a 32 hour experiment, in which the precipitate has a ~ 79 wt.% Au.

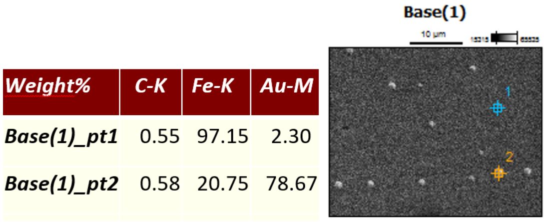

Weight%	C-K	Fe-K	Au-M
Base(1)_pt1	0.55	97.15	2.30
Base(1)_pt2	0.58	20.75	78.67

Figure 3.22: EDS analysis of set-up 4 experiments on the Fe-Au alloy.

The surface precipitation was quantified via the number density, areal fraction and average diameter. As seen in figure 3.23a, the number density decreases with time at the same time as the areal fraction increases. It can be concluded that coalescence of particles could be taking place. In figure 3.23b, the average equivalent diameter is showed together with the areal fraction and their tendencies in a double log-scale.according to previous literature both of them follow a power law with time, which in a double log-scale is represented by a linear function. A linear fitting was performed, where the average particle diameter has a slope of 0.12 ± 0.14 and areal fraction 0.44 ± 0.12. The areal fraction should have a slope two times the average diameters one, since the area $\propto d^2$. These results were compared to the preliminary in figures 3.23c and 3.23e. It can be observed that the set-up 4 kinetics are slower, since the average diameter in the set-up 4 seem to grow at half of the power as in the preliminary, 0.12 and 0.25 respectively. For the areal fraction, a similar situation is observed. However, if the number density is observed (see figure 3.23e), it can be seen that the number density of the final results is much larger, which means that many more precipitates have nucleated. Therefore, the situation is the following:

- Set-up 4 has a ~ 14 times higher number density that set-ups 1-3. In the times observed for set-ups 1-3 a nucleation phase can be seen from 0.5-8 hours and then coalescence from 8-10 hours, whereas in set-up 4 only coarsening is seen from 2-32 hours. Therefore, it seems that the coalescence happens earlier in set-up 4.
- The growth is higher in set-ups 1-3, since areal fraction and the average equivalent diameter are bigger and the trends are also higher.

Figure 3.23f represents this situation in the same figure, and where set-up three fits perfectly with the preliminary results even if they were oxidized. From these observations it can be concluded that the annealing step had an influence on the surface precipitation. In set-ups 1-3 the annealing step was performed in the oven and no quenching was possible. The results suggest that the cooling rate from the annealing to the ageing time was not fast enough to prevent any precipitation reaction in the cooling stage. This would explain the lower number density and larger growth of the particles. The surface precipitation on set-ups 1-3 would have happened as followed:

1. In the annealing step everything is homogenized and no precipitation occurs.
2. During the cooling down, once the equilibrium temperature between the $\alpha - \alpha + Au$ region is reached, then nucleation of Au-rich particles start. At this high temperature the driving force is lower, and therefore, a low number of precipitates nucleate, but their growth is fast due to the higher diffusivity at high temperatures.

3. Once the ageing temperature is reached, the driving force to precipitate is not as high as if the alloy would have maintained the original supersaturated state since already a large areal fraction has precipitated. For this reason, there is not a high increase of nucleation rate.

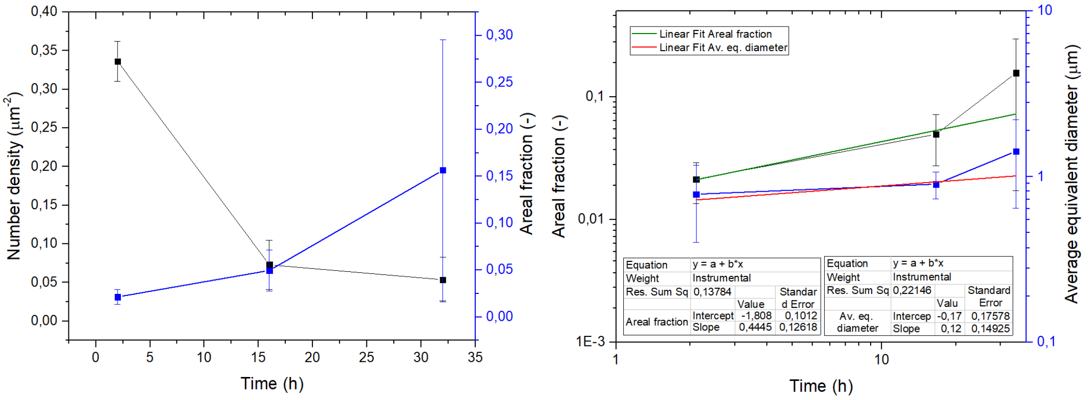

(a) Number density and areal fraction.

(b) Areal fraction and average equivalent diameter.

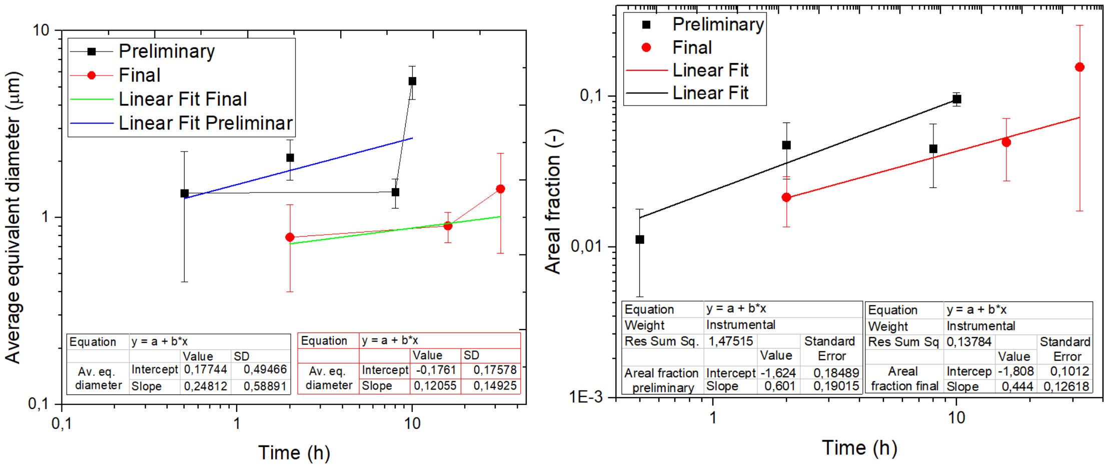

(c) Comparison of final and preliminary results of equivalent diameter.

(d) Comparison of final and preliminary results of areal fraction.

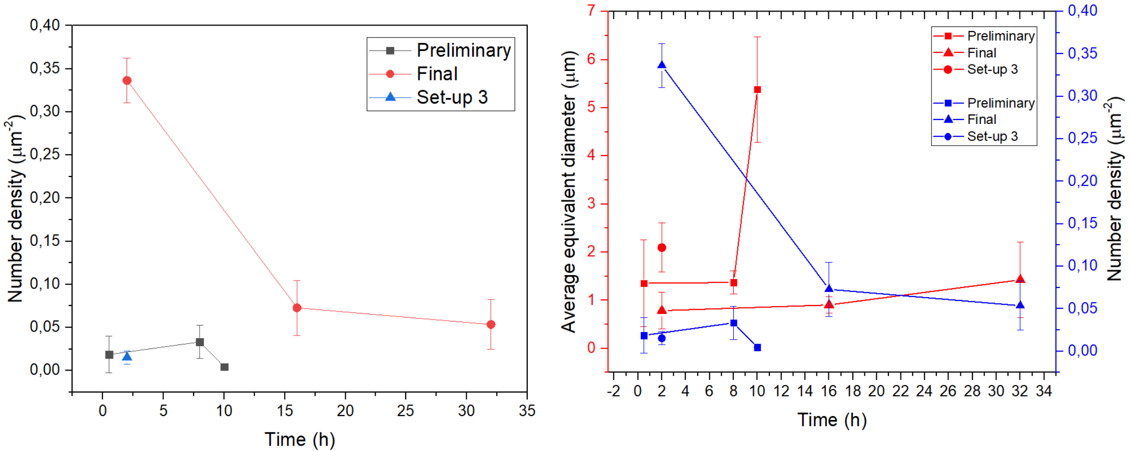

(e) Comparison of final and preliminary results of number density.

(f) Comparison of final and preliminary number density and equivalent diameter.

Figure 3.23: Analysis of the evolution with time of set-up 4 experiments on Fe-Au and comparison with preliminary results. in figures 3.23b, 3.23c and 3.23e a fitting has been done in order to calculate the growth law.

On the other hand, for set-up 4, where the samples have been quenched after the annealing, the samples arrive to the ageing temperature with a higher driving force, which results in higher nucleation sites and higher number density. Since the precipitation occurs at lower temperature, the diffusivity is lower and the growth is slower, resulting in smaller average equivalent diameter.

Furthermore, the precipitate-free zones of all the grain that have been analysed were observed and quantified. In other words, the PFZ of set-ups 3 and 4. Figure 3.24 shows he results in which it can be seen that the precipitate-free zone is independent of the ageing time and the annealing.

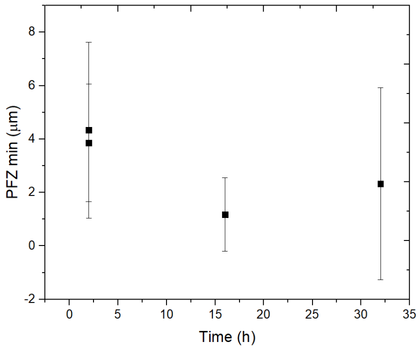

Figure 3.24: Measurements of the precipitates free zone (PFZ) on final experiments (set-up 4) of the Fe-Au alloy.

3.4.2.2. Qualitative Results for the Fe-Au Alloy Surface Precipitation

Figure 3.25 presents an overview of the evolution of the surface precipitation of the final set-up 4 (see figures 3.25b, 3.25c and 3.25d, respectively) as a function of time (2, 16 and 32 hours) for the Fe-Au alloy and it can be compared with the precipitation from set-up 3 of figure 3.25a.

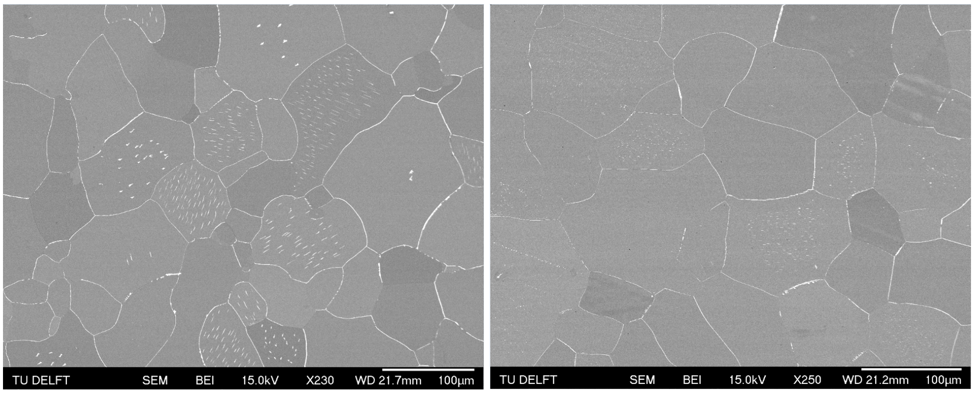

(a) Set-up 3 - 700°C-2h.

(b) Set-up 4: 700°C-2h.

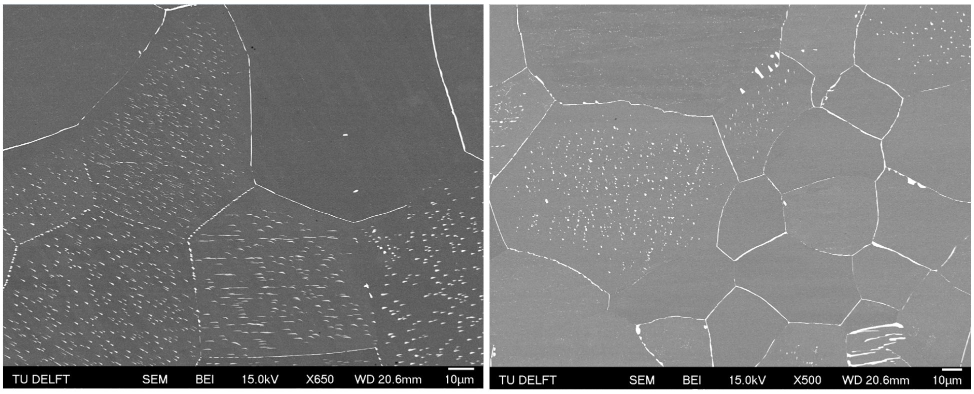

(c) Set-up 4: 700°C-16h.

(d) Set-up 4: 700°C-32h.

Figure 3.25: SEM backscattered electron images of final experiments for the Fe-Au alloy. A comparison of the different ageing times.

The same conclusions on the influence of the cooling rate from the previous section 3.4.2.1 can be applied to the qualitative analysis. Only by comparing the 2 hours experiment in set-up 3 and 4, which are at similar magnification, it is clear that on set-up 3 almost all the grain boundaries are covered and precipitation in the grain can be seen in many grain with a considerable size. However, in set-up 4 it is hard to see precipitation, the precipitation in the grain boundaries is much thinner and sometimes nonexistent and precipitation within the the grain is only present in a few grains and the particles are very small. For 16 and 32 hours, precipitation is observed in more grains, as well as in the grain boundaries.

In line with the preliminary results, the precipitation on the final Fe-Au alloy experiment was also inhomogeneous from grain to grain, and also precipitate-free zones were observed in some of them. It can be seen that the grain boundaries are the first location where Au-rich particles nucleate since for short times when most of the grain do not have precipitates, the grain boundaries are already identifiable due to precipitation.

The samples were analysed at higher magnifications in order to observe new features. Figure 3.26a shows that the precipitates shape remains the same, and round and needle-like precipitates are the two shapes observed, where all of the previous features were found: single or multiple preferential directions, two size precipitates which indicate two different nucleation times and a change in the pattern inside subgrains. However, for longer times, some coarsening of the Au-rich precipitate in the form of bands have been seen for 32 hours ageing, as presented in figure 3.26b. In these cases, the disk-like or needles precipitates in the grain disappear and instead, Au-rich patched or bands cover all of the grain. This coarsening only happens in a few grains. Moreover, a similar behaviour has been seen in grain boundaries for 2 hours ageing that could be the initial stage of this band-coarsening, as shown in figure 3.26c.

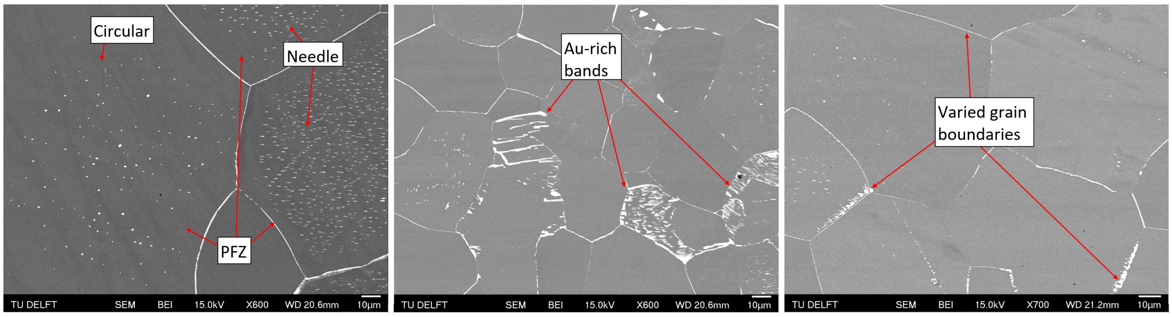

(a) round, needle-like precipitates and PFZ.

(b) Au-rich bands. Aged fro 32 hours.

(c) Grain boundaries after ageing 32 hours.

Figure 3.26: SEM backscattered electron images of final experiments (set-up 4) of the Fe-Au alloy. The shape of the precipitates, precipitate-free zone (PFZ) and the grain boundaries are showed with more detail at higher magnification.

3.4.2.3. Quantitative Results for the Fe-Au-W Alloy Surface Precipitation

The results from the electron backscattered spectroscopy have been informative since for the first time W-rich particles have appeared for the samples that have aged for 16 and 32 hours. The type of particles that were found were: Au-rich particles, W-rich particles, Au-rich grain boundaries and Au-W-rich zones with particles.

For the 2-hour experiment, only low-magnification measurements were taken. Au-rich particles and grain boundaries were observed together with porous W-rich particles. The matrix had the nominal concentration ~3 and ~4 wt.% of Au and W respectively. The grain boundary and Au-rich particles had ~ 40 wt.% of Au, and the porous W-rich particles were ~32 and ~26 wt.% W and Au. These measurements were taken at low magnifications. Therefore, for the Au-rich and W-rich particles the measurement could have measured part of the matrix and underestimate the content.

For the 32 and 16 hours experiment, a more thorough analysis at higher magnification was performed and new W-rich particles were found together with the previously observed in the 2-hours experiment. The Au-rich particles had ~ 73 of Au and ~ 0.6 of W wt.% (~ 38 of Au and ~ 0.3 of W at.%), which confirms all the previous work and expectations. The grain boundaries agreed on these results with ~ 73 – 80 Au wt.% and almost no W. If these result are compared to figure 3.20c, then if can be concluded that W avoids to precipitate on the grain boundary. Generally, Au-rich particles appear brighter in SEM images than W-rich, which made it easier to identify them.

With regard to the W-rich particles, there are two situations that were found:

1. W-rich particles: the particles had ~ 20 – 60 wt.% W and low ~ 2 – 5 wt.%Au. As can be seen in figure 3.27,

the high content particles have ~ 60 W wt.% and are generally porous and big (~ $1\mu m$) as point 1 and these composition coincides with Laves phase. The smaller precipitates (~ $100nm$) were found to have ~ 20 – 35 W wt.% and 1 – 2 Au wt.% (points 3, 4 and 5 in figure 3.27).

2. W-Au-rich particles: some precipitates were found to have intermediate contents of both W and Au, ~ 10 – 20 wt.% for both elements. These particles were small (~ $100nm$) and slightly brighter than W-rich and for this reason they were expected to be Au-rich. An example of this particle could be point 2 in figure 3.27. The resolution of EDS is around a micron and could affect to the measurements of the precipitates, since they are in the nano-scale and the matrix is full of W-rich precipitates.

As a conclusion of these results, it is clear that there are four types of precipitates that can be distinguished on the surface of the ternary alloy. Firstly, the Au-rich precipitates formed primarily at grain boundaries, that matches with the results of the binary alloy and the binary Fe-Au phase diagram. Then, there are big porous W-rich precipitates that coincide with the Laves phase composition and the binary Fe-W phase diagram. However, there are two types of precipitates that were found with unexpected compositions: small W-rich and W-Au-rich precipitates (~ $20wt.\%$ W and Au).

Atom%	C-K	O-K	Fe-K	W-M	Au-M
Base(3)_pt1	6.02	6.55	54.93	30.14	2.36
Base(3)_pt2	5.42		82.13	3.03	9.42
Base(3)_pt3	4.95		88.08	6.44	0.53
Base(3)_pt4	3.31		88.41	7.74	0.54
Base(3)_pt5	3.47		90.91	4.87	0.75
Base(3)_pt6	2.16		96.36	0.88	0.59

Weight%	C-K	O-K	Fe-K	W-M	Au-M
Base(3)_pt1	0.78	1.13	33.16	59.91	5.01
Base(3)_pt2	0.92		64.92	7.88	26.27
Base(3)_pt3	0.95		78.49	18.89	1.67
Base(3)_pt4	0.61		75.88	21.87	1.64
Base(3)_pt5	0.68		82.38	14.54	2.40
Base(3)_pt6	0.46		94.65	2.85	2.04

(a) BEI image of the analysed zone.

(b) Weight and atom % content.

Figure 3.27: EDS analysis of FeAuW with set-up 4.

Additionally, quantitative topological analysis was performed on the SEM images by ImageJ. Figure 3.28 presents all of the analysis done, where the results have been compared firstly with the preliminary experiments and afterwards with the final binary experiments. Figures 3.28a, 3.28c and 3.28b present the average equivalent diameter, the areal fraction and the number density compared to the preliminary ternary results, respectively.

The preliminary results in section 3.3 did not present any W-rich precipitation, just like in the final results for short ageing times (1-2 hours) and set-up 3. Therefore, there will be only a comparison for 1 and 2 hours ageing. It can be seen in figure 3.28a that for short ageing times, the average diameter of the final results was smaller but it seemed to follow the same growing trend of the preliminary. Additionally, in agreement with the binary results, set-up 3 behaves the same as the preliminary experiments. The number density for short times is higher and the areal fraction is of the same order as the preliminary results. Therefore, the conclusions from the binary experiments are confirmed and the cooling rate from the annealing temperature had an influence on the results. It seems that the slow cooling rate already enables precipitation at high temperatures, which resulted in lower number density but larger precipitates.

The final ternary results were also compared with the final binary results in figures 3.28d, 3.28e and 3.28. In figure 3.28d, the evolution of the average diameter with time is observed. For shorter times, where the ternary only presents Au-rich precipitates, both alloys seem to behave the same way. However, for longer ageing times (16-32 hours) it can be seen clearly that there is an influence with the precipitation of the W-rich precipitates in the average diameter (black square in figure 3.28a). W-rich particles were found to precipitate in high number density with a small size. Therefore, the influence is due to the impossibility to differentiate the Au-rich from the W-rich precipitates in the analysis the average diameter. Only in a few grains where both precipitates could be clearly differentiated by shape and size, the average diameter was calculated separately. The results are shown in the figure in blue for W-rich and red for Au-rich precipitates. It can be seen that Au-rich are bigger but do not reach the size of the precipitates of the binary alloy. Unfortunately, this situation only happens in a small percentage of the grains, and generally, the size was similar (Au-rich were never the smaller precipitate) and the precipitates were differentiated by shape and brightness under back-scattered imaging. Therefore, it could be concluded that the addition of W could have slowed down the growth of the gold precipitates.

In figure 3.28e the areal fraction is presented. The areal fraction on the ternary alloy has been calculated taking into account all the precipitations (W and Au-rich). A linear fit has been calculated and the ternary alloy has slope of 0.51 ± 0.13, which is higher that the binary (0.44 ± 0.12) and closer to Carlow's theory, whose research concluded on a slope of 0.5. As a conclusion, it could be said that regarding areal fraction, both alloys behave similarly and have the same coverage up to 32 hours. More experimental data for longer hours would be necessary to draw more detailed conclusions.

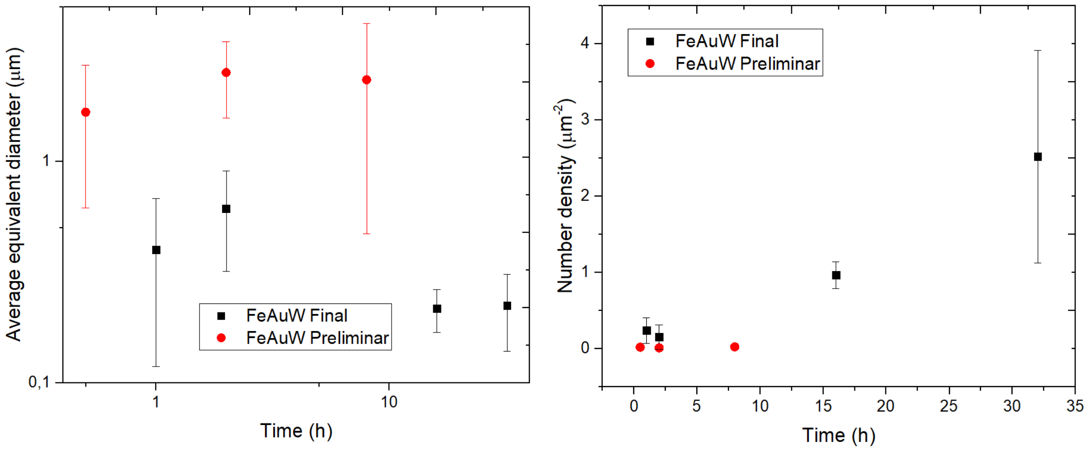

(a) Average diameter of final and preliminary results.

(b) Number density of final and preliminary results.

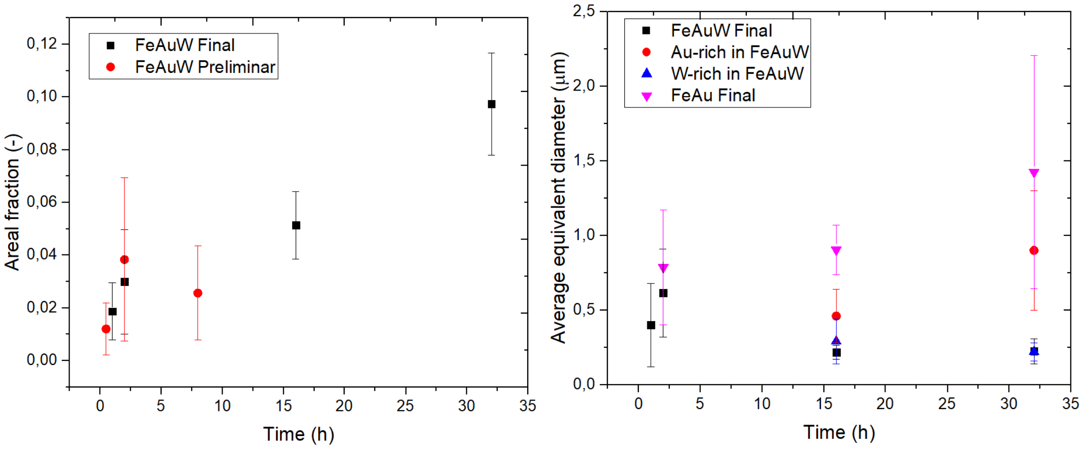

(c) Areal fraction of final and preliminary results.

(d) Average diameter of final results.

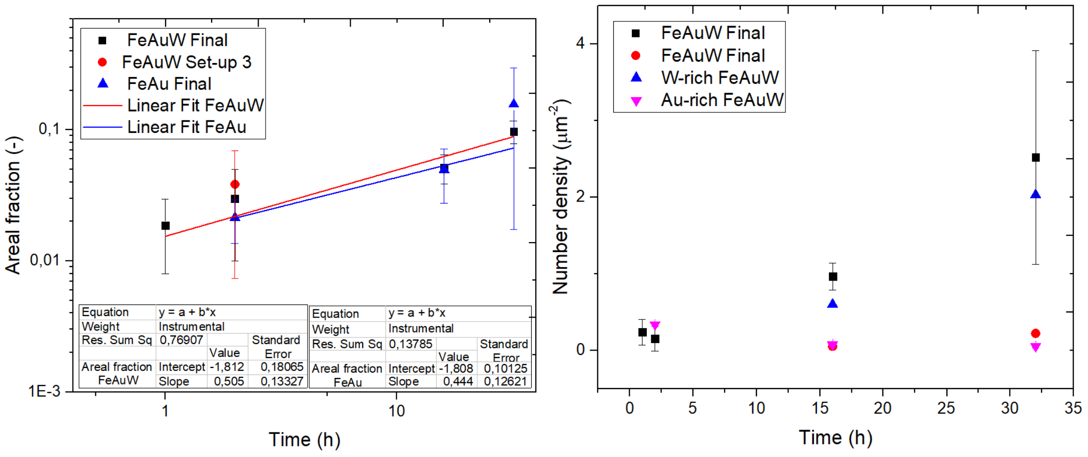

Equation	y = a + b*x		
Weight	Instrumental		
Res. Sum Sq	0,76907		
		Value	Standard Error
Areal fraction FeAuW	Intercept	-1,812	0,18065
	Slope	0,505	0,13327

Equation	y = a + b*x		
Weight	Instrumental		
Res. Sum Sq	0,13785		
		Value	Standard Error
Areal fraction FeAu	Intercept	-1,808	0,10125
	Slope	0,444	0,12621

(e) Areal fraction of final results.

(f) Number density of final results.

Figure 3.28: Analysis of the evolution with time of set-up 4 experiments on Fe-Au-W and comparison with preliminary on Fe-Au-W results and final results of Fe-Au.

Finally, the number density was analysed and presented in figure 3.28f. Contrary to the results of the binaries, where it seemed to have entered the coalescence regime,the precipitation on the ternary alloy shows a sudden increase for 16 hours onwards due to the precipitation of a high number of small precipitates that have governed the average equilibrium diameter of the precipitates. According to the overall calculations of the number density, taking into account W and Au-rich precipitates, the ternary alloy is still at the nucleation stage with simultaneous growth. As aforementioned, only in a few grains calculations to differentiate the precipitates could be performed and the number density of Au-rich precipitates is two orders magnitude lower than the W-rich precipitates, but they are in line with the binary results. However, these results are based on a few grains were the Au-rich could be identified, whereas in the rest of the grains, the Au-rich precipitates cannot be distinguished from the W-rich precipitates in terms of the size.

As a conclusion for the influence of the addition of tungsten in the binary alloy, several approaches could be taken:

- Overall approach: takes into account W-rich and Au-rich without differentiation. This approach is more reliable since more grains have been observed and taken into account in the quantitative calculations. From these results, it can be concluded that the addition of tungsten has delayed the coalescence of the precipitates and the number density has increasing number density. At the same time, this has had an influence on the average equivalent diameter, which has decreased. Taking both into account for the areal fraction calculations, the ternary areal coverage seem to achieve the same results as the binary, making it as efficient as the binary alloy, where for short times the Au-rich precipitates would precipitate and for longer times the combination of both precipitates.
- Split approach: this approach looks at W-rich and Au-rich separately. This approach is much more unreliable since only 7.5% grains could be analysed separately. Therefore, it is not representative and more data is necessary to increase the reliability of the calculations. By taking this into account, it can be concluded that the precipitation of W-rich particles has decreased the growth rate of Au-rich precipitates since the number density is kept the same, but the average equivalent diameter has decreased by ~ 50 – 60%.

3.4.2.4. Qualitative Results for the Fe-Au-W Alloy Surface Precipitation

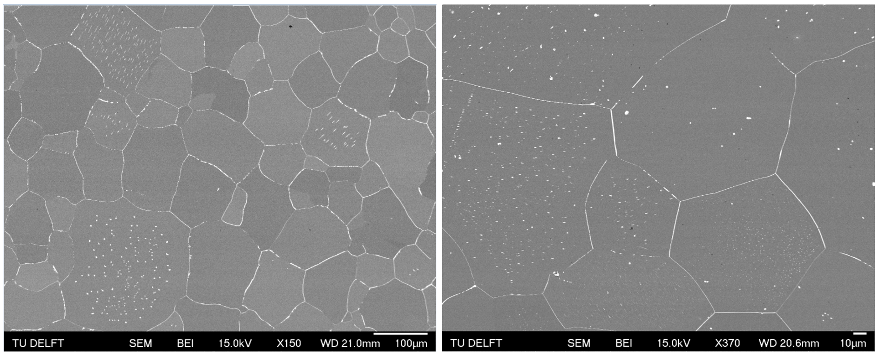

(a) Set-up 3: 700°C-2h.

(b) Set-up 4: 700°C-2h.

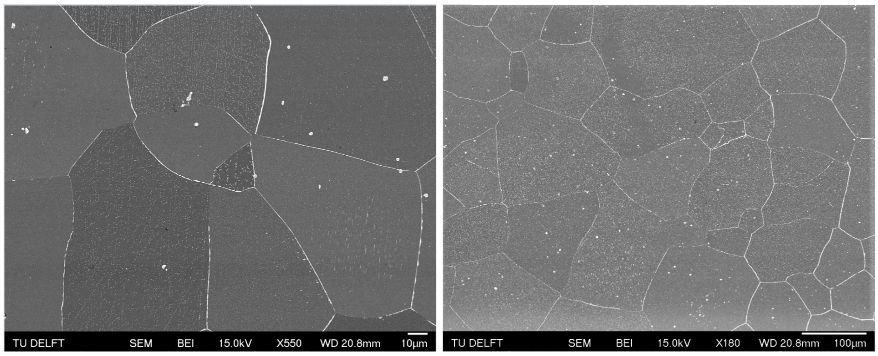

(c) Set-up 4: 700°C-16h.

(d) Set-up 4: 700°C-32h.

Figure 3.29: SEM backscattered electron images of final experiments for the Fe-3Au-4W alloy. Comparison of the different ageing times.

Together with the quantitative analysis, a qualitative one has performed. Figure 3.29 shows the general evolution of the precipitation with time.

If the 2 hours ageing is compared for the different set-ups 3 and 4 in figures 3.29b and 3.29b, respectively, it can be seen that the precipitation in set-up 4 is more disorganised, and many grains start to have a mixture of shapes, sizes and no clear patterns are seen as in set-up 3 and previous results on the binary alloy. Moreover, in figures 3.29c and 3.29d a high density of W rich precipitates can be observed together with the gradual disappearance of the high density and patterned Au-rich grains. For 16 and 32 hours there is W-rich precipitation in all of the grains and in some of them big and very bright (under backscattered SEM images) Au-rich precipitates are spotted.

There are some features of the Au-rich precipitates that are in common with the binary results, such as the change in precipitation density and shapes from grain to grain and the presence of Au-rich grain boundaries. In the case of W-rich, the precipitation density changes from grain to grain. However, it has been observed in many occasions that these precipitates nucleate along preferential direction that have a continuity from grain to grain. In figure 3.29c it can be observed along the vertical directions.

A more detailed analysis was performed at higher magnification. Apart from round and needle-like Au-rich precipitates, triangular precipitates were found and they seem to follow a preferential direction as can be seen in figure 3.30a. The two situations mentioned above related with the precipitation of W and Au rich are presented in figures 3.30c and 3.30b. The former figure presents the situation in which the Au-rich precipitates can be identified by shape and size, where they still maintain the pattern and preferential directions typical from the binary alloy. The latter, present a more representative situation, in which the Au-rich particles blend with the W-rich particles since they have similar sizes and shapes. In these cases, Au-rich are equiaxed and have rounded edges, whereas W-rich can be seen in plates or equiaxed shapes, but always with sharp edges. Moreover, these grains seem to have less Au-rich precipitates and these precipitate are rather spatially scattered without following a typical pattern.

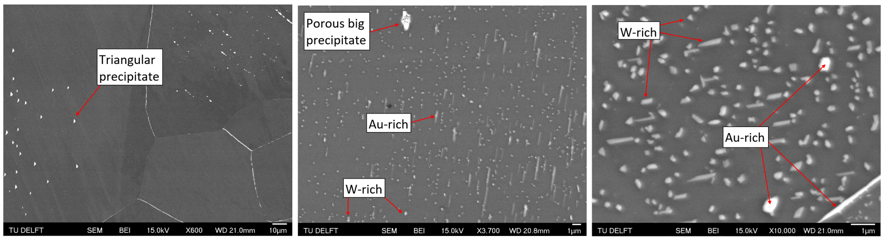

(a) Triangular precipitate. Aged for 16 hours.

(b) Example of W-rich and Au-rich precipitates at 16h ageing.

(c) Example of W-rich and Au-rich precipitates at 16h ageing.

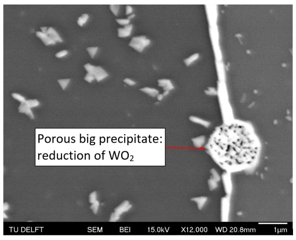

(d) Example of tungsten oxide reduction with oxygen.

Figure 3.30: SEM backscattered electron images of final experiments (set-up 4) for the Fe-Au-W alloy.

The last type of W-rich precipitate that was described earlier is the big porous rounded precipitates that can be seen in figure 3.30d. This type of precipitates has been observed at all times ageing times from set-up 4, even when the small W-rich precipitates have no precipitates yet. The change in morphology of tungsten oxide reduced by hydrogen has been studied by Venables and Brown [46]. The reduction of WO_3 by hydrogen was studied at different temperatures: 575, 675, 775, 875 and 975 ºC. The reduction occurs as a sequence of four stages, the initial WO_3 oxide gets reduced in four steps at the same time as the the morphology of the oxide changes. The final reduction step occurs from WO_2 to $\alpha - W$ where the resulting morphology consist on 'rounded mounds of coral-like clusters'. The ageing time for the surface precipitation experiment has been 16 hours, and the time necessary according to Venables et al. [46] to complete the reduction of WO_3 to $\alpha - W$ is 8100 seconds, which corresponds to 2 hours and 15 minutes. Therefore, a possible origin of those big rounded tungsten-rich particles with a porous morphology could be the reduction of prior tungsten oxides present in small amounts in the starting material.

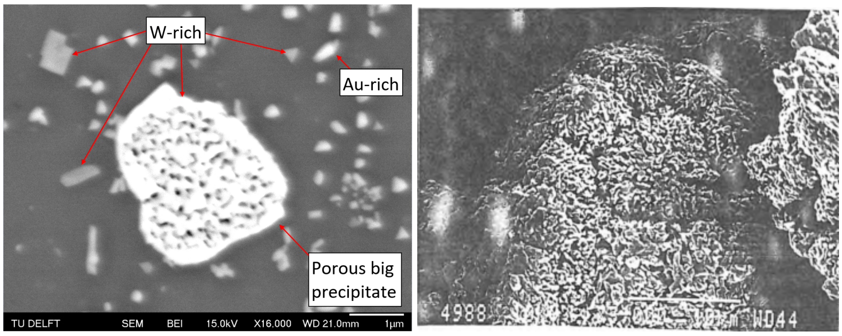

(a) Image of WO_2 reduction after ageing 16 hours. (b) Image of WO_2 reduction from Venables results [46].

Figure 3.31: SEM backscattered electron images of preliminary experiments for the Fe-Au alloy. Comparison of the precipitates shapes, grain boundaries thickness, subgrains and preferential directions.

3.4.2.5. Supplementary Analysis: EBSD and TEM Results

All the analyses that were done on the precipitates suggest that the crystal orientation of the grains is the most likely cause of the different shapes and distributions of the precipitates among the grains. For this reason, Electron Back-scattered Diffraction (EBSD) was performed on one annealed sample of the ternary alloy. The heat treatment applied to the samples was according to set-up 4 and aged for 1 hour. The EBSD was performed with a step of $3\mu m$. A 93% index rate was achieved, where only Au-rich particles were identified besides the bbc Fe matrix. Unfortunately, these precipitates were not big enough for EBSD to recognise their crystallographic orientation and only a qualitative relation could be made. The precipitation of ten grains was analysed as is shown in figure 3.32. Grains 1,4,9 and 10 have needle-like precipitates, where 1 and 10 has precipitates with very low aspect ratio. On the other hand, grains 2, 3, 6, 7 and 8 had more round precipitates. Therefore, it can be concluded that there is a relationship between the crystallographic orientation of the grains and the shape of the Au-rich precipitates, as shown in equation 3.1. However, it should be noted that not many precipitates were detected due to their small size.

$$\begin{aligned} 111_{Fe} \rightarrow Au \quad & \text{round precipitates (high aspect ration)} \\ 101_{Fe} \rightarrow Au \quad & \text{needle precipitates (low aspect ratio)} \end{aligned} \tag{3.1}$$

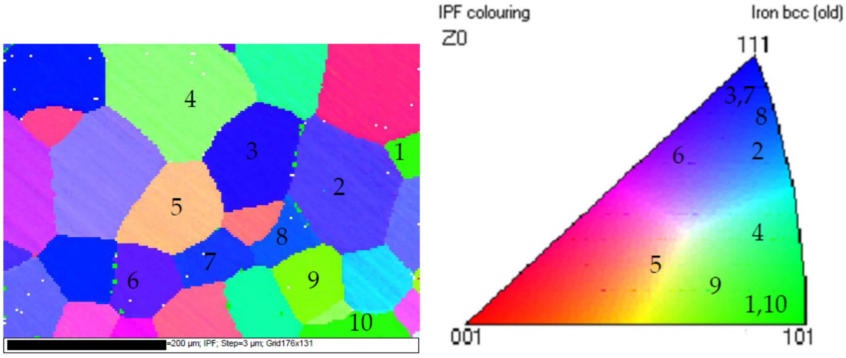

(a) EBSD map. (b) EBSD results.

Figure 3.32: Electron backscattered diffraction (EBSD) for the Fe-Au-W alloy aged for 1 hour and heat treated according to set-up 4 (see table 3.2).

Additionally, TEM analysis was performed in Fe-Au-W failed creep samples which show bulk and grain boundary precipitation. TEM complements the information obtained with SEM by providing information of the structure of the sample such as the crystal structure and lattice orientation relationships.

The results from the TEM analysis confirmed that the Au-rich precipitates have a FCC structure with a lattice parameter of a=3.95 ± 0.06 Å, which corresponds to a composition of 61±20 at.% Au. This experiments were performed at 550 °C and the results agree with the phase diagram. The experiments performed in this thesis are at 700°C, where the crystal structure is expected to be the same but the composition has 58 at% Au.

The shape of the precipitates was found to be plate-like. The Au-rich precipitates found in surface precipitation have needle-like or round shapes. There could be a relation, where depending on the crystallographic direction of the matrix the round precipitate would correspond to the planar face of the 3D-plate and needle-like shape would correspond to the thickness of the 3D-plate.

Moreover, dislocation were always linked to some precipitates. This results can be linked to the indentation experiments, where precipitation was induced in grains that did not present precipitation in the flat surface 3.36c. Therefore, this change in the precipitation pattern induced by the indentation could be due to the dislocations that are formed during deformation.

Finally, the TEM results shows some situations in which W and Au-rich particles precipitates separately, but in others, W-rich and Au-rich were in contact and even forming a type of sandwich structure. These last situation could explain the unexpected EDS readings for the Fe-Au-W alloy with high contents of Au and W.

3.5. Precipitation at Locally Deformed Surfaces

Apart from assessing the evolution of the precipitation with time, this thesis has also analysed the influence of deformation on surface precipitation. In this case, the deformation has been chosen to be local and prior to the heat treatment. A spherical indentation has been performed at different depths using a Brinell hardness machine, since spherical indentation will assess the strain influence in all of the crystallographic planes.

All along the indentation there is a strain gradient, that will influence the surface precipitation, since the higher the strain, the easier it is to nucleate a precipitate. Therefore, each indentation (which will have a round shape) will be analysed in the along its radius *a*, where *a* is the radius of the indent. The new dimensionless parameter *r/a* for this purpose is defined, where *r* is the position along the radius of the indent, *a*. Therefore the analysis will be done at *r/a*=0 (centre of the indent and load application axis), *r/a*=0.5 (half way between the centre and the edge of the indent) and *r/a*=1 (edge of the indent).

As explained in section 2.4, the strain field can be calculated as a function of the indent in the material represented by the dimensionless parameter *a/R*, where *R* is the radius of the indenter. For each*a/R* there is a different strain field and a maximum equivalent strain defined. In this section, the indentation results will be displayed in function of *a/R* and the equivalent maximum strain. In this thesis three indentations at three different depths have been performed in each sample, Fe-Au and Fe-Au-W, after the annealing at 868 ºC for 8 hours and the mechanical polishing. The measures of *a* are the same on both Fe-Au and Fe-Au-W for each indentation depth. Figure 3.33 presents the hardness results obtained from the indentation experiments.

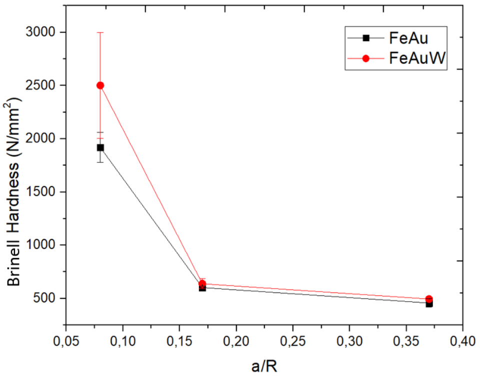

Figure 3.33: Hardness of Fe-Au and Fe-Au-W with respect to the depth of the indentation, which is represented by the dimensionless parameter *a/R*.

Table 3.7 show the results of the indentation experiments: the nominal depths, the applied loads, the final indentation depth after the elastic strain recovery and the dimensionless parameter *a/R* that corresponds to each indentation depth. Moreover, in this table the equivalent strain calculated according Chaudhri's findings on copper [32]. It has been assumed that same strain field, as presented in figure 2.3 in section 2.4. The equivalent strain is going to be calculated in three locations: $\frac{r}{a}=0$, $\frac{r}{a}=0.5$ and $\frac{r}{a}=1$. These calculations are represented in the table as $\epsilon(\frac{r}{a}=X)$, where the maximum strain is in the centre of the indentation. The strains were also calculated by an alternative method [33], which is mostly applicable for high intermediate *a/R*, but that reached to the same conclusion: the highest precipitation is expected in the indentation of highest load and depth. However, according to Chaudhri's studies later on [33], spherical indentations with low *a/R* between 0.08-0.105 (which is the case for the indentation of 45 μm deep) have a maximum strain located at $\sim\frac{r}{a}=0.5-0.8$. As a conclusion, in the experimental results, most precipitation is expected in the maximal strain regions, which are at *r/a*~0.5 for *a/R*=0.08 and at *r/a*~0 for *a/R*=0.17 and 0.37.

Table 3.7: Indentation *a/R* parameter and equivalent strain for the observed regions for the Fe-Au and Fe-Au-W indentations.

Depth [μm]	**Load Fe-Au** [*N*]	**Load Fe-Au-W** [*N*]	$h_{min,av.}$ [μm]	a/R	$\epsilon_{\frac{r}{a}=0}$	$\epsilon_{\frac{r}{a}=0.5}$	$\epsilon_{\frac{r}{a}=1}$	ϵ_{max}
45	222 ± 18	291 ± 59	31 ± 4	0.08	0.023	0.028	0.037	0.019
90	586 ± 13	621 ± 44	69 ± 7	0.17	0.047	0.057	0.075	0.047
180	1220 ± 105	1335 ± 32	149 ± 7	0.37	0.107	0.130	0.170	0.145

3.5.1. Results for the Locally Deformed Samples

The results of the deformation experiments have been assessed qualitatively. As it will be shown, the precipitation on the indentation surface is not uniform and is very scattered and for this reason together with timing issues, only a few grains have been observed at high magnifications and the quantitative analysis are not representative of the real situation. Nevertheless, these few grain have been analysed to get a rough idea of the precipitation in the indentation. This will be complemented by qualitative observation of the general images of the indentations, that are more representative. Due to the imperfections of the ball, some scratches were made together with the indentation and the quantitative analysis has tried to avoid those imperfections.

This section will firstly present the results on the binary Fe-Au alloy and end up with the ternary Fe-Au-W alloy.

3.5.1.1. Indentation for the Fe-Au Alloy

Figure 3.34 presents the quantitative analysis of the precipitation on the indentation surface. As explained in section 2, the indentation will introduce deformation and strain field in the material which will come together with higher density of dislocations. This dislocations are sites with higher surface energy and high diffusion paths. Therefore, precipitates have a lower nucleation barrier due to the fact that they will destroy defect interface and possibly their growth would be faster as diffusivity through dislocations, known as pipe diffusion, has been observed to be faster.

Due to the large variety of shapes and densities of precipitates found in the indents, the areal fraction has been chosen as the parameter to compare the amount of precipitate present along the indentation. The three figures present the evolution of areal fraction per indentation depth and the same scale has been used in order to be able to compare between them.

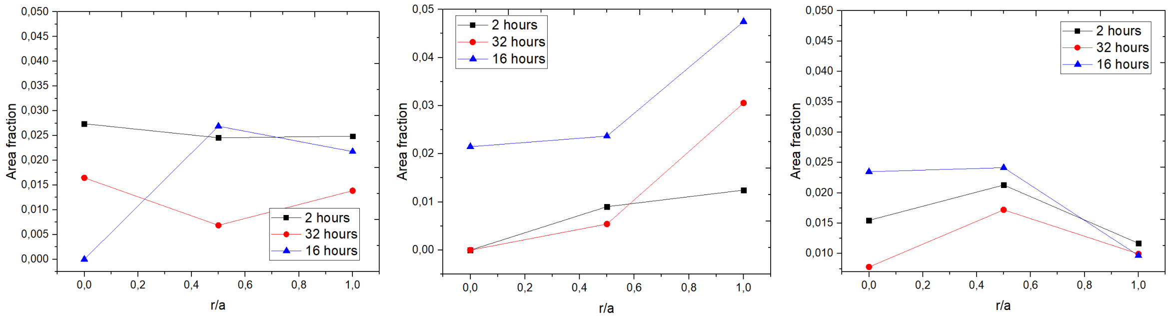

(a) Indentation depth: 45 μm.

(b) Indentation depth: 90 μm.

(c) Indentation depth: 180 μm.

Figure 3.34: Quantitative analysis of indentations on Fe-Au alloy. The results will show the progress of number density, average equivalent diameter and areal fraction along the radius of the indent, represented by the dimensionless parameter *r/a*, where *r* is the position along the indent.

It can be seen that the quantitative analysis does not really represent the expected situation because they present that the *a*/*R*=0.08 indent (45 μm) shows comparable areal fraction to the others *a*/*R*=0.17 and 0.37, when qualitatively it is clearly the opposite as seen in figure 3.35. Moreover, the values are even lower that the normal surface experiments (see figure 3.23b). The incoherence of these results could originate from two reasons. (i) Only a few grains were analysed per *r/a* and the zones were chosen to avoid imperfections. (ii) A feature that has been observed on the post-analysis of the images were the Au-rich band as a phenomenon that occurred as a consequence of the coalescence of Au-rich particles in the normal surface. However, these were precisely the grains that were avoided in these calculations and that could have made the difference. As it can be observed in figure 3.35, these Au rich band only appear for the 32 hour experiment. From this results it can be concluded that more quantitative analysis of the indentation needs to be done to deduce quantitative conclusions.

For the qualitative analysis, figure 3.35 presents all the indentation sequence. The fist row (figures 3.35a, 3.35b and 3.35c) shows the indent at each depth after 2 hours ageing. The second and third rows the same for 16 hours and 32 hours, respectively.

For the 2 hours ageing, slightly more precipitates were found compared to the surrounding flat surface. Not much difference between the different *a/r*, where precipitation is observed in very few grains, and mostly between *r/a*=0.5-1, which is not expected according to the spherical indentation theory.

For 16 and 32 hour of ageing, more precipitation is observed at the indentation and a clear difference between the different *a*/*R* is observed.

For the 16 hours more precipitation was observed inside the indent compared to the flat surface. In the case of *a*/*R*=0.08 (figure 3.35d), most of the precipitation is found in between *r*/*a*=~ 0.6 – 1 as expected according to [33]. For the *a*/*R*=0.17 the centre is covered with precipitates. Precipitation is also observed at *r*/*a*~0.5 and in some grains *r*/*a*~1. This situation is in between the two expected distributions based on [33]. In the case of *a*/*R*=0.37, the precipitation is mostly at *r*/*a*~ 0 and it extends to *r*/*a*~ 0.6 , as predicted by the theory.

Similar results to the 16 hours are obtained in the 32 hours experiments. For *a*/*R*= 0.08, most of the precipitates are found at *r*/*a*=~ 0.6 – 1 with the addition of some precipitation in the centre *r*/*a*=0. In the case of *a*/*R*=0.17, no precipitation was found in *r*/*a*=0 and only a few grain around *r*/*a*~0.8 with one Au-rich band. This precipitation agrees with the expectations for *a*/*R*=0.08-0.105, but not for *a*/*R*=0.17. The precipitation for *a*/*R*=0.37 was similar but Au-rich bands are found in various grains, mostly locates at *r*/*a* ~0.8-1, which could be originated due to the contribution of large ageing times. However, this coalescence did not occur in the middle of the grain were the maximum strain is located and it would have been expected. Again, it seems that for the binary alloy, the precipitation do not follow the expectation set by the theory.

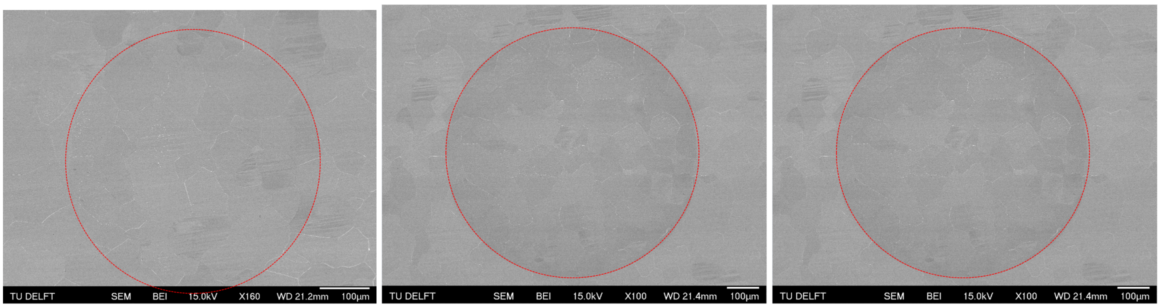

(a) Aged 2 hours. Indentation depth: 45 μm. (b) Aged 2 hours. Indentation depth: 90 μm. (c) Aged 2 hours. Indentation depth: 180 μm.

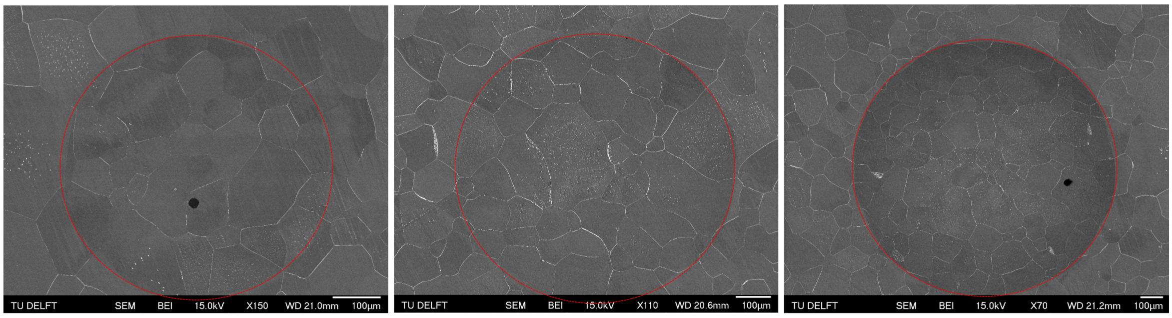

(d) Aged 16 hours. Indentation depth: 45 μm. (e) Aged 16 hours. Indentation depth: 90 μm. (f) Aged 16 hours. Indentation depth: 180 μm.

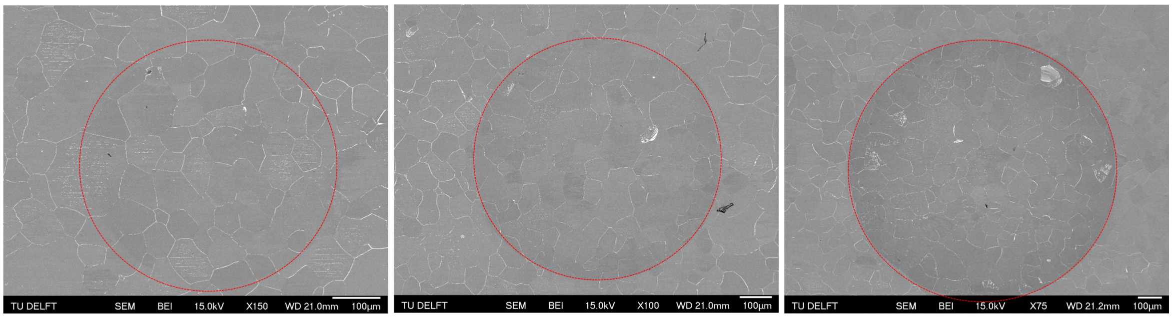

(g) Aged 32 hours. Indentation depth: 45 μm. (h) Aged 32 hours. Indentation depth: 90 μm. (i) Aged 32 hours. Indentation depth: 180 μm.

Figure 3.35: SEM backscattered electron images of preliminary experiments for the Fe-Au alloy. Comparison of the precipitates shapes, grain boundaries thickness, subgrains and preferential directions.

Finally, special features from the indentations were analysed also at higher magnification. In figures 3.36a, 3.36b and 3.36c, the precipitation at the edge of the indent for each indentation depth can be observed. In all of the cases, the precipitation density, shape and preferential direction changes in the same grain when the indent starts . It can be concluded that the indentation does influence the surface precipitation, as it can change the orientation of the crystal matrix and generate dislocations. Finally, the appearance of Au-rich bands was also observed in the indentations, as shown in figure 3.36d .

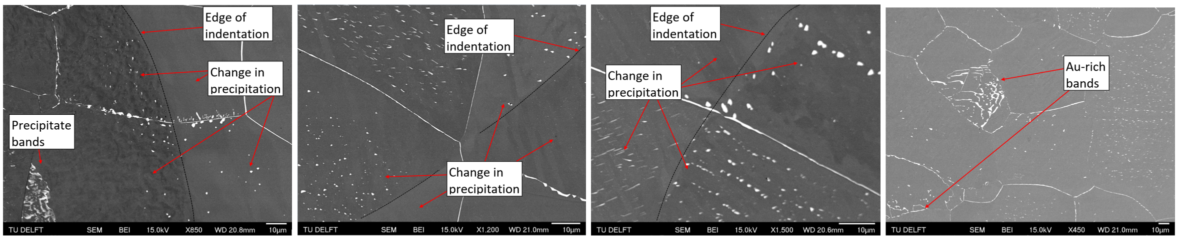

(a) Precipitation on the edge for *a*/*R*=0.08.

(b) Precipitation on the edge for *a*/*R*=0.17.

(c) Precipitation on the edge for *a*/*R*=0.37.

(d) Au-rich precipitation band at *r*/*a*=0.5 for 32 hours ageing.

Figure 3.36: SEM backscattered electron images of preliminary experiments for the Fe-Au alloy. Comparison of the precipitates shapes, grain boundaries thickness, subgrains and preferential directions.

3.5.1.2. Indentation for the Fe-Au-W Alloy

There are many more precipitates due to the presence of W-rich precipitates. An alignment of the precipitation direction of the W-rich rich precipitates has been observed. No Au-rich bands are observed. Pores are observed, but not selective precipitation. This could be because the precipitates already nucleated at dislocations.

In figure 3.37 the evolution with time and the comparison of the different indentation depths can be observed. The indentation with *a*/*R*∼ 0.08 shows an areal fraction with coincides with the precipitation on the flat surface for the 2, 16 and 32 hours ageing and no difference is observed along the radius of the indent. In the case of *a*/*R*∼ 0.17 and 0.32, the 2 hour experiment also give the same results of areal coverage as the flat surface. However, for longer ageing times there is an increase in the areal coverage. These results do not coincide with the qualitative observations (see figure 3.38), where it is clear that there is more precipitation at the indentation than on the flat surrounding surface. This incoherence in the results can be due to the observed grains. In the same way as with the binary alloy, this quantitative analysis was carried out with only a few grains which do not represent the the whole population. Therefore more analysis is necessary to draw quantitative conclusions.

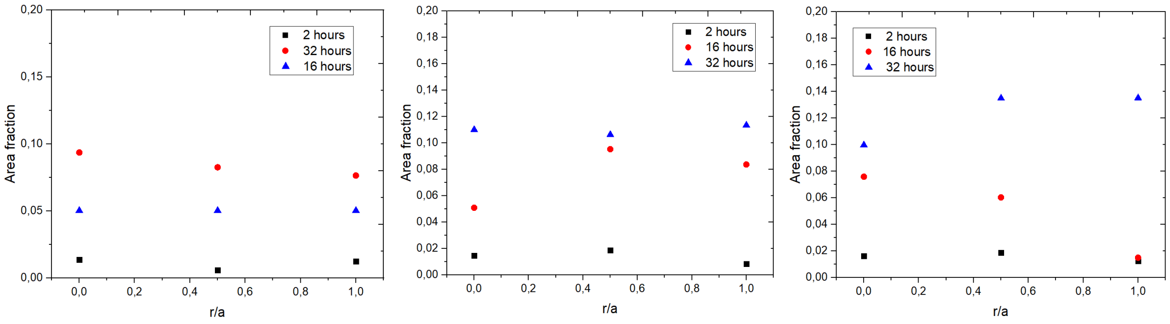

(a) Indentation depth: 45 μm.

(b) Indentation depth: 90 μm.

(c) Indentation depth: 180 μm.

Figure 3.37: Quantitative analysis of indentations for the Fe-Au alloy. The results show the progress of number density, average equivalent diameter and areal fraction along the radius of the indent, represented by the dimensionless parameter *r*/*a*, where *r* is the position along the indent.

For the qualitative analysis, figure 3.38 presents the precipitation sequence by rows. Each row presents the precipitation for the same ageing time but for different *a*/*R*. As expected by the quantitative analysis, it can be observed that longer ageing times results in more precipitation. In terms of the load, there is a higher difference between the precipitation on the flat surface and at the indent for higher loads. However, the difference between different *a*/*R* is harder to determine. The *a*/*R*∼0.08 presents most of the precipitation around *r*/*a*∼0.5-0.8 for the three ageing times, , as expected by theory. *a*/*R*∼0.17 and 0.37, for 2 hours ageing, there is precipitation all over the indent and no specific locations can be distinguished. However, for longer times, it can be observed that most of the precipitation is located towards the centre, *r*/*a*∼0-0.8. On the contrary to the binary results, ternary results are more in agreement with the theoretical research.

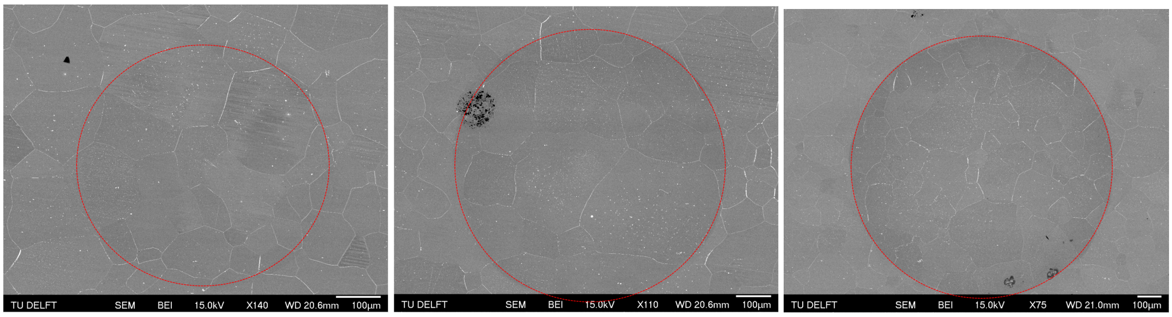

(a) Aged 2 hours. Indentation depth: 45 μm. (b) Aged 2 hours. Indentation depth: 90 μm. (c) Aged 2 hours. Indentation depth: 180 μm.

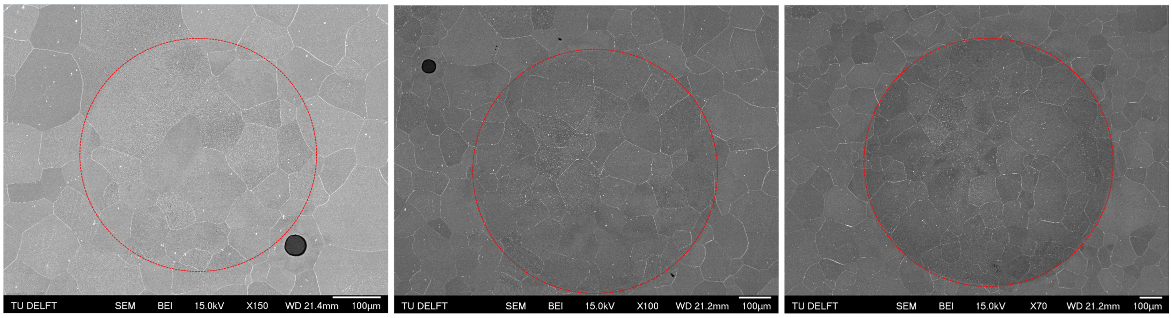

(d) Aged 16 hours. Indentation depth: 45 μm. (e) Aged 16 hours. Indentation depth: 90 μm. (f) Aged 16 hours. Indentation depth: 180 μm.

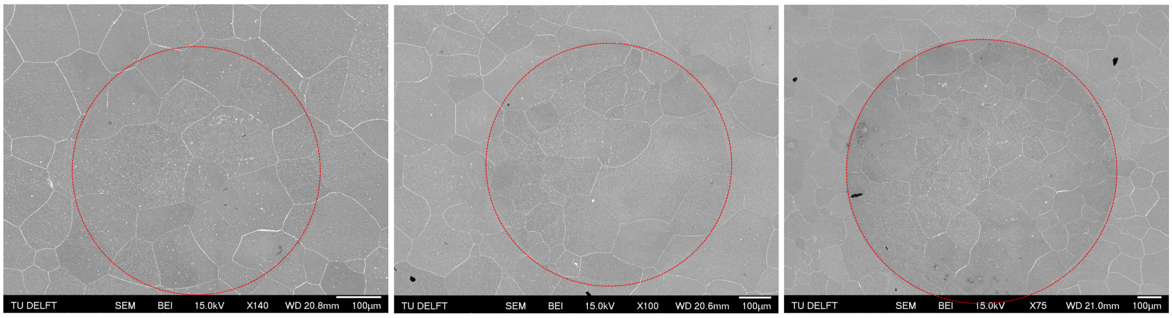

(g) Aged 32 hours. Indentation depth: 45 μm. (h) Aged 32 hours. Indentation depth: 90 μm. (i) Aged 32 hours. Indentation depth: 180 μm.

Figure 3.38: SEM backscattered electron images of preliminary experiments for the Fe-Au-W alloy. Comparison of the precipitates shapes, grain boundaries thickness, subgrains and preferential directions.

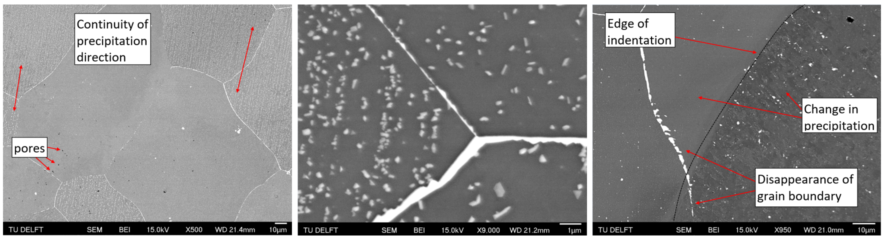

(a) Aged 16 hours. Indentation depth 45 μm and r/a=0. (b) Aged 16 hours. Indentation depth 90 $\mu m$and r/a=0.5. (c) Aged 16 hours. Indentation depth 180 μm and r/a=1.

Figure 3.39: SEM backscattered electron images of indentation experiments for the Fe-Au-W alloy. Images of the frequent features in the indentations.

4

Experimental Self Healing Creep Steels

During the second part of the thesis, the research on self-healing properties has been complemented by observing multi-component alloys, which are closer to the commercial industrial steel alloys. This is the first time in which self-healing properties have been assessed in alloys that resemble the industrial steel compositions. This chapter starts with the motivation of this set of experiments. Secondly, detailed description of their set-up will be presented. It will be followed by a discussion of the results from the warm-deformation experiments. Finally, the results of the cold-deformation will be discussed.

4.1. Motivation for Experimental Self Healing Creep Steels Experiments

The alloys that have been considered as a study object are a set of three self-healing creep steels developed by Yu within the Novam research group. Yu has designed ferritic heat resistant steels able to work under creep and corrosive conditions, besides having self-healing properties. Based on industrial power plants, these alloys have been designed to serve at 550ºC at the same time as achieve high mechanical properties by precipitation ($M_{23}C_6$) and solid solution strengthening. As for the self-healing properties, tungsten has been chosen to be the healing agent by precipitating as Laves phase.

Based on commercial steels, the composition of the alloys consists on W as a healing agent, Si and Mn for solid solution strengthening, Cr for heat resistance, and C for solid solution strengthening and the formation of $M_{23}C_6$ hardening particles together with Cr. The target microstructure of the alloy at service temperature should consist of a fully ferritic iron matrix, with only strengthening $M_{23}C_6$ and Laves phase.

The composition of the alloys has been calculated by means of a genetic algorithm and taking into account the creep cavity formation kinetics and the Laves phase incubation time from further experimental research. The incubation time of the Laves phase depends on its driving force, which according to classical nucleation theory: $t_{incub} \propto \textit{exp(chemical driving force}^{-1})$. However, Yu used a simplified relation based on the empirical results $t_{incub} \propto \textit{driving force}^{-1/2}$. Experimental results on commercial steels show that there is a linear relationship between temperature and incubation time, as can be seen in figure 4.1. Taking both of the relations into account, the genetic algorithm has reached to three different alloys of similar mechanical and different self healing properties at 550 ºC. The chemical composition is presented in table 4.1, where the difference in self-healing mechanism stems from the different driving forces of the Laves Phase and only alloy 2 is aimed to match the creep-cavity kinetics.

Table 4.1: Designed chemical composition (in wt%) of the three experimental creep steel alloys developed by Yu [47].

Alloy	**C**	**Cr**	**Mn** (wt.%)	**Si**	**W**	T_{anneal} [K]	**Phase configuration** [%]	**Driving Force** [$Jmol^{-1}$]
1	0.026	12	0.81	0.32	1.45	1473	BCC + 1.03 Laves + 0.52 $M_{23}C_6$	2964.2
2	0.023	12	0.32	0.65	2.23	1473	BCC + 1.87 Laves + 0.46 $M_{23}C_6$	4218.4
3	0.023	13.03	0.01	0.97	3.0	1473	BCC + 2.6 Laves + 0.72 $M_{23}C_6$	4848.8

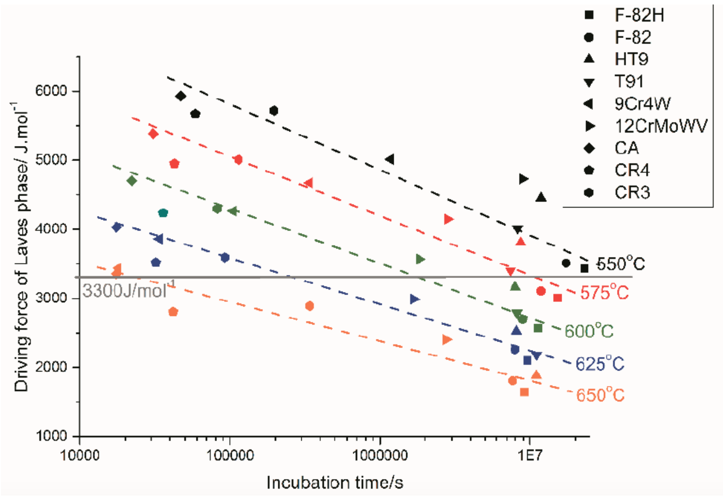

Figure 4.1: Incubation time of Laves Phase according to the experimental results of commercial steel alloys gathered by Yu [47].

As can bee seen in table 4.1, the driving forces of alloys 1, 2 and 3 are in the order of $\sim 3000, 4000$ and 5000 $Jmol^{-1}$. Making use of the experimental results from figure 4.1, a quick calculation of Laves phase incubation time can be done and they are expected to appear after 1700 and 300 hours for alloys 2 and 3, respectively. Verifying experimentally the self healing properties of this alloys is quite a challenge. In this thesis, it has been proposed to accelerate and observe site selectivity between nucleation sites of Laves phase by introducing strain energy.

Two types of deformation modes have been performed to introduce strain fields in the samples. On the one hand, warm concurrent deformation has been performed as it recreates similar conditions as for creep deformation. On the other hand, cold local deformation has also been performed in the surface in the form of indentations in order to observe precipitation on the surface.

4.2. Experimental Set-up

The material that has been studied has been manufactured by Northeastern university of China whose composition is listed in table 4.1. The raw material came as a cold-rolled sheet that were cut by spark erosion into small orthohedron with dimension of $\sim 5x5x10 mm^3$ and in cylinders of $\sim 5mm$ diameter x$10mm$ long.

As aforementioned, two types of experiments were performed according to the way the deformation was applied in the samples. The first type consists on concurrent warm deformation, where uniaxial stress was applied during the ageing of the sample. The prior cold deformation was performed via indentations with the ZHV30 ZWICKI-LINE Hardness tester with the Brinell indentor. Table 4.2 presents a summary of the different experiments performed.

Table 4.2: Summary of the heat treatments for the experimental self healing creep steels.

Nº	Alloy	Furnace	Annealing	Cooling Rate	Ageing	Stress [MPa]
1	Alloy 3	Dilatometer	1200°C-5 min	20°C/s	550°C- 50 hours	0
2	Alloy 3	Dilatometer	1200°C-5 min	20°C/s	550°C- 50 hours	100
3	Alloy 3	Dilatometer	1200°C-5 min	20°C/s	550°C- 50 hours	125
4	Alloy 3	Dilatometer	1200°C-5 min	20°C/s	550°C- 50 hours	150
5	Alloy 3	Dilatometer	1200°C-5 min	20°C/s	550°C- 50 hours	175
6	Alloy 3	Dilatometer	1200°C-5 min	20°C/s	550°C- 50 hours	200
7	Alloy 1	Silica	-	-	550°C- 80 hours	Indent
8	Alloy 2	Silica	1150 - hours	Quenched	550°C- 80 hours	Indent
9	Alloy 3	Silica	-	-	550°C- 80 hours	Indent

4.2.1. Warm Concurrent Deformation Experiments

The samples have been polished and cleaned by ultrasonic bath in ethanol prior to the heat treatment. The heat treatment of the warm deformation experiments has been performed in a dilatometer under vacuum (~ 10^{-6} mbar), where the samples were heated by a induction heating coil and compressed with a uniaxial force.

A thermocouple had to be welded to the sample before entering the dilatometer. The equipment used for the welding was a spot electric-resistance welding machine. The chamber was fluxed with helium before and at the end of the heat treatment. The heating rate of the dilatometer was set at 10 ºC/s, and the cooling rate at 20 ºC/s. The necessary cooling rate had to be calculated experimentally, because no forced cooling could be used as it would interrupt the vacuum in the chamber.

There are several limitations of the dilatometer that must be taken into account: (i) the machine has to be maintained at 20 ° C by an external cooling system, (ii) limited demand of power during long periods of time, (iii) deformation can only be applied by compression or torsion loads, and (iv) the samples must be cylindrical, 10 mm long and with a diameter of 5 mm.

The heat treatment performed to obtain surface precipitation for the warm deformation experiments consisted of two parts. It was observed in the raw material that after the cold-rolling at 800°C the matrix was not fully ferrite and a small FCC phase fraction was found in the iron matrix. Therefore, first of all, the samples were annealed at 1200°C for 5 minutes in the single α iron phase in order to obtain an homogenised microstructure. In the second part of the heat treatment, the samples have been aged isothermally at the same time as a load was applied uni-axially along the longitudinal direction. Alloy 3 was the tested alloy, as it has the highest driving force and the shortest incubation times. The ageing temperature was chosen to be 550ºC for 50 hours, which resulted in a good combination of driving force and incubation time that will enable to observe the evolution of precipitation in an appropriate time scale for this thesis. Figure 4.2 presents the temperature and stress cycle applied to each the samples.

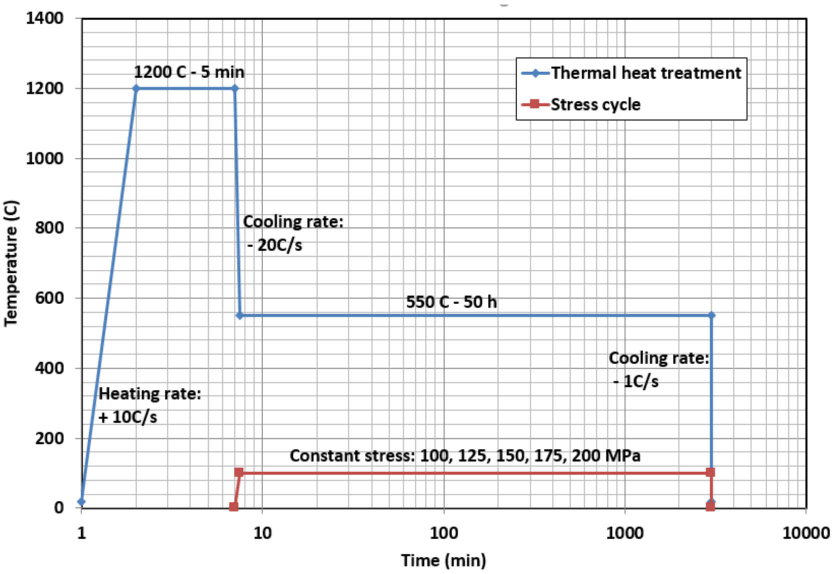

Figure 4.2: Heat treatment for the warm in-situ deformation experiments.

According to the manual, 1500 ° C is the maximum working temperature of the dilatometer, therefore, 1200 ° C for 50 hours is considered to a safe operating condition.

The deformation was applied by compression, even though tension would be more effective to generate cavities. The samples had the required dimensions, but the prior grinding and polishing of the samples required a rectangular prism shape instead of cylindrical.

4.2.2. Cold Prior Deformation Experiments

Together with the deformation at high temperatures, also local deformation has been assessed. These experiments have been performed in the same way as the indentations for the binary and ternary alloys in section

3.2.

The deformation has been done by indentation with the ZHV30 ZWICKI-LINE Hardness tester with the Brinell indentor. Two indentors were used: a ball of 2.5 mm and 5.0 mm diameter. The speed of the load application was 80μ m/min, the removal speed was 5 mm / min and the load holding time was of 10 seconds. There are two ways to control the indentation in a hardness test: by setting the maximal load or the maximum depth. Maximum depth was chosen for the 2.5 mm balls and maximum force for the 5 mm diameter experiments.

The indentations have been done in alloy 1, 2 and 3 in order to observe the influence of the driving force. Figure 4.3 shows the scheme of the indentations. Figure 4.3a shows the three indentations that were performed with the 2.5 mm diameter ball. The indentations were performed at different depths depths: 45, 90 and 180 μm. The three depths were chosen according to the grain size of the samples (~ 100 μm after annealing): one much smaller, one in the order of the grain size and the last one larger. Figure 4.3b presents the indentations performed with the 5.0 mm ball applying a maximal force of 1200 N. The samples have been indented after the annealing and mechanical polishing and before the ageing.

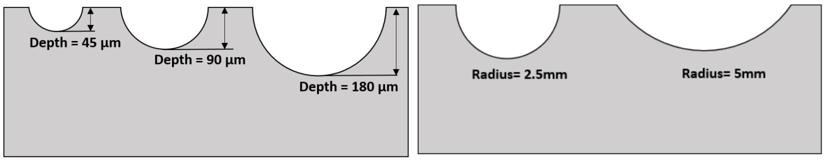

(a) Scheme of the indentations performed in the samples with the Brinell Hardness tester with a ball of 2.5 mm diameter.

(b) Scheme of the indentations performed in the samples with the Brinell Hardness tester with a balls of 2.5 mm and 5 mm diameter.

Figure 4.3: Scheme of the indentations performed in the samples with the Brinell Hardness tester.

The heat treatment consisted of an ageing step at 550 °C for 50 hours. The three alloys were heat treated at the same time. However, before applying the heat treatment, some steps were performed for the preparation of the samples: annealing, polishing, indentation, pre-flux and pre-heating of the furnace.

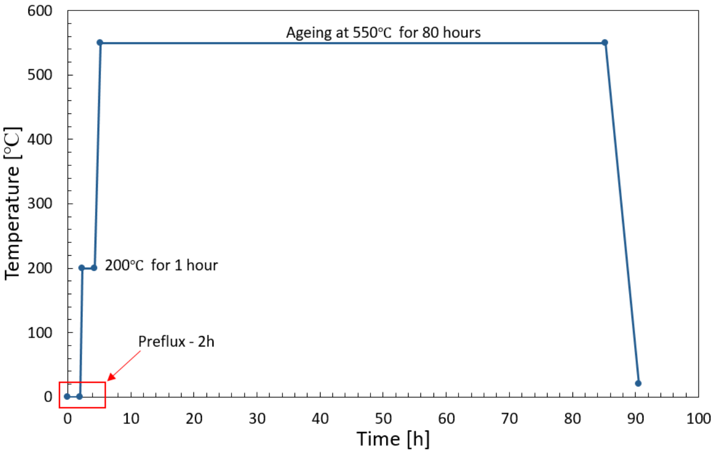

Figure 4.4: Heat treatment for the cold pre-deformation experiments.

Alloy 2 was annealed prior to the indentation in a vertical furnace and subsequently quenched. Alloys 1 and 3 were not annealed because the annealing temperature of alloy 1 was too high for a vertical furnace and alloy 3 was considered to be homogenised. Afterwards, the three alloys were mechanically polished and the indentations were performed. Next, the samples were cleaned with an ultrasonic bath with ethanol. The set-up of the furnace was the same as for set-up 4 in section 3.2. The same silica electric-resistance furnace was used, where the gas mixture of 10%$H_2 + Ar$ is fluxed for two hours before the heat treatment. The flux of argon goes through one filter and an extra furnace heated to 800ºC where there is titanium powder as a getter to remove all the oxygen present in the argon. Moreover, there is a bypass for the hydrogen to avoid heating it to 800ºC for safety reasons [36]. Additionally, one extra step is performed prior to the heat treatment: the chamber is pre-heated at 200ºC for 1 hour, so that the oxygen attached to the silica walls gets fluxed away [37]. Then the heat treatment was applied. Figure 4.4 shows a scheme of the whole heat treatment in the furnace.

4.3. Results and Discussion

The samples of the warm concurrent deformation experiments were oxidised in the dilatometer. SEM analysis was performed on the surface together with energy-dispersive spectroscopy and no precipitates were observed on the surface. For that reason, the precipitation was observed in the bulk material. On the other hand, no oxidation problems were observed in the cold deformation experiments, and surface precipitation was seen in the generated pores.

4.3.1. Warm Concurrent Deformation Experiments

The results of the warm concurrent deformation were unexpected: all of the samples were oxidized and some of the samples were deformed macroscopically, contracting axially and expanding laterally in the middle section of the sample. The samples underwent different stress levels: 0, 100, 125, 150, 175 and 200 MPa and only the samples submitted at 125 and 150 MPa presented the macroscopic deformation. In order to explain the origin of these deformation, the strain generated from the stress has been observed, together with the bulk of the samples.

4.3.1.1. Quantitative Results of Warm Concurrent Deformation Experiments

Energy-dispersive spectroscopy (EDS) was performed to all the samples. Only the samples at 125 and 150 MPa (highest strain) presented precipitation in the bulk as observed in figure 4.5, which is a representative example of the alloy at 125 MPa. The composition of the precipitates (points 1 and 2) have around 10 wt.%W (3 at.%), which is a higher value than the nominal, but far from the composition of W Laves phase (~ 30 at.%W). These results can originate from the low resolution of EDS relative to the size of these precipitates, which are in the nano scale whereas the resolution of the EDS is of the order of microns. Therefore, the only conclusion from these composition is that W-rich precipitates appear in the bulk of the most deformed samples and in the most deformed areas.

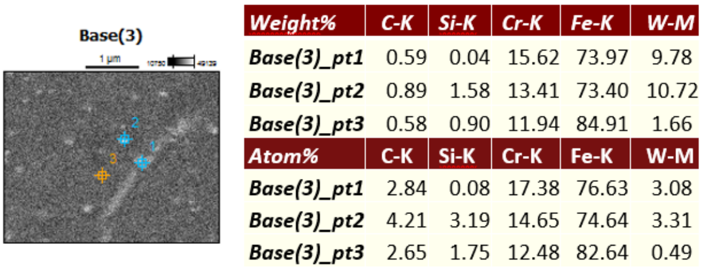

Weight%	C-K	Si-K	Cr-K	Fe-K	W-M
Base(3)_pt1	0.59	0.04	15.62	73.97	9.78
Base(3)_pt2	0.89	1.58	13.41	73.40	10.72
Base(3)_pt3	0.58	0.90	11.94	84.91	1.66
Atom%	**C-K**	**Si-K**	**Cr-K**	**Fe-K**	**W-M**
Base(3)_pt1	2.84	0.08	17.38	76.63	3.08
Base(3)_pt2	4.21	3.19	14.65	74.64	3.31
Base(3)_pt3	2.65	1.75	12.48	82.64	0.49

Figure 4.5: EDS analysis of precipitation on alloy 3 125 MPa.

The strain in % of the samples was observed in order to understand why the intermediate stress levels had been deformed macroscopically. As presented in figure 4.6a, it can be seen that indeed the samples at 125 and 150 MPa were the ones mostly deformed, with maximum strains of ~ 10% and ~ 14% for 125 and 150 MPa, respectively. The strain grew continuously until it reached a maximum before the release of the force as expected. The rest of the samples were barely deformed (less than 0.001%). From the point of view of the strain, it can be concluded that strain induces precipitation in the bulk of alloy 3.

In figure 4.6b the amount of precipitation in the bulk was quantified and compared to the strain level. It can be seen that the maximum areal fraction does not coincide for the maximum strained sample, as it would have been expected. The reason for this can originate from the non uniformity of the precipitation in the bulk. The maximum precipitation was observed in the middle section of the samples (macroscopically deformed) and close to the free surface. Therefore, the pictures were not taken in the same locations in each sample and that could have influenced the results.

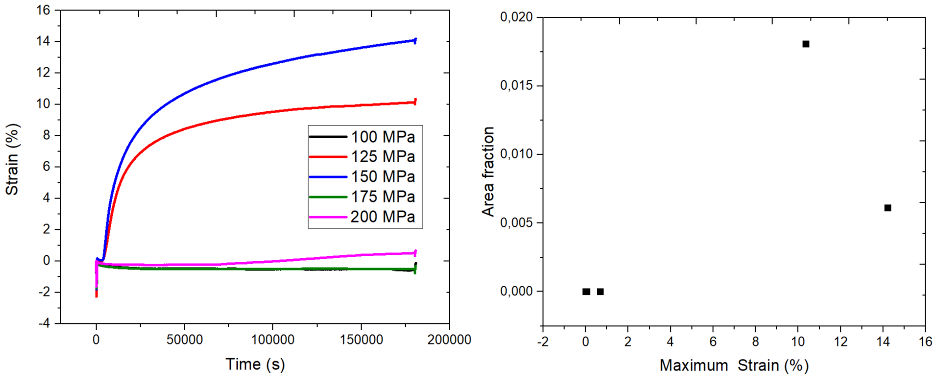

(a) Evolution of strain with time.

(b) Areal fraction with strain.

Figure 4.6: Quantitative analysis of the strain level for the different loads and the corresponding areal fraction in the bulk.

4.3.1.2. Qualitative Results of Warm Concurrent Deformation Experiments

First of all, pictures of the surface of the deformed samples are shown in figure 4.7, where it can be observed that cavities were generated in the surface and mostly in the grain boundaries as a consequence of the stress. No precipitation was observed, some literature on the surface precipitation of copper in tantalum substrates [41] and the results in the binary-ternary alloys suggest that oxidation layer could delay the surface precipitation.

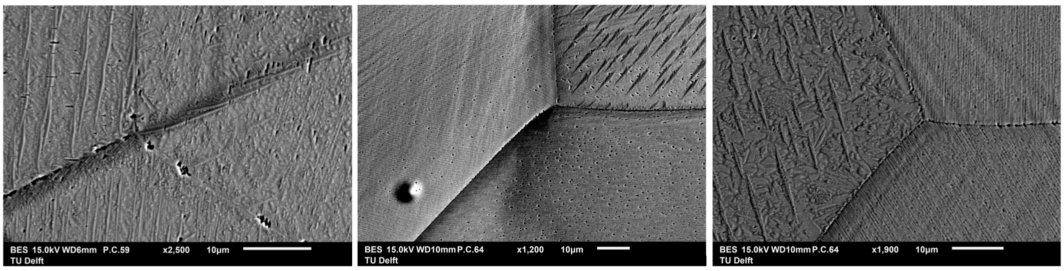

(a) Alloy 3 - 100MPa.

(b) Alloy 3 - 150MPa.

(c) Alloy 3 - 200MPa.

Figure 4.7: Backscattered images of surface alloy 3 after dilatometer.

Figure 4.8 shows the precipitation in the bulk of alloy 3 at three different stress levels. The first two figures (4.8a and 4.8b) correspond to the highly strained samples that were subjected to a stress of 125 and 150 MPa, respectively. It can be seen that both of them present a large number of pores originated from the deformation. However, figure 4.8c presents the bulk of the alloy that was tested at 200 MPa and no pores are observed. This alloy is representative of the bulk at 0, 100 and 175 MPa. These results are expected, as cavities are originated when the material is deformed. Together with the pores, some Si-rich particles were found in the samples. These Si-rich particles were found in all of the sample before the heat treatment, therefore, it has been considered that they are present in the raw material.

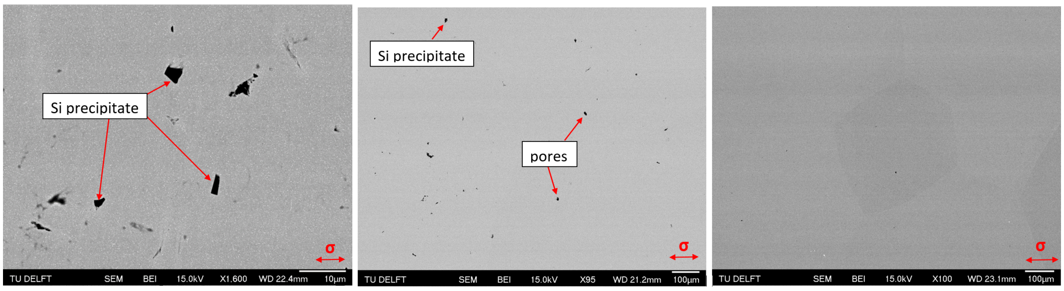

(a) 125 MPa.

(b) 150 MPa.

(c) 200 MPa.

Figure 4.8: SEM back-scattered images of the bulk of alloy 3 after the heat treatment.

Figure 4.9 present a high magnification of the bulk section for the deformed samples, where the W-rich precipitates are visible. It can be seen in figures 4.9a and 4.9b that the precipitates are equiaxed, nano-sized and are distributed homogeneously in the matrix. Moreover, there are no precipitates in the cavities. This suggests that particles precipitate at dislocations. Furthermore, these precipitates were only found in the most strongly deformed sections of the samples: the middle part expanded laterally and towards the free surface. The embedded ends that were not deformed did not show any trace of W-rich precipitates. This agrees with the theory of the precipitation on dislocation. Finally, figure 4.9c shows that also the bulk material presented pores as a result of the deformation.

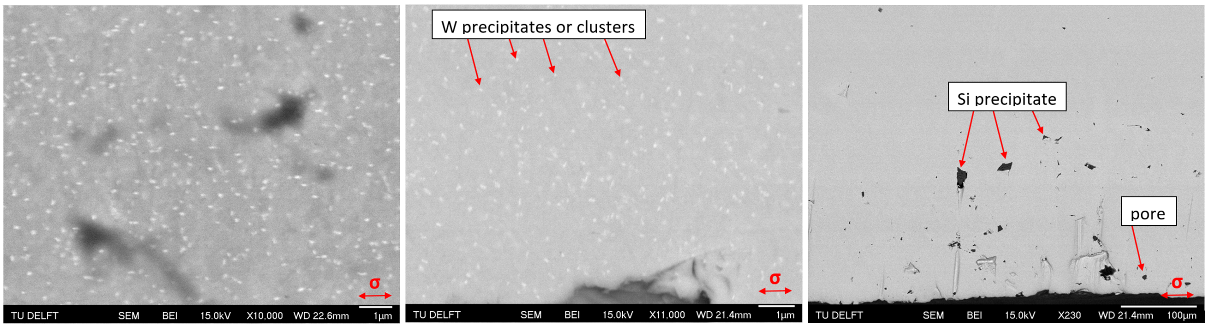

(a) 125 MPa.

(b) 150 MPa.

(c) 150 MPa - close to the edge.

Figure 4.9: High magnification SEM back-scattered images of the bulk of alloy 3 after the heat treatment, where W-rich particles can be observed.

4.3.2. Cold Prior Deformation Experiments

The results of the cold prior deformation were very encouraging. These alloys have been designed to start nucleating W Laves phase at 1000 hours at 550ºC. These experiments found that the Fe_2W Laves phase precipitated only in the cavities formed due to the deformation. These results, which are discussed below, have proven the self-healing properties of these alloys.

4.3.2.1. Quantitative Results of Cold Prior Deformation Experiments

Figure 4.10 presents the hardness results obtained from the indentation experiments. Figure 4.10a shows the difference in the alloy hardness, where Alloy 1 is the softest and 3 the hardness as expected due to the higher content of tungsten. Figure 4.10b shows the evolution of the hardness with the the indentation depth, as expected, the hardness calculations considers that it has been easier to penetrate, and consequently the material is softer.

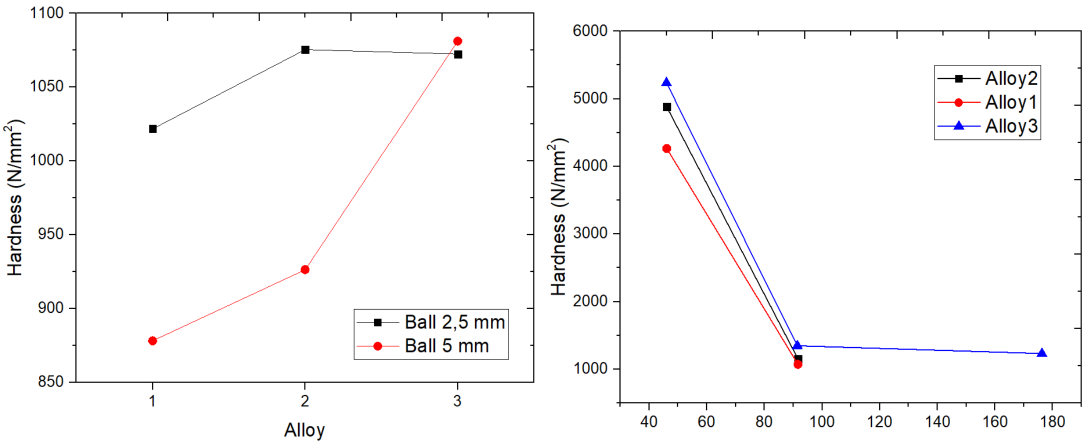

(a) Hardness per alloy and indentor size for a maximal applied force of 1200 N.

(b) Alloy 2.

Figure 4.10: Hardness evolution with indentation depth for each alloy.

EDS analysis was performed to the three alloys. Figures 4.11a, 4.11b and 4.11c show the composition of the matrix and the precipitates that were found on th surface. As can be observed, in all three the precipitates had ~ 30 at.%W, which coincides with W Laves phase.

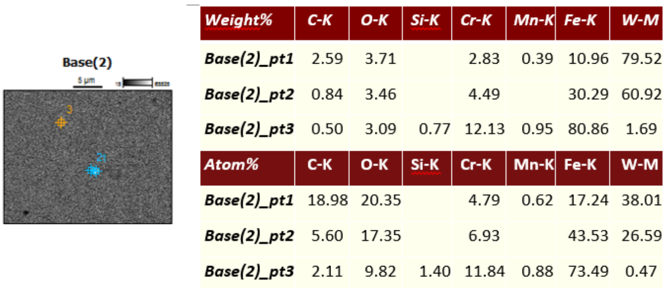

Weight%	C-K	O-K	Si-K	Cr-K	Mn-K	Fe-K	W-M
Base(2)_pt1	2.59	3.71		2.83	0.39	10.96	79.52
Base(2)_pt2	0.84	3.46		4.49		30.29	60.92
Base(2)_pt3	0.50	3.09	0.77	12.13	0.95	80.86	1.69
Atom%	**C-K**	**O-K**	**Si-K**	**Cr-K**	**Mn-K**	**Fe-K**	**W-M**
Base(2)_pt1	18.98	20.35		4.79	0.62	17.24	38.01
Base(2)_pt2	5.60	17.35		6.93		43.53	26.59
Base(2)_pt3	2.11	9.82	1.40	11.84	0.88	73.49	0.47

(a) Alloy 1.

Weight%	C-K	O-K	Si-K	Cr-K	Mn-K	Fe-K	W-M
Base(5)_pt1	10.88	2.46		2.63		12.39	65.22
Base(5)_pt2	2.47	1.89		4.84		26.70	64.09
Base(5)_pt3	2.02	3.34		5.48		28.28	60.88
Atom%	**C-K**	**O-K**	**Si-K**	**Cr-K**	**Mn-K**	**Fe-K**	**W-M**
Base(5)_pt1	50.44	8.55		2.81		12.36	19.76
Base(5)_pt2	16.56	9.52		7.48		38.43	28.02
Base(5)_pt3	12.74	15.83		7.98		38.36	25.09
Base(5)_pt4	2.39	6.14	2.24	11.18	0.35	77.23	0.47

(b) Alloy 2.

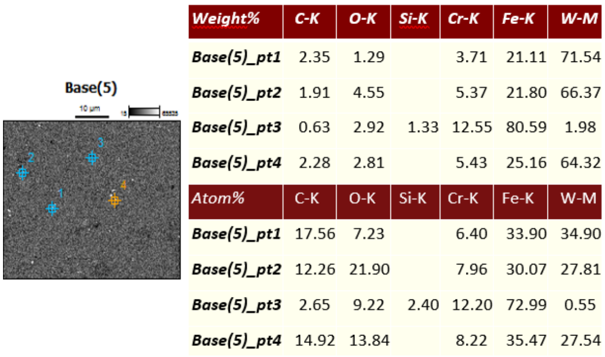

Weight%	C-K	O-K	Si-K	Cr-K	Fe-K	W-M
Base(5)_pt1	2.35	1.29		3.71	21.11	71.54
Base(5)_pt2	1.91	4.55		5.37	21.80	66.37
Base(5)_pt3	0.63	2.92	1.33	12.55	80.59	1.98
Base(5)_pt4	2.28	2.81		5.43	25.16	64.32
Atom%	C-K	O-K	Si-K	Cr-K	Fe-K	W-M
Base(5)_pt1	17.56	7.23		6.40	33.90	34.90
Base(5)_pt2	12.26	21.90		7.96	30.07	27.81
Base(5)_pt3	2.65	9.22	2.40	12.20	72.99	0.55
Base(5)_pt4	14.92	13.84		8.22	35.47	27.54

(c) Alloy 3.

Figure 4.11: EDS analysis of the precipitates in alloys 1, 2 and 3.

As mentioned also in the previous section, Si-rich particles were found in all the three alloys even after homogenisation. These particles were analysed with EDS and the results are presented in figure 4.12. The composition has ~60-70 wt.%Si and ~10 wt.%C, and the rest is Cr and Fe. It has been considered that silica carbide was formed during the manufacturing of the alloy, which is a high temperature inclusion and the Cr and Fe readings come from the EDS resolution, which will be getting information from the surrounding matrix.

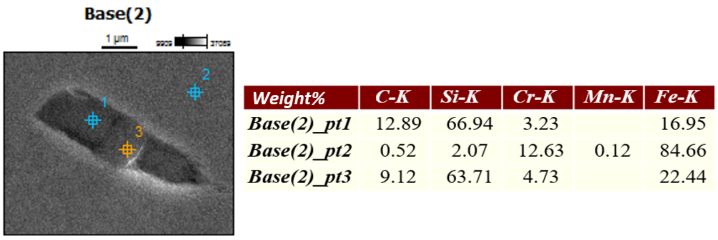

Weight%	C-K	Si-K	Cr-K	Mn-K	Fe-K
Base(2)_pt1	12.89	66.94	3.23		16.95
Base(2)_pt2	0.52	2.07	12.63	0.12	84.66
Base(2)_pt3	9.12	63.71	4.73		22.44

Figure 4.12: Si particle.

4.3.2.2. Qualitative Results of Cold Prior Deformation Experiments

The qualitative results from the indentation experiments have shown barely any difference between the indentations. The indentations have produced cavities in the surface, where the tungsten Laves phase has precipitated occasionally. The cavities have been found isolated or linked to a Si-rich particles or other inclusion. This is expected, as carbide and inclusions are hard particles difficult to deform. Then, when the stress in applied, there is a mismatch between the deformation of a more ductile matrix and the hard particles and a cavity nucleates in the interface. Figures 4.13a, 4.13b and 4.13c show a general picture of the indentations made with the ball of 5 mm diameter with a maximal force of 1200 N in the three alloys. It can be seen that the cavities (dark points) are only located at the indent surface. The nucleation of these cavities does not have a preference and are located all over the indent in al of the cases. Moreover, the quantification of cavities was not possible as the black points are also inclusions.

Finally, figures 4.13d, 4.13e and 4.13f present more detailed images of the precipitation of the Fe_2W Laves phase in the cavities. It can be observed that in the three alloys Laves phase has precipitated. There cavities are semi and fully covered. Some semi-covered cavities have shown one nucleation site and others several nucleation sites.

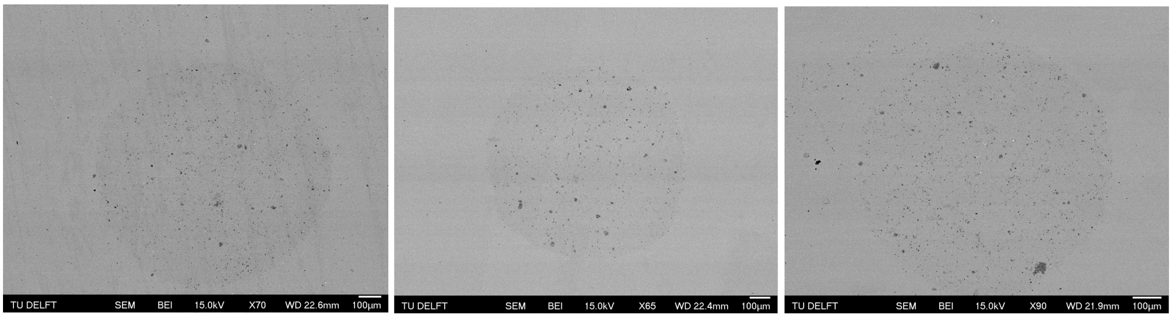

(a) Alloy 1. (b) Alloy 2. (c) Alloy 3.

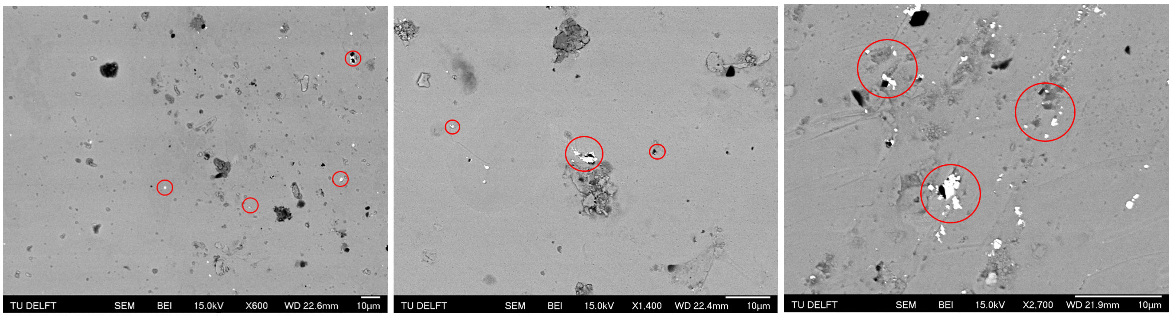

(d) Alloy 1. (e) Alloy 2. (f) Alloy 3.

Figure 4.13: Precipitation in the indents.

5

Summary and Conclusion

Based on section 2, the research objective of this thesis was to contribute to developing the theory of cavity-filling on self-healing creep-resistant steels investigated by van der Zwaag and van Dijk [5] by studying the influence of additional self healing elements and concurrent deformation on surface precipitation. These two objectives were decided to be studied separately. This section will present a summary of the results, followed by the conclusions, where the research questions will be answered.

5.1. Summary

Firstly, the influence of an additional self-healing element was assessed by comparing the surface precipitation on a binary and a ternary alloy, where the evolution of precipitation with time was the main focus. Chapter 3 presented all the results, which can be summarize in:

- No surface segregation was detected by EDS with the measures on the matrix. The composition of the Au-rich (~55 at.%Au) precipitates in the binary alloy agrees with the Fe-Au binary phase diagrams calculations, where at 700 °C the composition should be around ~60 at.%Au. This type of precipitate was found within the grain and in the grain boundaries in both binary and ternary alloys. In the ternary alloy, apart from the Au-rich precipitates, whose composition was not influenced by the addition of W, three different types of W-rich particles were found:
  1. Big (~ $1\mu m$), round and porous precipitate with a ~30 at.%W which coincides with Laves phase composition. This coral-shape is typically observed with the reduction of WO_2 to α-W with H_2 [46]. It is considered that the WO_2 was present in the raw material and got reduced in the furnace.
  2. Small (~ 100 nm) W-rich precipitates. Their composition is ~5-8 at.%W, and they are present in a variety shapes within the same grain: plates or equiaxed and always with sharp edges. TEM analysis detected W-rich precipitates that contained ~5-8 at.%W, the STEM mode results showed that their lattice spacing that corresponded to Laves phase. Therefore, it could be concluded that the small W-rich phase is consistent with the Laves phase.
  3. Small (~ 100 nm) W-Au-rich particles which contain ~10-20 at.%W and ~10-20at.%Au. They are present in a variety shapes within the same grain: plates or equiaxed and always with more rounded edges. TEM results have showed that these could be a mixture of Au-rich and W-rich precipitates in a nanoscale that precipitate in contact with each other, occasionally forming in a sandwich pattern.
- The distribution of the precipitates changed with the precipitation of the small W-rich precipitate with lower at.%W composition, which only appeared for longer times (16 and 32 hours). In the cases where only Au-rich precipitated on the surface (binary alloy or ternary for short times), three different grain types were found:
  1. No precipitation
  2. Round precipitates, which could be found following different distributions: (i) High number density precipitation with no clear precipitation pattern. The precipitation is uniform and the precipitates

have a smaller size than the rest of the grains. (ii) Low number density precipitation. The precipitates are found to have nucleated in a pattern and several preferential directions are found. Generally, in these grains the precipitates have a larger size. (iii) In some grains, there can be one or two isolated big precipitates.

3. Needle-like precipitation. In most of the cases, the number density is high for this shape of precipitates. In the vast majority of the grains, the needles precipitate on a patter following one preferential direction which is parallel to their longitudinal direction. In some cases, the needles can follow two preferential direction in which to precipitate. These direction have an angle of $\sim 42 \pm 8°$. The number of needles in each direction are equally divided and the precipitates longitudinal direction is always parallel to the preferential precipitation direction.

However, with the appearance of the W-rich precipitates the Au-rich precipitates patterns and shapes start to be less frequent among the grains. Only a few grain still show the type of precipitation of the binary alloy together with a uniformly distribution of small W-rich precipitates. In this case, the Au-rich precipitates are considerably $\sim 1.3 - 3$ times bigger than the W-rich. In the rest of the grain, the Au-rich and W-rich blend together in size and shape, where the main difference is that Au-rich have more rounded edges. The precipitation of the W-rich precipitates was homogeneous withing the grains. However, just as like Au-rich precipitates, the precipitation only appears in some grains, which suggests that there is also a crystallographic relationship between the Fe matrix and the W Laves phase.

- EBSD analysis shows the following crystallographic relationship between the Fe matrix and the Au-rich precipitates: 111_{Fe} → Au round precipitates (high aspect ration), and 101_{Fe} → Au needle precipitates (low aspect ratio). However, it should be noticed that not many precipitates were detected due to their small size. This EBSD was in low resolution and higher ageing times would increase the average diameter and precipitation in more grains, facilitating EBSD measurements.

  Moreover, TEM analysis resulted in the confirmation of a FCC Au-rich phase, which precipitates in the BCC-Fe matrix with the following direction: $[200]_{matrix}||[002]_{Au-precip}$, $[200]_{matrix}||[1\bar{1}0]_{Au-precip}$ and with interface $(015)_{matrix}||(116)_{Au-precip}$.

- Moving on to kinetics, a power law between the radius and the time with an exponent of ~0.25 was expected to be followed by precipitation on the surface based on the theoretical calculations from Carlow [30] and the experimental results of Fang [48]. Due to the diversity of shapes and sizes within the ternary alloy, the areal fraction ($\propto r^2$) was studied and expected to follow a power law with an exponent of ~0.5. The results of both binary and ternary alloy agree, where the calculated exponent were 0.44 ± 0.13 and 0.5 ± 0.13, respectively. Moreover, the precipitation of W-rich phase only happened for longer times (from 16 hours onwards) as expected due to the lower diffusivity of W.

  Coalescence was observed in the binary alloy, whereas in the ternary the apparition of W-rich slowed down the growth of Au-rich and no coalescence was observed neither in Au or W precipitates. Finally, the cooling rate has a large influence in the precipitation kinetics as observed by [17] with surface precipitation on aluminium alloys. A slower cooling rate ended up with lower number densities and higher average diameters that higher cooling rates.

The second part of the thesis focused on the influence of deformation on surface precipitation. There were two types of deformation experiments that were performed. The first type was cold spherical indentations performed prior to the heat treatment. The observations can be summarize in:

- There was more precipitation at the indents than in the flat surface. Detailed observation of the edge of the grain boundaries show that precipitation is induced by the indent. The difference between the different indentation depths is not straight forward due to the non-uniform distribution of the precipitates along the indents.

  There was a difference in the behaviour of Au-rich and W-rich precipitates. Au-rich precipitates have high preferential crystallographic orientations in which to nucleate, and even at low loads the strain is incapable of inducing much precipitation. At higher loads, more grains with precipitations are observed and even coalescence in some grain with the apparition of Au-rich bands. Whereas W-rich have been found to precipitate in more more number of grain and be less restrictive with the crystallographic orientations, and therefore the influence of the strain is more evident.

- In the case of the three alloys, the indents accelerated precipitation by the generations of cavities or imperfections in which the W Laves phase was observed. The Laves phase has been observed partially and fully filling cavities. Moreover, by comparing the indents with the same spherical ball, it can be concluded that higher indentation depths and loads have resulted in higher strain fields. From the experiments at the same load but with different radius, the larger radius showed higher precipitation, which was not expected as applies a lower pressure. As for the difference between the three alloys, there was no qualitative difference between the three alloys even though the driving force of alloy 3 twice the driving force of alloy 1 and no quantitative analysis was performed.

The second deformation type was the application of warm concurrent compressive force, which only tested on the experimental alloy 3. It was observed that the strain field induced W-rich precipitation, which was present in the bulk material in the form of clusters of nano-scale size. Due to their uniform distribution and the fact that they were observed only in the most deformed parts of the sample, it is concluded that they nucleated at dislocations.

5.2. Conclusions

From this summary five clear conclusions can be drawn:

1. There is a deceleration interaction between W and Au. The appearance of W-rich precipitates slows down the Au-rich precipitation kinetics.
2. Introducing both W and Au as self-healing agents, the ternary alloy is proved to be as efficient as the binary since the same areal fraction is covered with both alloys for the studied times.
3. No precipitation was found in the bulk, which confirms the site-selectivity of the precipitates, necessary for self-healing.
4. The hypothesis of Sun [16] was confirmed with an EBSD analysis, which concluded that there is a relationship between the crystallographic orientation of the grains and the shape of the Au-rich precipitates. Further TEM analysis also confirmed a crystallographic relationship between the the matrix and the precipitates in the bulk.
5. The strain field produced by the indentation accelerated the precipitation kinetics. Higher depths and loads, produce higher strain fields and more precipitation, as expected. In the binary and ternary alloys, new patterns were observed in the precipitation, which are believed to be linked to dislocations. In the creep steel, the precipitates nucleated in the cavities of the surface. The warm deformation applied in alloy 3 resulted in precipitation of W-rich at dislocations in the mostly deformed sections in the bulk.

Finally, all of these conclusions help to answer the two research questions that were proposed at the beginning of this thesis:

- What is the influence of the addition of a second self healing element?

  The addition of tungsten in Fe-Au alloy was studied. There is a decelerating influence of tungsten on gold, since it retards the nucleation and growth of Au-rich particles. However, if the areal fraction coverage from Fe-Au and Fe-Au-W are compared, they offered the same coverage for the same ageing times. Therefore, some Au-rich precipitation is retarded at expense of the nucleation of W-rich precipitates.

- What is the influence of deformation on surface precipitation?

  Deformation clearly accelerates precipitation in the case of the creep experimental alloy, as it has proved to nucleates precipitates after 80 incubation hours when they were designed to precipitate at 1000 hours. This is possibly due to the combination of the surface, the strain field induced with the indent and the cavities formed, which together lowers the nucleation barrier. Additionally, the warm deformation has shown precipitation at dislocations in the bulk for strain levels of 12-14%. However, the indentation on the binary and ternary system, which is not based on precipitation in cavities, has been observed to increase precipitation, but highly dependant on the precipitate type. The strength of the influence depends on the crystal orientation of the matrix.

Bibliography

[1] S. J. Garcia and H. R. Fischer. Self-healing polymer systems: Properties, synthesis and applications. In *Smart Polymers and their Applications*, pages 271–298. Woodhead Publishing Limited, 2014.

[2] V. Kilicli, X. Yan, N. Salowitz, and P. K. Rohatgi. Recent Advancements in Self-Healing Metallic Materials and Self-Healing Metal Matrix Composites. *Jom*, 70(6):846–854, 2018.

[3] Jr. W. D. Callister and D. G. Rethwisch. *Materials Science and Engineering -An Introduction*. Wiley, 9 edition, 2014.

[4] G. N. Haidemenopoulos. *Physical Metallurgy: Principles and Design*. CRC Press, 2018.

[5] N. van Dijk and S. van der Zwaag. Self-Healing Phenomena in Metals. *Advanced Materials Interfaces*, 5(17):1–13, 2018.

[6] T. Kern F. Abe and R. Viswanathan, editors. *Creep-resistant Steels*. Woodhead Publishing, 1 edition, 2007.

[7] K. Laha, J. Kyono, S. Kishimoto, and N. Shinya. Beneficial effect of B segregation on creep cavitation in a type 347 austenitic stainless steel. *Scripta Materialia*, 52(7):675–678, 2005.

[8] N. Shinya, J. Kyono, and K. Laha. Self-healing effect of boron nitride precipitation on creep cavitation in austenitic stainless steel. *Journal of Intelligent Material Systems and Structures*, 17(12):1127–1133, 2006.

[9] K. Laha, J. Kyono, and N. Shinya. An advanced creep cavitation resistance Cu-containing 18Cr-12Ni-Nb austenitic stainless steel. *Scripta Materialia*, 56(10):915–918, 2007.

[10] S. Zhang, J. Kohlbrecher, F. D. Tichelaar, G. Langelaan, E. Brück, S. van Der Zwaag, and N. H. van Dijk. Defect-induced Au precipitation in Fe-Au and Fe-Au-B-N alloys studied by in situ small-angle neutron scattering. *Acta Materialia*, 61(18):7009–7019, 2013.

[11] S. Zhang, C. Kwakernaak, F. D. Tichelaar, W. G. Sloof, M. Kuzmina, M. Herbig, D. Raabe, E. Brück, S. van der Zwaag, and N. H. van Dijk. Autonomous Repair Mechanism of Creep Damage in Fe-Au and Fe-Au-B-N Alloys. *Metallurgical and Materials Transactions A: Physical Metallurgy and Materials Science*, 46(12):5656–5670, 2015.

[12] S. Zhang, C. Kwakernaak, W. Sloof, E. Brück, S. van der Zwaag, and N. van Dijk. Self healing of creep damage by gold precipitation in iron alloys. *Advanced Engineering Materials*, 17(5):598–603, 2015.

[13] C. D. Versteylen, M. H.F. Sluiter, and N. H. van Dijk. Modelling the formation and self-healing of creep damage in iron-based alloys. *Journal of Materials Science*, 53(20):14758–14773, 2018.

[14] S. Zhang, H. Fang, M. E. Gramsma, C. Kwakernaak, W. G. Sloof, F. D. Tichelaar, M. Kuzmina, M. Herbig, D. Raabe, E. Brück, S. van der Zwaag, and N. H. van Dijk. Autonomous Filling of Grain-Boundary Cavities during Creep Loading in Fe-Mo Alloys. *Metallurgical and Materials Transactions A: Physical Metallurgy and Materials Science*, 47(10):4831–4844, 2016.

[15] H. Fang, N. Szymanski, C. D. Versteylen, P. Cloetens, C. Kwakernaak, W. G. Sloof, F. D. Tichelaar, S. Balachandran, M. Herbig, E. Brück, S. van der Zwaag, and N. H. van Dijk. Self healing of creep damage in iron-based alloys by supersaturated tungsten. *Acta Materialia*, 166:531–542, 2019.

[16] W. W. Sun, H. Fang, N .H. Dijk, S. van der Zwaag, and C. R. Hutchinson. Linking Surface Precipitation in Fe-Au Alloys to Its Self-healing Potential. *Metallurgical and Materials Transactions A*, 48(5):2109–2114, 2017.

[17] Y Chen, X Y Fang, Y Brechet, and C R Hutchinson. Surface precipitation on engineering alloys. *ScienceDirect - Acta Materialia*, 81:291–303, 2014.

[18] T. Vu Dinh, W. W. Sun, Y. Yue, Y. Wu, C. R. Hutchinson, and S. Thomas. On the miniaturised sacrificial protection achieved by surface precipitation in aluminium alloys. *Corrosion Science*, 145(March):67–79, 2018.

[19] H. Fang and N.H. van Dijk. *Solid state phase transformations in steels: a neutron and synchrotron radiation study*. Phd thesis, TU Delft, 2019.

[20] C. Uebing. Surface cosegregation phenomena on alloys and steels: Structural features and phase transitions. *Progress in Surface Science*, 53(2-4):297–304, 1996.

[21] J. M. Roussel, G. Tréglia, and B. Legrand. Surface Segregation Maps Derived from Tight-Binding Ising Model. *Solid State Phenomena*, 172-174:1008–1015, 2011.

[22] H. Viefhaus C. Uebing and H.J. Grabke. Formation of CrN surface compounds and surface precipitates on Fe-15%Cr-N single crystals. *Applied Surface Science*, 32:363–380, 1988.

[23] B. Eltester and C. Uebing. Surface segregation phenomena on Fe-3.5%Mo-N(100): The formation of a MoN surface compound. *Surface Science*, 347(1-2):39–45, 1996.

[24] D.A. Porter and K.E. Easterling. *Phase Transformations in Metal and Alloys*. Springer-Science+Business Media, B.V., 2 edition, 1992.

[25] H. Chen and S. van der Zwaag. A general mixed-mode model for the austenite-to-ferrite transformation kinetics in Fe-C-M alloys. *Acta Materialia*, 72:1–12, 2014.

[26] C. Uebing, H. Viefhaus, and H. J. Grabke. Surface cosegregation and surface precipitation on Fe-3%V-C,N(100) single crystals. *Surface Science*, 264(1-2):114–126, 1992.

[27] M. De Jong, S. van der Zwaag, and M. Sluiter. Ab-initio modeling of metastable precipitation processes in aluminum 7xxx alloys. *International Journal of Materials Research*, 103(8):972–979, 2012.

[28] Dennis W. Readey. *Kinetics in Materials Science and Engineering*. CRC Press, Taylor & Francis Group, Boca Raton, FL, 2016.

[29] N. H. van Dijk, S. E. Offerman, J. Sietsma, and S. van der Zwaag. Barrier-free heterogeneous grain nucleation in polycrystalline materials: The austenite to ferrite phase transformation in steel. *Acta Materialia*, 55(13):4489–4498, 2007.

[30] G. R. Carlow and M. Zinke-Allmang. Areal fraction effects during late-stage clustering on surfaces. *Surface Science*, 328(3):311–319, 1995.

[31] Manhong Zhao, Nagahisa Ogasawara, Norimasa Chiba, and Xi Chen. A new approach to measure the elastic-plastic properties of bulk materials using spherical indentation. *Acta Materialia*, 54(1):23–32, 2006.

[32] M. Munawar Chaudhri. Subsurface plastic strain distribution around spherical indentations in metals. *Philosophical Magazine A: Physics of Condensed Matter, Structure, Defects and Mechanical Properties*, 74(5):1213–1224, 1996.

[33] M. Munawar Chaudhri. Strain hardening around spherical indentations. *Physica Status Solidi (A) Applied Research*, 182(2):641–652, 2000.

[34] S. Zhang. *Self healing of damage in Fe-based alloys*. Doctoral dissertation, TU Delft, 2015.

[35] Nikodem Szymanski. Self healing of deformation induced samage in Fe-W alloys. *Journal of Chemical Information and Modeling*, 53(9):1689–1699, 2019.

[36] G. R. Astbury and S. J. Hawksworth. Spontaneous ignition of hydrogen leaks: A review of postulated mechanisms. *International Journal of Hydrogen Energy*, 32(13):2178–2185, 2007.

[37] J. Tennermann. Dewpoint measurement accuracy. *Measurement, Instrumentation, and Sensors Handbook: Spatial, Mechanical, Thermal, and Radiation Measurement, Second Edition*, 1(October):5–1–5–14, 2017.

[38] C. Zener. Theory of growth of spherical precipitates from solid solution. *Journal of Applied Physics*, 20(10):950–953, 1949.

[39] Masakatsu Hasegawa. Ellingham Diagram. In *Treatise on Process Metallurgy*, volume 1, chapter 3, pages 507–516. Elsevier Ltd., 2013.

[40] M. Graf, T. Holm, and S. Wiberg. Neutral hardening and annealing. In *Furnace atmospheres no.2.*, number 2, pages 33–56. Linde AG, 2017.

[41] F. Fillot, Zs Tokei, and G. P. Beyer. Surface diffusion of copper on tantalum substrates by Ostwald ripening. *Surface Science*, 601(4):986–993, 2007.

[42] H Okamoto, T B Massalski, Phase Dia, H Okamoto, and T B Massalski. Au (Gold) Binary Alloy Phase Diagrams. In *ASM Handbook: Alloy Phase Diagrams*, volume 3, pages 152–174. ASM International, 1984.

[43] O.K. von Goldbeck. Iron-Gold Fe-Au. In *Iron-Binary Phase Diagrams*, page 14. Springer-Verlag, Berlin, Heidelberg, 1982.

[44] S. Wilayat Husain, M. Saeed Ahmed, and Ihtzaz Qamar. Dendritic morphology observed in the solid-state precipitation in binary alloys. *Metallurgical and Materials Transactions A: Physical Metallurgy and Materials Science*, 30(6):1529–1534, 1999.

[45] Maria Lujan Castro and Osvaldo Fornaro. Dendritic morphology of gamma precipitate in a beta CuZnAl ma Formación de precipitados γ de morfologia dendrítica en una matriz β CuZnAl. *Revista Materia*, 12(July):541–548, 2007.

[46] Dean S. Venables and Michael E. Brown. Reduction of tungsten oxides with hydrogen and with hydrogen and carbon. *Thermochimica Acta*, 285(2):361–382, 1996.

[47] H. Yu. *Manuscript - Design of ferritic heat resistant steels with self-healing properties at 550^{o}C and above.* Doctoral dissertation, TU Delft, 2019.

[48] H Fang, Y Fu, C Kwakernaak, W G Sloof, E Brück, S Zwaag, and N H Van Dijk. Surface precipitation of supersaturated solutes in binary and ternary iron-based alloys. pages 1–9, 2019.